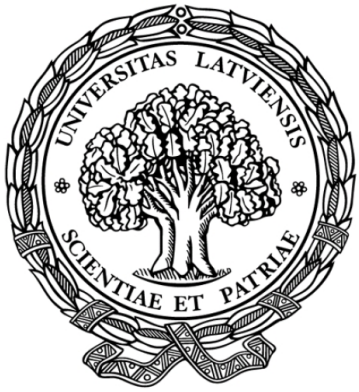

UNIVERSITY OF LATVIA

FACULTY OF PHYSICS AND MATHEMATICS

SYNTHESIS AND UP-CONVERSION LUMINESCENCE OF ERBIUM DOPED LANTHANUM CONTAINING FLUORIDE STRUCTURES

Anatolijs Šarakovskis

Doctoral thesis

Subsection: Solid State Physics

Rīga, 2010

Table of contents

Abstract 4
Anotācija 5
List of Figures 6
List of Tables 9
1. Introduction 10
1.1. Topicality and motivation for the research 10
1.2. Main goals and tasks of the work 14
1.3. Novelty of this work 14
1.4. Author contribution 15
2. Acronyms 16
3. Physical background 17
3.1. Rare-earth elements 17
3.2. Erbium 20
3.3. Up-conversion luminescence in rare-earth ions 22
3.3.1. Excited state absorption 24
3.3.2. Energy transfer up-conversion 25
3.3.3. Sensitized energy transfer up-conversion 26
3.3.4. Cross-relaxation 27
3.3.5. Comparison between excited state absorption and energy transfer up-conversion 28
3.4. Properties of up-conversion luminescence 29
3.4.1. Power dependence of up-conversion luminescence 29
3.4.2. Up-conversion luminescence and phonons 32
3.4.3. Dynamics of UC luminescence 34
3.5. Synthesis and up-conversion luminescence in rare-earth doped $NaLaF_4$ 36
3.6. Synthesis and up-conversion luminescence in rare-earth doped oxyfluoride glass ceramics 39
4. Experimental methods 42
4.1. Synthesis 42
4.2. Differential thermal analysis 43
4.3. Structure investigations 45
4.4. Infrared absorption and Raman spectra measurements 45
4.5. Luminescence measurements 46
4.5.1. Luminescence spectra 46
4.5.2. Excitation spectra 46
4.5.3. Luminescence kinetics 47
5. Results 48
5.1. Erbium doped $NaLaF_4$ 48
5.1.1. Mixing-firing synthesis of $NaLaF_4:Er^{3+}$ 48
5.1.2. Structure and optical properties of $NaLaF_4:Er^{3+}$ 48
5.1.3. Summary 59
5.1.4. Novel synthesis method 60
5.1.5. Structure and optical properties of $NaLaF_4:Er^{3+}$ 61
5.1.6. Summary 71

5.2. Erbium doped oxyfluoride glass ceramics 72
5.2.1. Synthesis and structure of glass and glass ceramics 72
5.2.2. Optical properties of glass and glass ceramics 74
5.2.3. Summary 83
5.3. Thesis 84
6. Outlook 85
References 87
7. List of publications 97
8. List of conference abstracts 98
9. Acknowledgements 100

Abstract

Up-conversion process involves conversion of low-energy light photons into higher-energy light photons. This is being achieved by a “ladder” type stepwise excitation of a luminescent ion through sequential absorption of lower-energy photons followed by the emission of the accumulated energy in a form of luminescence. In this case the luminescence light has shorter wavelength (higher photon energy) than any of the absorbed photon.

In the present work the main focus is set on the up-conversion luminescence research of erbium doped $NaLaF_4$ crystalline material and erbium doped transparent oxyfluoride glass ceramics containing LaF_3 nanocrystallites.

Structure, photoluminescence and up-conversion luminescence of $NaLaF_4:Er^{3+}$ are studied by means of x-ray diffraction, stationary and time-resolved spectroscopy methods. It will be shown that the increase of Er^{3+} concentration in $NaLaF_4:Er^{3+}$ causes the formation of $Na(LaEr)F_4$ complex compound responsible for the shortening of the lifetime of Er^{3+} luminescence. The quenching of the up-conversion luminescence in $NaLaF_4:Er^{3+}$ annealed at different temperatures is due to Er^{3+}-oxygen related defects. Additionally, a novel synthesis route of $NaLaF_4:Er^{3+}$ will be shown allowing to synthesize the material without using hazardous hydrofluoric acid.

Oxyfluoride silicate glass ceramics containing $LaF_3:Er^{3+}$ is synthesized by thermal treatment of the precursor glass and up-conversion properties of the material are studied at room temperature and 50 K. It will be shown that the dominance of either excited-state-absorption or energy-transfer mechanisms of the up-conversion luminescence mechanisms in oxyfluoride glass ceramics containing $LaF_3:Er^{3+}$ nanocrystals is temperature dependent. A dominance criterion of either of the two mechanisms of the up-conversion luminescence in the crystalline phase of the glass ceramics will be provided.

Anotācija

Augšup-pārveidošanas (AP) procesā gaismas fotoni ar mazāku enerģiju tiek pārveidoti par fotoniem ar lielāku enerģiju. To var sasniegt ar luminiscējoša jona pakāpienveidīgu ierosināšanas procesu, kurā secīgiem mazākas enerģijas fotonu absorbcijas processiem seko uzkrātās enerģijas izstarošana luminiscences veidā. Šajā gadījumā luminiscences starojumam ir īsāks viļņa garums (fotoniem ir lielāka enerģija) nekā ierosinošajam starojumam.

Darbā galvenā uzmanība ir pievērsta AP luminiscences pētījumiem ar erbija joniem aktivētā $NaLaF_4$ kristāliskā materiālā un ar erbija joniem aktivētā caurspīdīgā stikla keramikā, kas satur LaF_3 kristalītus.

$NaLaF_4:Er^{3+}$ struktūra, fotoluminiscence un AP luminiscence ir pētīta ar rentgenstaru difrakcijas, stacionāras un laikā izšķirtās spektroskopijas palīdzību. Darbā ir parādīta jaunizstrādātā $NaLaF_4:Er^{3+}$ sintēzes metode, kas atšķirībā no citām metodēm ļauj iegūt $NaLaF_4:Er^{3+}$, neizmantojot kaitīgo fluorūdeņraža skābi. Ir secināts, ka Er^{3+} koncentrācijas pieaugums izraisa $Na(LaEr)F_4$ kompleksā savienojuma veidošanos, kas samazina Er^{3+} luminiscences dzīves laiku. Darbā pierādīts, ka dažādās temperatūrās sintezētajam $NaLaF_4:Er^{3+}$ materiālam luminiscences dzēšana ir saistīta ar skābekļa tipa defektiem.

Darbā ir apskatīta ar Er^{3+} joniem aktivēta oksifluorīdu silikāta stikla keramika, ko iegūst, termiski apstrādājot sintezēto oksifluorīdu stiklu. Ir pētītas stikla un stikla keramikas AP luminiscences īpašības istabas temperatūrā un 50 K temperatūrā. Promocijas darbā ir secināts, ka AP procesā novērojamo enerģijas-pārdeves un ierosinātā-stāvokļa-absorbcijas mehānismu ieguldījums ir atkarīgs no temperatūras. Rezultātā ir piedāvāts kritērijs, kas nosaka viena vai otra AP luminiscences mehānisma dominanci stikla keramikas kristāliskajā fāzē.

List of Figures

1. **Fig. 3.1:** Interactions leading to different energy levels for Eu^{3+} ion (adapted from [46]).
2. **Fig. 3.2:** Emission spectra of Eu^{3+} in matrixes: (A) Eu^{3+} in water; (B) Eu(dipicolinic acid)$^{+}$ in water; (C) Eu(dipicolinic acid)$_3^{3-}$ in water [48].
3. **Fig. 3.3:** Energy level scheme of Er^{3+} ion in LaF_3 host matrix (adapted from [49]).
4. **Fig. 3.4:** Different processes, in which lower energy excitation radiation is converted into higher energy emission (adapted from [52]).
5. **Fig. 3.5:** (a) schematic ESA process in Er^{3+}, (b) ESA process with various intermediate levels, (c) ESA process with different energies of excitation photons.
6. **Fig. 3.6:** Schematic ETU process between Er^{3+} ions.
7. **Fig. 3.7:** Sensitized ETU process for Yb^{3+}-Er^{3+} ion pair.
8. **Fig. 3.8:** Energy level scheme for Er^{3+}, Yb^{3+} and Tm^{3+} ions system (adapted from [52]).
9. **Fig. 3.9:** Schematic CR process between two Er^{3+} ions.
10. **Fig. 3.10:** Schematic energy level configuration for power UC luminescence dependence explanation.
11. **Fig. 3.11:** Power dependence of the "green" and "red" UC luminescence bands of Er^{3+} in LaF_3 [54]
12. **Fig. 3.12:** Schematic energy level configuration.
13. **Fig. 3.13:** Non-radiative rate vs. energetic separation ΔE in different hosts.
14. **Fig. 3.14:** Graphical interpretation of (a) ESA, (b) ETU and (c) combination of ESA and ETU mechanisms in the temporal profiles of UC luminescence.
15. **Fig. 3.15:** Phase diagram of NaF-LaF_3 (adapted from [57]).
16. **Fig. 3.16:** The structure of $NaLaF_4$ represented as $Na_{1.5}La_{1.5}V_{Na}F_6$ crystal in the $P\bar{6}$ group [30].
17. **Fig. 4.1:** High temperature furnace Carbolite HTF 18/8.
18. **Fig. 4.2:** Nickel reactor used for the fluorination of samples.
19. **Fig. 4.3:** Shimadzu DTG-60 apparatus scheme [63].
20. **Fig. 4.4:** Window of the software developed to analyze excitation spectra.
21. **Fig. 5.1:** XRD pattern of 1% Er^{3+} doped $NaLaF_4$ polycrystalline material. The most intense peaks of $NaLaF_4$ are indexed.

22. **Fig. 5.2:** XRD pattern of $NaLaF_4:Er^{3+}$ material for samples with different LaF_3 and ErF_3 contents.
23. **Fig. 5.3:** Raman spectrum of undoped $NaLaF_4$ sample.
24. **Fig. 5.4:** Stationary UC luminescence spectrum of 2% Er^{3+} doped $NaLaF_4$ excited at 975 nm measured at room temperature.
25. **Fig. 5.5:** Power dependence of the transitions $^2H_{9/2} \rightarrow {}^4I_{15/2}$ (squares), $^4S_{3/2} \rightarrow {}^4I_{15/2}$ (circles) and $F_{9/2} \rightarrow {}^4I_{15/2}$ (triangles) in $NaLaF_4:Er^{3+}$ measured at room temperature.
26. **Fig. 5.6:** Decay profiles for (a) $^4S_{3/2} \rightarrow {}^4I_{15/2}$, (b) $^4F_{9/2} \rightarrow {}^4I_{15/2}$, (c) $^2H_{9/2} \rightarrow {}^4I_{15/2}$ optical transitions in $NaLaF_4:Er^{3+}$(0.5mol%) excited at 980 nm measured at room temperature.
27. **Fig. 5.7:** Schematic energy level diagram and the main radiative transitions in Er^{3+} ion. Full and dashed arrows are radiative and non-radiative transitions, respectively.
28. **Fig. 5.8:** Stationary UC luminescence spectra of Er^{3+} doped $NaLaF_4$ samples at different doping levels excited at 975 nm measured at room temperature.
29. **Fig. 5.9:** Decay profiles for the $^4S_{3/2} \rightarrow {}^4I_{15/2}$ optical transition in $NaLaF_4$ at different Er^{3+} concentrations: direct excitation at room temperature. Inset – double exponential fit of the decay for the sample with 4 mol% Er^{3+}.
30. **Fig. 5.10:** Decay profiles for the $^4F_{9/2} \rightarrow {}^4I_{15/2}$ optical transition in $NaLaF_4$ at different Er^{3+} concentrations: direct excitation at room temperature. Inset – double exponential fit of the decay for the sample with 4 mol% Er^{3+}.
31. **Fig. 5.11:** XRD pattern of $NaLaF_4$ powder at different synthesis stages. Vertical lines – recognized XRD peaks of LaF_3 (solid lines at the bottom), $NaLaF_4$ (solid lines in the upper part) and NaF (dotted line at the bottom).
32. **Fig. 5.12:** Evolution of the intensity of XRD peaks related to LaF_3 (squares) and $NaLaF_4$ (circles) crystalline phases.
33. **Fig. 5.13:** UC luminescence excited at 975 nm measured for the sample annealed at $650^{O}C$.
34. **Fig. 5.14:** "Green" UC luminescence excited at 975 nm measured for the samples annealed at different temperatures.
35. **Fig. 5.15:** Evolution of the intensity of the "green" UC luminescence band as the function of the annealing temperature.

36. **Fig. 5.16:** Normalized decay kinetics of the UC luminescence excited at 980 nm. Luminescence position set to 542 nm. Inset: initial part of the decay kinetics magnified.
37. **Fig. 5.17:** Evolution of the relative intensities of the decay components as the function of the annealing temperature.
38. **Fig. 5.18:** Absorption spectra measured for the samples annealed at different temperatures. Inset: integrated absorbance for the samples annealed at different temperatures.
39. **Fig. 5.19:** Normalized decay kinetics of the UC luminescence excited at 980 nm measured for the samples reannealed in fluorine atmosphere. Luminescence position set to 542 nm.
40. **Fig. 5.20.** "Green" UC luminescence excited at 975 nm measured for the sample annealed at different temperatures.
41. **Fig. 5.21:** DTA curve of the precursor glass. T_g – glass transition temperature, T_c – crystallization temperature.
42. **Fig. 5.22:** XRD pattern of the G (black line) and GC (red line) samples. The most intense LaF_3 diffraction peaks are denoted.
43. **Fig. 5.23:** UC luminescence spectra of the G (black line) and GC (red line) samples measured at a) RT and b) 50 K under 970 nm excitation.
44. **Fig. 5.24:** Excitation spectra of the UC luminescence at 539 nm measured for the GC sample at a) RT and b) 50 K. Vertical bars under the plots correspond to the transitions from different Stark sublevels of the ground state $^4I_{15/2}$ (energetic positions of the sublevels are given in the legend) to the Stark sublevels of the $^4I_{11/2}$.
45. **Fig. 5.25:** Excitation spectra of the luminescence at 539 nm measured for the GC sample at RT (black line) and 50 K (red line).
46. **Fig. 5.26.** Decay kinetics of the UC luminescence for the G (black line) and GC (red line) samples under 970 nm excitation measured at RT. Inset: magnified initial part of the decay kinetics. Luminescence position set to 539 nm.
47. **Fig. 5.27:** Decay kinetics of the UC and traditional luminescence for the GC sample under various excitation wavelengths measured at 50 K. Inset: magnified initial part of the decay kinetics. Luminescence position set to 539 nm.
48. **Fig. 5.28:** Energy level scheme of Er^{3+} ion in LaF_3 [49] and possible mechanisms of the UC luminescence in the crystalline phase of the GC sample at 50 K.

List of Tables

1. **Table 3.1:** Energy levels of Er^{3+} in LaF_3 host matrix (adapted from [49]).
2. **Table 3.2:** Physicochemical properties of different hosts prospective in UC applications.
3. **Table 3.3:** Characteristic phonon energies of different hosts [12].
4. **Table 4.1:** Physicochemical processes involving absorption of the heat (endothermic) or evolution of the heat (exothermic) [62].
5. **Table 5.1:** Lifetimes (in μs) of the main optical transitions in Er^{3+} doped $NaLaF_4$ samples at different doping levels and $NaErF_4$, measured under direct excitation at room temperature.

1. Introduction

1.1. Topicality and motivation for the research

Up-conversion process involves conversion of low-energy light photons into higher-energy light photons. This is being achieved by a "ladder" type stepwise excitation of a luminescent ion through sequential absorption of lower-energy photons followed by the emission of the accumulated energy in a form of luminescence. In this case the luminescence light has shorter wavelength (higher photon energy) than any of the absorbed photon. This type of luminescence has attracted interest of scientists since it was first recognized and treated by Auzel in 1966 [1]. Possible applications of the up-conversion luminescence involve but are not limited to visualization of infrared radiation [2], reading of x-ray reusable memory plates [3], 3-D display technology [4], white light simulation [5], temperature sensors [6], up-conversion lasers [7], biological markers [8], optical fiber amplifiers [9], enhancing the efficiency of solar cells [10] and others.

In principle any ion which has several discrete energy levels (transition metals, lanthanides, actinides) might be used in up-conversion processes [11], when incorporated in, for example, a solid state material. Rare-earth ions and particularly Er^{3+} ion is the most recognized and often used for up-conversion purposes. It is for a series of nearly equidistant energy levels of Er^{3+}, which make it perfectly suited for up-conversion excitation and thus desirable as an activator in many different hosts.

Depending on particular application different classes of the host matrixes must be used. For example, if the material is expected to be used as an active medium for laser, than it must be of high optical durability and heat resistance, while fine granularity rather than the durability is of great importance if the material is used as a luminescent display. In any case, **materials characterized by high efficiency of the up-conversion luminescence are persistently searched for.**

Low-phonon energy media, which can be doped with rare-earth ions, are attractive hosts for up-conversion purposes, because they enable emissions from rare-earth ion energy levels that are not quenched by multi-phonon relaxations as it is in high-phonon energy materials [12]. Shalav et al. [10] has shown that heavy halides of lanthanum (LaI_3, $LaBr_3$, $LaCl_3$) are featured by high efficiency of the up-conversion luminescence. The high efficiency can be explained by the reduced rate of non-radiative transitions in the materials due to small phonon energy of the hosts and also by the possibility of effective doping of the materials due to the affinity of La^{3+} to any other trivalent rare-earth activators. However, extremely high sensitivity of the heavy halides towards moisture diminishes their chances to become widely used in various applications.

Fluorides, belonging to the class of halides, are characterized by much lower hygroscopicity compared to their heavier counterparts still possessing a small phonon energy required for an efficient up-conversion process. These facts make the **rare-earth doped La^{3+} containing fluorides attractive media for up-conversion purposes.**

Up-conversion luminescence was studied in many rare-earth doped heavy fluorides (LaF_3 [13], GdF_3 [14], YF_3 [15], BaF_2 [16], CaF_2 [17], $BaYF_5$ [18], SrF_2 [19], PbF_2 [20], $NaGdF_4$ [21] and some others). Rare-earth doped $NaYF_4$ is one of the most prospective and extensively studied materials among the efficient up-conversion luminophors [11, 22-25]. At room temperature two types of stable lattice structures are reported for $NaYF_4$: cubic and hexagonal [26, 27]; the efficiency of the up-conversion luminescence in the hexagonal phase is about 10 times higher than that reported for the cubic [22]. The high efficiency of the up-conversion process in the hexagonal $NaYF_4$ is explained partly because of the small effective phonon energy of the medium (~360 cm^{-1} [11]) and partly due to the multisite nature of $NaYF_4$ crystalline lattice, meaning that rare-earth ions can occupy various non-equivalent states in the crystalline lattice [28, 29], thus enhancing the efficiency of the up-conversion process.

Compared to $NaYF_4$ up-conversion properties of rare-earth doped $NaLaF_4$ up to now have not been extensively studied. $NaLaF_4$ doped with Er^{3+} and Yb^{3+} was first examined as an up-conversion host in 1972 [26], however **no** further studies of the up-conversion luminescence in rare-earth doped $NaLaF_4$ have followed. The similarity in chemical composition of $NaLaF_4$ and $NaYF_4$ ($Y^{3+} \leftrightarrow La^{3+}$) as well as

their isostructure ($NaLaF_4$ has a hexagonal lattice structure [30]) predict **rare-earth doped $NaLaF_4$ to be an efficient up-conversion host.** Moreover, the existence of exclusively hexagonal structure of $NaLaF_4$ suggests easier synthesis routine of the material while the existence of both the cubic and hexagonal crystalline structures of $NaYF_4$ stable at room temperature sometimes makes the synthesis of the purely hexagonal $NaYF_4$ rather problematic [10, 31]. The above mentioned considerations make **the synthesis of rare-earth doped $NaLaF_4$ and the studies of the up-conversion processes in the material important and prospective for future development of new effective up-conversion media.**

Rare-earth doped fluorides in powder form are prospective materials to be used as efficient up-conversion luminophors, for example, in luminescent displays. However some applications require synthesis of large size **transparent** media with efficient up-conversion properties. Rather high temperatures and special (oxygen-free) atmosphere conditions required for the synthesis of large size and highly durable bulk fluoride crystals make the production of the materials a challenging task. Additionally, limited fusion-spliceability of the bulk fluorides to conventional telecommunication fibres diminishes chances for the materials to be used in photonics applications.

The synthesis of large size rare-earth doped glasses, for example silicate glasses, is much easier; the synthesis usually occurs at lower temperature and therefore the synthesis procedure is cost-effective and energy-efficient. Finally, the affinity of the silicate glass to the optical fibres opens up the possibility for the material to be used in the field of telecommunication and optical signal processing.

Despite much easier synthesis routine, rare-earth doped silicate glasses suffer from increased probability of non-radiative transitions within luminescent rare-earth ions related to rather high phonon energies of the matrix. As a result the efficiency of the up-conversion luminescence observed in rare-earth doped silicate glasses is usually small.

Transparent oxyfluoride glass ceramics, having rare-earth doped fluoride nanocrystals embedded in a silicate matrix, provides both the high efficiency of the up-conversion process (the efficient up-conversion luminescence occurs in the fluoride nanocrystals) and excellent chemical, mechanical and durability properties of the silicate glass [12].

Conventional synthesis of an oxyfluoride glass ceramics [12] involves annealing of the initially properly composed precursor oxyfluoride glass at certain temperature corresponding to the crystallization of the glass. The heat treatment of the glass triggers the formation of rare-earth doped fluoride nanocrystals.

Different oxyfluoride ceramics systems have been synthesized with PbF_2 [32-34], CaF_2 [35-38], BaF_2 [39-41] crystallites doped with various rare-earth dopants since the first oxyfluoride glass ceramics was reported [42]. A group of Wang have succeeded in the preparation of an oxyfluoride silicate ceramics, which contains Er^{3+} doped LaF_3 nanocrystals. Various properties of this system related to the synthesis of the material and up-conversion processes have been thoroughly studied at room temperature [43-45]. At present, no results on the studies of the up-conversion luminescence performed at low temperatures in this system have been published. **The studies of the up-conversion luminescence in oxyfluoride glass ceramics at low temperatures might be of great importance to understand the true nature of the up-conversion processes occurring in the material that are otherwise impossible to observe at higher temperatures.**

1.2. Main goals and tasks of the work

The main focus in this work is set on two representatives of the most prospective classes of up-conversion hosts: erbium doped $NaLaF_4$ crystalline material and erbium doped transparent oxyfluoride glass ceramics containing LaF_3 nanocrystallites.

The goals of the present work are to **study the up-conversion luminescence in Er^{3+} doped $NaLaF_4$** and **study the up-conversion luminescence properties of Er^{3+} doped oxyfluoride glass ceramics at different temperatures.** To achieve the goals the following tasks were set:

- synthesize Er^{3+} doped $NaLaF_4$,
- develop a novel synthesis method for $NaLaF_4:Er^{3+}$,
- study the structure of $NaLaF_4:Er^{3+}$ and the influence of the structure on the up-conversion luminescence properties of the material at different Er^{3+} doping levels,
- study possible impact of oxygen related defects on the up-conversion properties of $NaLaF_4:Er^{3+}$,

- synthesize Er^{3+} doped oxyfluoride glass and glass ceramics with LaF_3 nanocrystallites,
- study the up-conversion luminescence properties of the oxyfluoride glass and glass ceramics at different temperatures.

1.3. Novelty of this work

Experimental investigations performed in this work allowed to:

- develop a novel synthesis technique of $NaLaF_4:Er^{3+}$ material without using a hydrofluoric acid,
- identify the impact of oxygen related defects on the UC luminescence of $NaLaF_4:Er^{3+}$,
- establish regularities leading to the dominance of either excited state absorption or energy transfer mechanisms of the UC luminescence in Er^{3+} doped oxyfluoride glass ceramics at different temperatures.

1.4. Author contribution

Synthesis of all the samples mentioned in this work, measurements of up-conversion and photoluminescence spectra, excitation spectra and luminescence kinetics, differential thermal analysis, x-ray diffraction patterns as well as the analysis of the obtained results have been performed solely by the author.

Raman spectrum of $NaLaF_4$ material was measured by dr.phys. Georgijs Čikvaidze, infrared absorption spectra of $NaLaF_4$ materials were measured by dr.habil.phys. Larisa Grigorjeva.

2. Acronyms

UC	up-conversion
GSA	ground state absorption
ESA	excited state absorption
ET	energy transfer
ETU	energy transfer up-conversion
XRD	x-ray diffraction
DTA	differential thermal analysis
IR	infrared
VIS	visible
UV	ultraviolet
CW	continuous wave
RE	rare-earth
RT	room temperature
G	glass
GC	glass ceramics

3. Physical background

3.1. Rare-earth elements

RE elements is a collection of 17 elements, namely, scandium (Sc), yttrium (Y), lanthanum (La), cerium (Ce), praseodymium (Pr), neodymium (Nd), promethium (Pm), samarium (Sm), europium (Eu), gadolinium (Gd), terbium (Tb), dysprosium (Dy), holmium (Ho), erbium (Er), thulium (Tm), ytterbium (Yb) and lutetium (Lu). Mostly trivalent, the ions of the respective elements hold a special place in photonics and applications because of their unique luminescence properties when used as activators in various solid state materials [46].

The electronic configuration of Sc^{3+} is equivalent to Ar, Y^{3+} to Kr, and La^{3+} to Xe. The ions from Ce^{3+} to Lu^{3+} have one to fourteen 4f electrons sequentially added to their inner shell configuration, which is equivalent to Xe. Sc^{3+}, Y^{3+}, La^{3+}, and Lu^{3+}, have no electronic energy levels that can induce excitation and luminescence processes around the visible region. In contrast, the ions from Ce^{3+} to Yb^{3+}, which have partially filled 4f orbitals, have energy levels characteristic of each ion and show a variety of luminescence properties in or near the visible region. Many of these ions can be used as luminescent ions in optical materials, mostly by replacing Y^{3+}, Gd^{3+}, La^{3+}, and Lu^{3+} in various compound crystals [47]. The luminescence spectra of RE ions usually are characterized by sharp peaks, whose spectral positions are almost independent on the embedding host matrix. The relative intensities and the fine structure of the luminescence peaks, however, may vary [46].

As it was mentioned, going from La^{3+} to Lu^{3+}, the 4f orbitals are sequentially filled with electrons. These orbitals are shielded by the electrons in the 5s and 5p shells, which are lower in energy, but spatially located outside the 4f orbitals. The electronic transitions that are responsible for the line-like absorption and luminescence spectra are transitions within the $4f^n$ configuration, and therefore are only slightly affected by the matrix due to effective shielding of the transitions by 5s and 5p electrons. The occurrence of the different energy levels belonging to the same configuration is a result of several interactions within the ion. An example of such interactions leading to the different electronic energy levels for one of RE ions (Eu^{3+}) is shown in **Fig. 3.1**. [46].

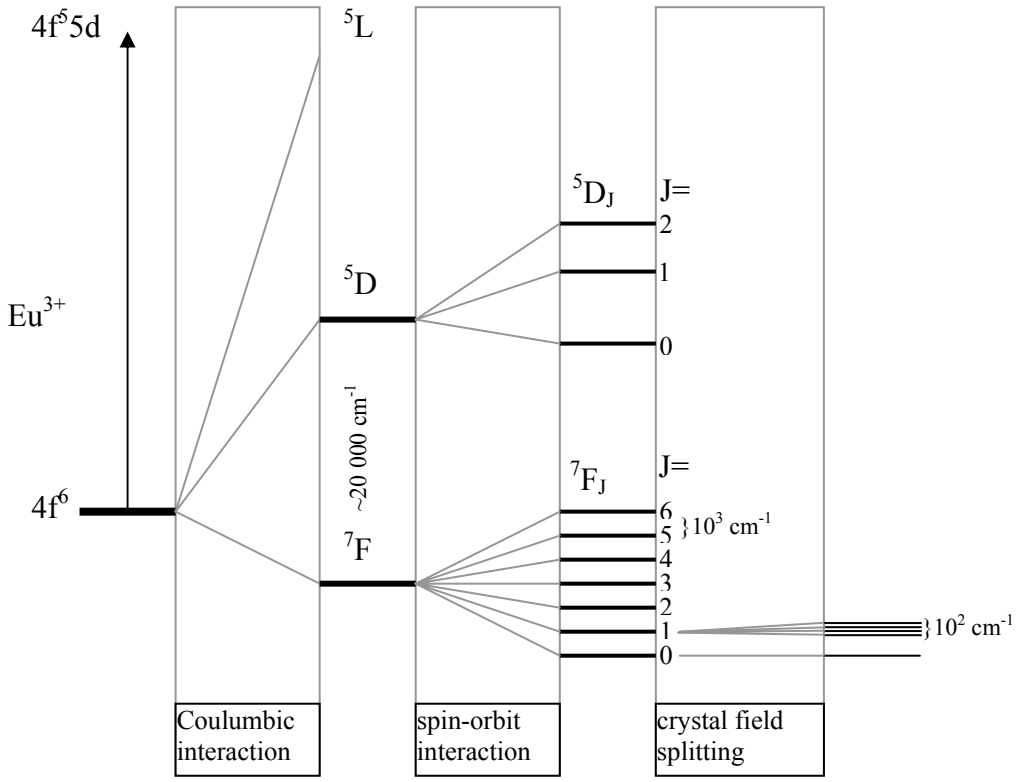

Fig. 3.1: Interactions leading to different energy levels for Eu^{3+} ion (adapted from [46]).

The Coulombic or electrostatic interaction, representing repulsions of the electrons within the 4f orbitals, is the most significant among the 4f electronic interactions and it gives rise to terms (in **Fig. 3.1** indicated as ^7F, ^5D and ^5L) with a separation in the order of 10^4 cm^{-1}. Afterwards additional splitting of the terms into several J-levels is done by spin-orbit coupling, which is relatively large (10^3 cm^{-1}) in lanthanide ions (in **Fig. 3.1** indicated as $^7F_{6,5,4,3,2,1,0}$ and $^5D_{2,1,0}$). Finally, when the rare-earth ion is incorporated into a coordinating environment, such as a crystalline or glass lattice, the individual J-levels undergo further splitting by the electric field of the matrix (so-called crystal field). These splittings are usually smaller than the previously mentioned (10^2 cm^{-1}) and they become present as a fine structure on the individual bands [46].

Strongly speaking, the radiative transitions in a "free" lanthanide ion are parity forbidden. This means that electric dipole transitions within the 4f level (with the same parity) are dipole-forbidden. However, once a RE ion is doped into a coordination matrix (for example, crystal or glass host), some of these transitions become weakly allowed due to mixing of the parity configuration by the crystalline

field. The weakly allowed transitions are the reason for the long lifetimes (in the millisecond range) usually observed for the energy levels of the RE ions doped into a coordination matrix [10]. Most of the observed absorption and emission lines of RE ions are such induced weakly allowed electric dipole transitions [46].

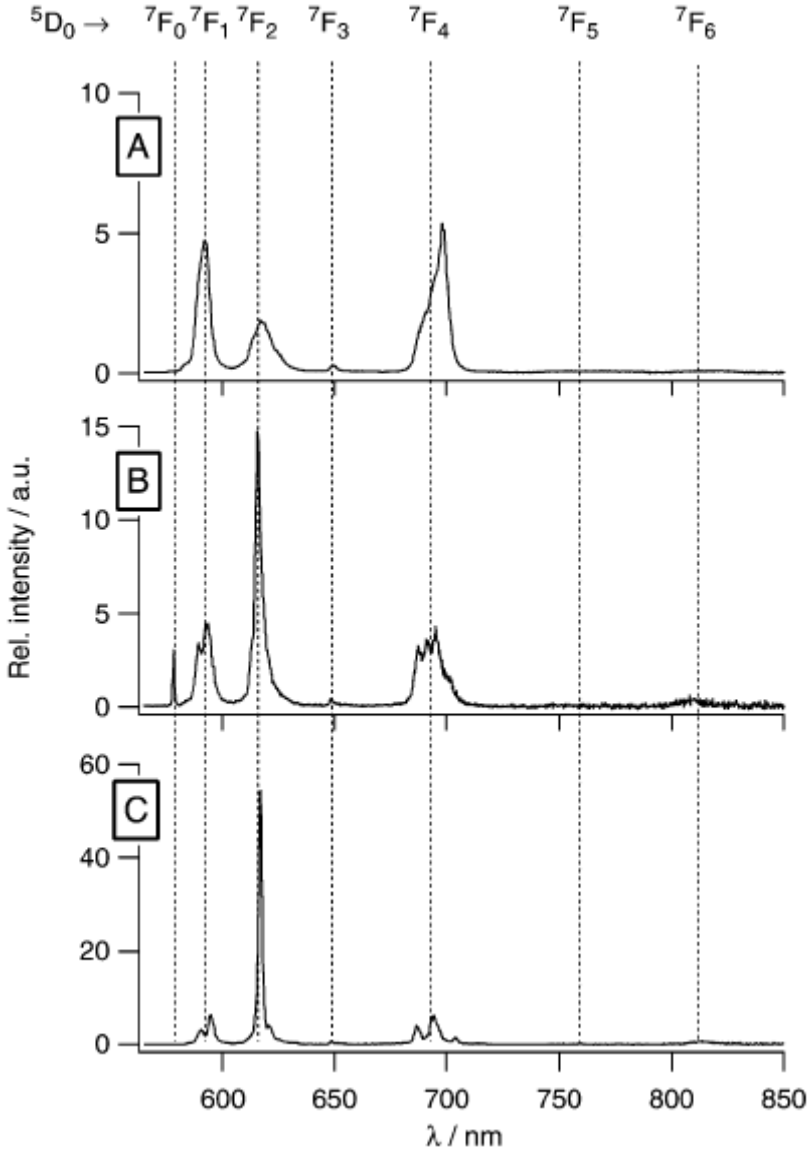

Fig. 3.2: Emission spectra of Eu^{3+} in matrixes: (A) Eu^{3+} in water; (B) Eu(dipicolinic acid)$^+$ in water; (C) Eu(dipicolinic acid)$_3^{3-}$ in water [48].

Since electric dipole transitions in RE ions are induced by the crystalline field, their probabilities are very sensitive to it. The intensities of some of these transitions are highly sensitive to the coordinating environment, which means that their intensities can vastly vary, depending on the coordination field. An example of such a hypersensitive transition is the $^5D_0 \rightarrow {}^7F_2$ emission line of Eu^{3+} (**Fig. 3.2**) [48].

3.2. Erbium

Er^{3+} ion is one of the most extensively studied RE ions as an activator in various hosts. In the remaining of this section general information about the luminescence properties of Er^{3+} will be given. The energy levels of Er^{3+} in LaF_3 host matrix and their positions are summarized in **Fig. 3.3** and **Table 3.1** [49].

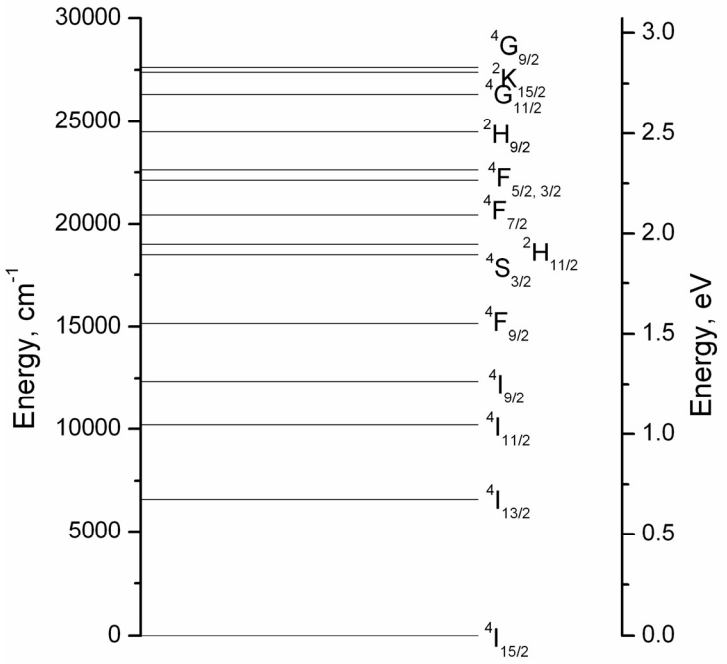

Fig. 3.3: Energy level scheme of Er^{3+} ion in LaF_3 host matrix (adapted from [49]).

From the indicated transitions one of the most important in the field of communication technologies is the transition at 1520 nm ($^4I_{13/2}$), which is used in erbium doped fiber amplifier – an optical amplifier that uses an Er^{3+} doped optical fiber as a gain medium to amplify an optical signal. This type of amplifiers is related to fiber lasers, where the core of a silica fiber is doped with Er^{3+}. Er^{3+} doped silica can be efficiently pumped with a laser at a wavelength of 980 nm or 1480 nm, and it exhibits gain in the 1550 nm region. Amplification of a signal is achieved by stimulated emission of photons from Er^{3+} in the doped fiber. The pumping laser excites ions into a higher energy ($^4I_{15/2} \rightarrow {}^4I_{13/2}$ or $^4I_{15/2} \rightarrow {}^4I_{11/2}$) from where a stimulated emission of a photon (at the wavelength of the signal) back to a ground state occurs. The energetic position of $^4I_{13/2}$ level lies in a strategic region related to a

so-called “low loss optical window” of silica based fiber, making the erbium doped fiber amplifier the best known and most frequently used optical amplifier [50].

Table 3.1: Energy levels of Er^{3+} in LaF_3 host matrix (adapted from [49]).

Nr.	Notation	Wavelength, nm (*)	Energy, eV (*)
1	$^4I_{15/2}$	ground state	0
2	$^4I_{13/2}$	1520	0.816
3	$^4I_{11/2}$	980	1.265
4	$^4I_{9/2}$	810	1.531
5	$^4F_{9/2}$	660	1.879
6	$^4S_{3/2}$	540	2.296
7	$^2H_{11/2}$	526	2.358
8	$^4F_{7/2}$	489	2.536
9	$^4F_{5/2}$	452	2.743
10	$^4F_{3/2}$	442	2.805
11	$^2H_{9/2}$	408	3.038
12	$^4G_{11/2}$	380	3.264
13	$^2K_{15/2}$	365	3.398
14	$^4G_{9/2}$	362	3.427

(*) the wavelength and the photon energy are indicated for the transitions from the specific level to the ground state. The indicated values are averaged.

Other important radiative transitions of Er^{3+} ion lie in the “green” ($^4S_{3/2}\rightarrow{}^4I_{15/2}$) and “red” ($^4F_{9/2}\rightarrow{}^4I_{15/2}$) spectral regions[1]. The presence of the luminescence in these strategic regions opens up a possibility to utilize Er^{3+} doped materials in the field of luminophors. There are several ways how the “green” and “red” luminescence of an Er^{3+} doped material can be excited. One of the ways is a traditional luminescence, when the luminescence is excited by light with a wavelength corresponding to the transitions from the ground state to one of the excited states above the “green” and the “red” states ($^4I_{15/2}\rightarrow{}^4F_{7/2}$, $^4F_{5/2}$, $^4F_{3/2}$, $^2H_{9/2}$ etc.).

[1] In principle the radiative transitions in the violet (~ 410 nm) and blue (~ 450nm, 480 nm) can be also observed in Er^{3+} , however, their intensities usually are considerably smaller than those of the “green” and the “red”

Another possibility, how the “green” and the “red” luminescence can be excited, is a so-called UC process, in which the VIS luminescence is excited by IR radiation. The UC process will be discussed in the following section of this chapter.

3.3. Up-conversion luminescence in rare-earth ions

All fluorescence light emitters usually follow the well-known principle of the Stokes law which simply states that excitation photons are at a higher energy than emitted ones or, in other words, that output photon energy is lower than input photon energy [51]. Nevertheless there are some exceptions (so called anti-Stokes emissions) when the conversion of photons of a given energy into greater-energy ones might be possible.

It is better to first divide them into different types, according to the physical mechanisms responsible for the process [52]. Physically, these conversion processes can be divided into two types: single-photon or multi-photon processes. A single-photon conversion process stands for anti-Stokes emission frequently observed in Raman spectra of solid state materials, where one photon of lower energy is absorbed and subsequently emitted at higher energy (**Fig. 3.4a**). The additional energy is usually provided by the lattice vibration quanta (phonons), which have very specific energies corresponding to the phonon spectrum of the host lattice. Although some measurement techniques, for example, Coherent Anti-Stokes Raman Spectroscopy, employ single-photon conversion method, in general the efficiency of the effect usually is low and the process will not be discussed in detail.

Multi-photon conversion is another class of the anti-Stokes emissions, in which two or more incident photons are absorbed in a medium and one photon of higher energy is emitted.

Second harmonic generation (**Fig. 3.4b**) is a process, in which incident photons interact with a nonlinear material to “effectively” combine and form photons with twice the energy of the incident photons. Since both the intermediate and the final states are virtual ones, the two photons to be combined must coincide in frequency and must be coherent. Such conditions can be reached under laser excitation, which is why the second harmonic generation is extensively used in laser industry. The most

famous example is 532 nm “green” emission, which appears by doubling the frequency of fundamental 1064 nm emission of YAG:Nd^{3+}.

Two-photon absorption process (**Fig. 3.4c**) occurs when the energy of one photon is not sufficient to bridge the gap between the ground and the final excited state but the total energy of two photons is enough. Both the ground and the final states are “real” ones and it is not necessary that the photons are of the same energy or are coherent as it was in the second harmonic generation. Nevertheless, the two-photon absorption process requires rather high excitation intensity, which is the reason why the process is not an “everyday phenomena”.

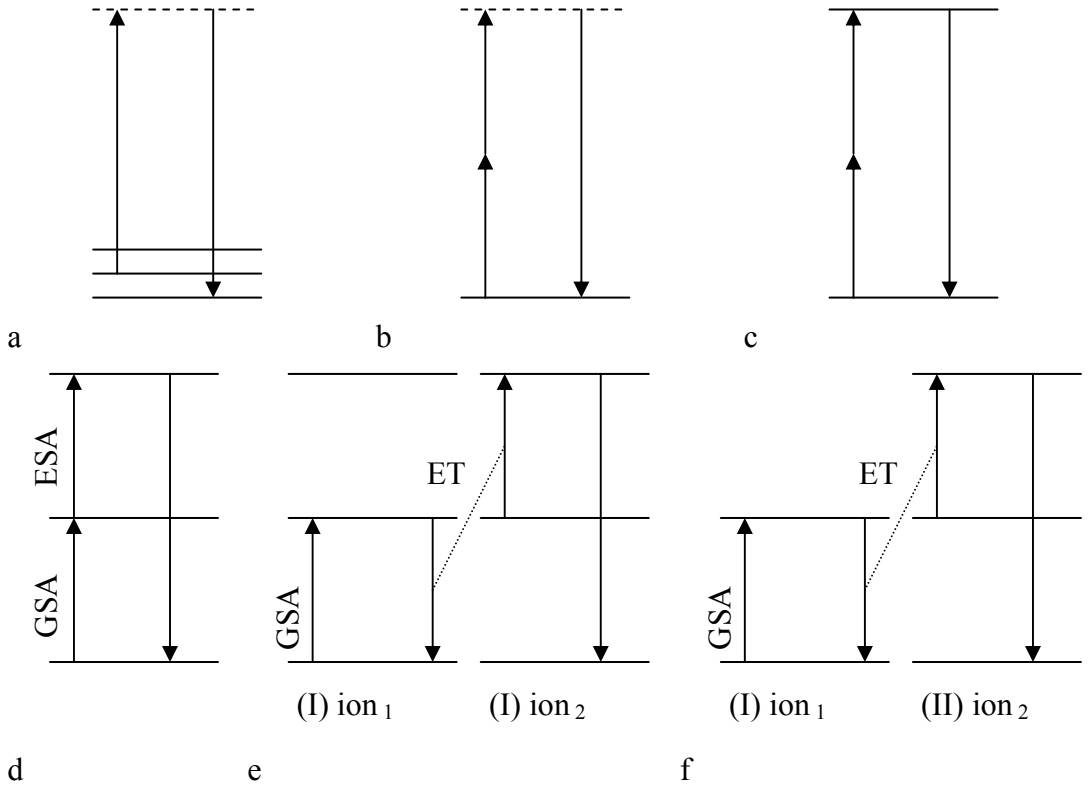

Fig. 3.4: Different processes, in which lower energy excitation radiation is converted into higher energy emission (adapted from [52]).

(a) anti-Stokes Raman emission,

(b) second harmonic generation

(c) multi-photon absorption

(d) ESA

(e) ETU

(f) sensitized ETU

The remaining mechanisms shown in **Fig. 3.4** are two-photon UC processes (ESA and ETU) that will be later referred in the experimental part of the work. Here they will be discussed more in detail.

The states involved in the both ESA and ETU UC processes, namely, ground, intermediate and excited states are all "real" levels. Examples of different mechanisms of UC luminescence in Er^{3+} will be shown.

3.3.1. Excited state absorption

ESA process shown in **Fig. 3.4d** is a result of GSA, i.e. electron transition from the ground state to the intermediate state, followed by ESA, i.e. electron transition from the intermediate state to the final excited state.

In **Fig. 3.5a** one of the possible ESA processes in Er^{3+} is shown.

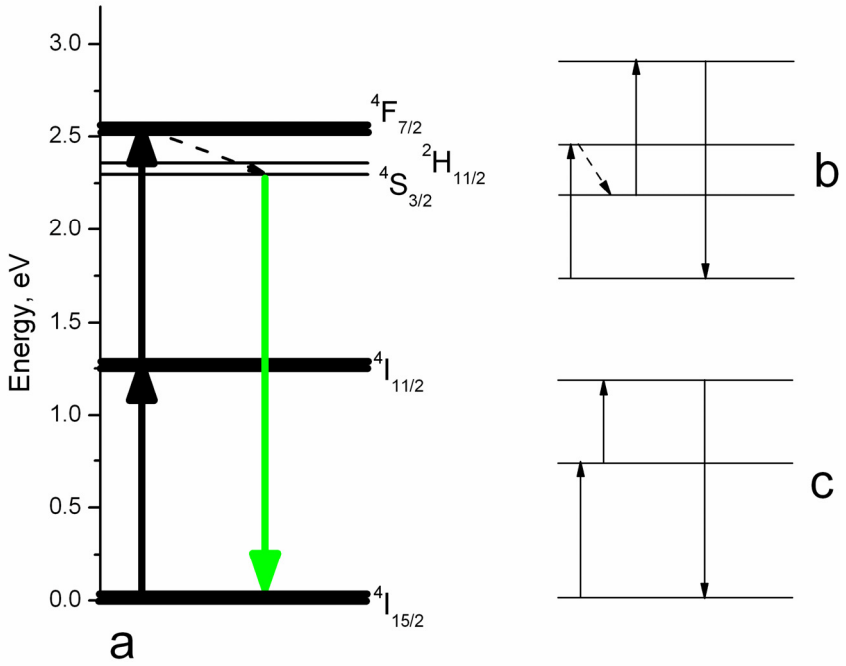

Fig. 3.5: (a) schematic ESA process in Er^{3+}, (b) ESA process with various intermediate levels, (c) ESA process with different energies of excitation photons. Full and dashed arrows are radiative and non-radiative transitions, respectively.

The excitation of Er^{3+} at around 980 nm (1.25 eV) corresponds to electronic transition from $^4I_{15/2}$ to $^4I_{11/2}$. Later a photon of approximately the same energy can realize the transition from $^4I_{11/2}$ to $^4F_{7/2}$. The non-radiative decay from $^4F_{7/2}$ to $^2H_{11/2}$ and $^4S_{3/2}$ populates the two levels and after the electronic transition to the $^4I_{15/2}$ the "green" UC luminescence appears. As a result IR radiation is up-converted into the

VIS. The intermediate level (in the case of Er^{3+} it is $^4I_{11/2}$) plays an important role in the ESA process – this level must have a lifetime long enough for an excitation to be stored in the ion until the next photon realizes the transition to the final excited state. As a rule of thumb, the lifetime of about tens of microseconds for the intermediate level is enough to observe an efficient ESA mechanism [52].

The described ESA process in Er^{3+} is a specific case of a general scheme, where, for example, several intermediate levels might be involved (**Fig. 3.5b**), or photons of different energies are used to populate the final excited state (**Fig. 3.5c**). ***The main characteristic feature of the ESA mechanism is that the UC process occurs within a single ion.***

3.3.2. Energy transfer up-conversion

ETU process occurs between two ions, one of which is already in the intermediate state (**Fig. 3.4e** and **Fig. 3.4f**). Depending on whether the ions are of the same kind or are different the ETU mechanism can be simply ETU or sensitized ETU, respectively.

In **Fig. 3.6** one of the possible ETU mechanisms in the system of two Er^{3+} ions is shown.

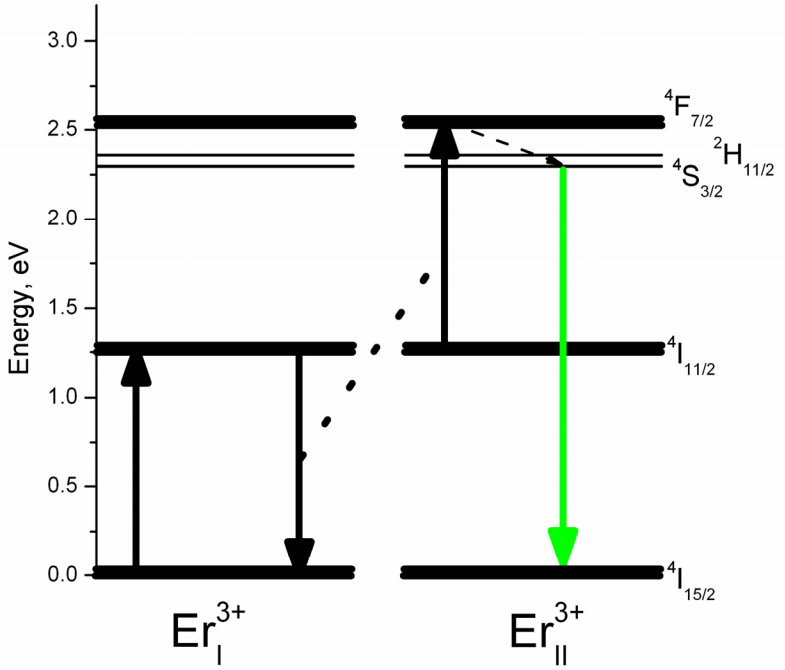

Fig. 3.6: Schematic ETU process between Er^{3+} ions. Full and dashed arrows are radiative and non-radiative transitions, respectively.

Again excitation at around 980 nm (1.25 eV) brings two Er^{3+} in the first excited state. Afterwards one of the ions de-excites to the ground state (Er^{3+}_{I}) while the second ion (Er^{3+}_{II}) is excited to the higher-energy state. In this case the energy from one ion is being transferred to another ion by so-called Coloumb interaction. Considering two ions as dipoles the probability of such interaction drops off as R^{-6}, where R – is the distance between the ions [51]. This fact suggests that the efficiency of the ETU process depends on the concentration of the active ions: the higher the concentration, the smaller is the distance between the ions, the higher probability of the ETU process.

3.3.3. Sensitized energy transfer up-conversion

The sensitized ETU process is similar to the simple ETU with the difference that the two ions involved in the process are not identical. In **Fig. 3.7** the sensitized ETU process for Yb^{3+}-Er^{3+} ion pair is shown.

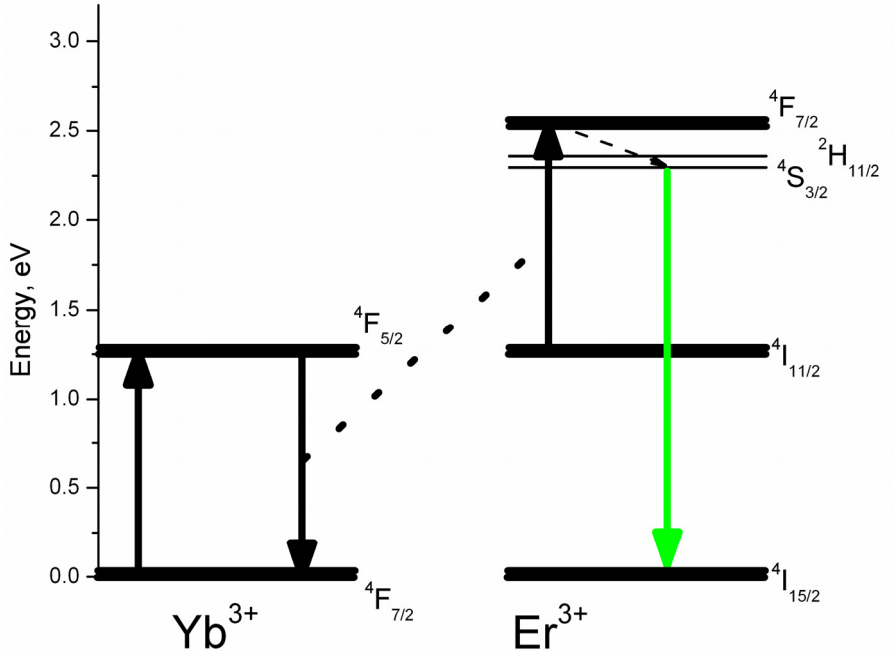

Fig. 3.7: Sensitized ETU process for Yb^{3+}-Er^{3+} ion pair. Full and dashed arrows are radiative and non-radiative transitions, respectively.

Under excitation at about 980 nm (1.25 eV) both ions are brought to the excited states (Yb^{3+} – to $^4F_{5/2}$, Er^{3+} – to $^4I_{11/2}$). Subsequent de-excitation of Yb^{3+} ion to the ground state and energy transfer to the Er^{3+} ion brings the latter to the higher-excited state.

More complex scheme of sensitized ETU process for Er^{3+}, Yb^{3+} and Tm^{3+} system is shown in **Fig. 3.8** [52]. The excitation at about 980 nm promotes Yb^{3+} ion in the excited state. Afterwards series of ETU processes from Yb^{3+} to Er^{3+} and Tm^{3+} and non-radiative decays within the ions take place. Finally the radiative transitions in Er^{3+} ($^2H_{9/2} \rightarrow {}^4I_{15/2}$, $^4S_{3/2} \rightarrow {}^4I_{15/2}$ and $^4F_{9/2} \rightarrow {}^4I_{15/2}$) and Tm^{3+} ($^1D_2 \rightarrow {}^3F_4$ and $^1G_4 \rightarrow {}^3H_6$) produce the luminescence in the "violet", "green", "red" and "blue" spectral regions.

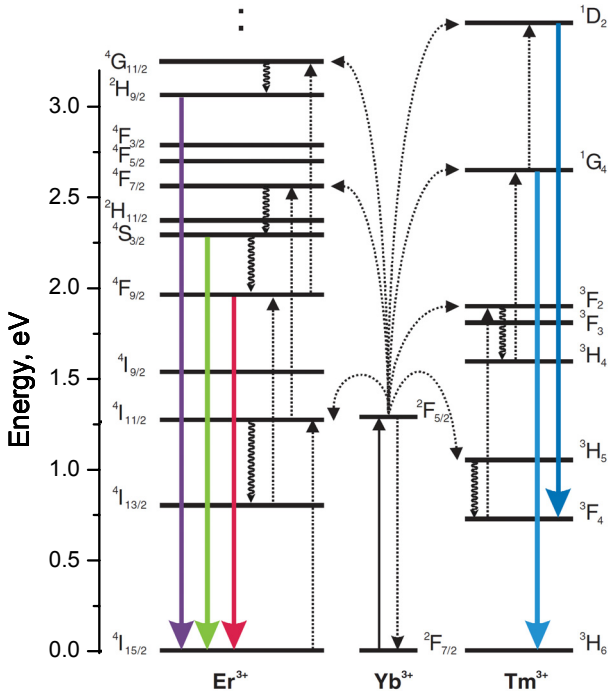

Fig. 3.8: Energy level scheme for Er^{3+}, Yb^{3+} and Tm^{3+} ions system (adapted from [52]). Solid arrows – radiative processes (upward – excitation, downward – emission), dotted arrows – ET, curled arrows – non-radiative transitions.

3.3.4. Cross-relaxation

CR is another type of energy transfer in which two ions are involved. The main difference between CR and ETU are the final states, to which the ions involved in the

processes arrive. After ETU one of the ions is in a higher energy state than either of the ions was before the process. This is not the case for CR process, when both ions are in lower excited state(s) than one of the ions was prior to the CR. One of the CR processes in Er^{3+} ion is shown in **Fig. 3.9**. Before the CR process one of the ions is in the $^4F_{7/2}$ state (the highest) while the other is in the ground state. After the CR process both of the ions are in $^4I_{11/2}$ energy state. Since the energy of $^4I_{11/2}$ is lower than that of $^4F_{7/2}$ the observed process is CR [52].

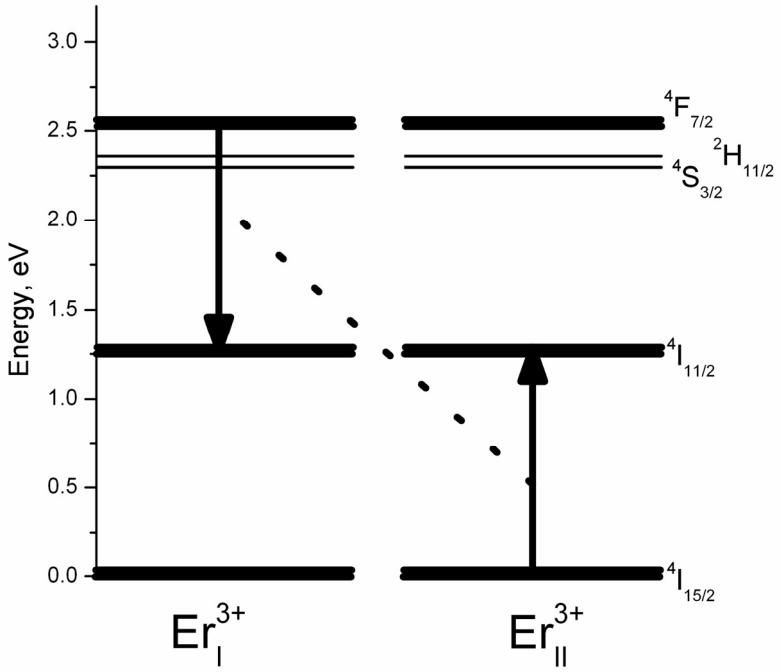

Fig. 3.9: Schematic CR process between two Er^{3+} ions.

3.3.5. Comparison between excited state absorption and energy transfer up-conversion

The efficiency of an ESA process is defined only by the energy level structure of a specific active ion. In general the cross-section of an ESA UC luminescence can be written as:

$$\sigma_{GSA/ESA} \propto \sigma_{GSA} \cdot \sigma_{ESA}, \tag{3.1}$$

where σ_{GSA} is the GSA absorption cross-section, σ_{ESA} is the ESA absorption cross-section and $\sigma_{GSA/ESA}$ is the cross-section of the ESA UC luminescence emission. Equation (3.1) means that for a given excitation wavelength (energy) the efficient

ESA UC luminescence will be observed only in the case when there is an efficient overlap between GSA and ESA [52].

In ETU process two ions are involved. The interaction between the ions occurs in a host matrix and it was found that efficient ETU process can take place at energy mismatches between GSA and ESA as high as several thousand reciprocal centimeters [51]. In general the probability of an ETU UC luminescence can be written as:

$$W_{ETU} \propto e^{-\beta \Delta E}, \tag{3.2}$$

where β is a lattice dependent constant and ΔE – energy mismatch between both ions [51].

3.4. Properties of up-conversion luminescence

3.4.1. Power dependence of up-conversion luminescence

The intensity of the traditional luminescence is directly proportional to the intensity of the excitation light. This is not the case for the UC luminescence, where the dependence of the luminescence intensity on the excitation power might be considerably more complex.

The excitation power dependence of the UC emission intensity for different mechanisms of the UC luminescence was analyzed in detail by Pollnau et al. [53]. Here, for the sake of simplicity, a case of ESA UC luminescence will be explored, however, similar analysis of ETU process (treated in details in [53]) leads to the same conclusions (**Fig. 3.10**).

Consider a system having 4 equidistant energy levels (E_0, E_1, E_2, E_3). If the system is excited with the radiation of energy equal to the difference between the levels ($E = E_2 - E_1$), electron transitions from the ground state (E_0) to excited state (E_1) will be observed. Assuming the population of the ground state tending to infinity, the population of the E_1 will be directly proportional to the intensity of the excitation light:

$$N_1 \propto I_{exc} \tag{3.3}$$

The intensity of the luminescence from this level to the ground state will be proportional to the population of the level:

$$I_{lum} \propto I_{exc} \tag{3.4}$$

The population of the E_2 level will be proportional to the product of the population of E_1 level and the intensity of the excitation light. Taking into account equation (3.4) one gets:

$$N_2 \propto N_1 \cdot I_{exc} \propto I_{exc}^{\ 2} \tag{3.5}$$

In this case the intensity of the luminescence from this level to the ground state will be:

$$I_{lum} \propto I_{exc}^{\ 2} \tag{3.6}$$

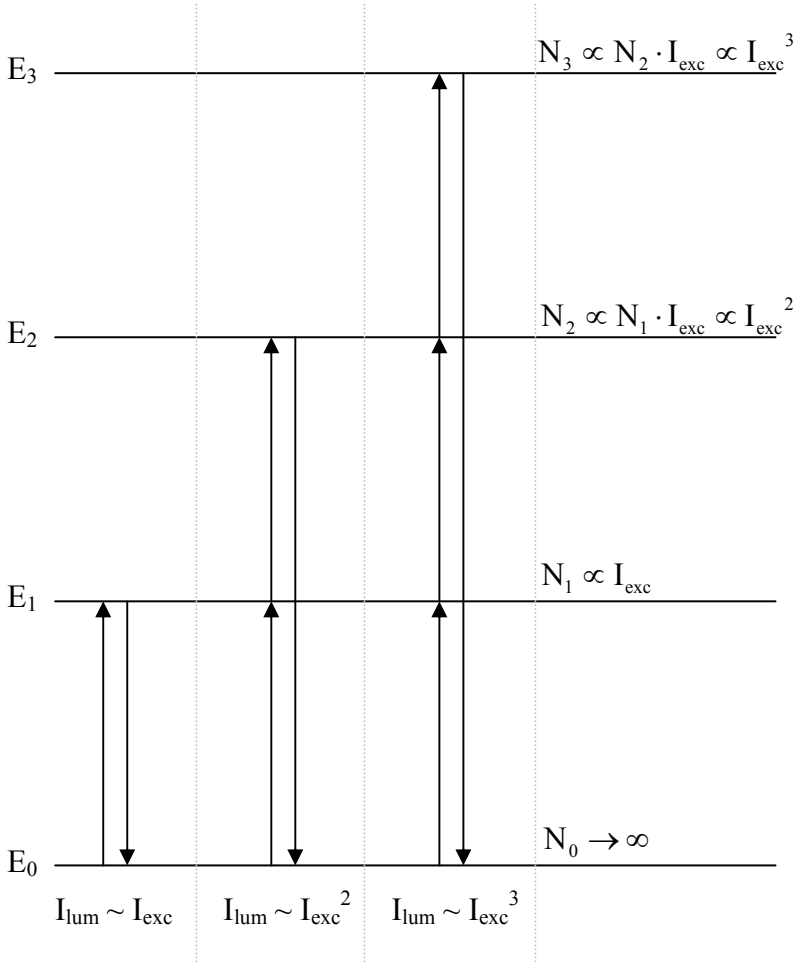

Fig. 3.10: Schematic energy level configuration for power UC luminescence dependence explanation.

Similarly, if 3 photon absorption is involved in the creation of the UC luminescence, the intensity of the luminescence will have cubic dependence on the excitation power:

$$I_{lum} \propto I_{exc}^{\ 3} \tag{3.7}$$

As a result the experimentally measured intensity dependence of UC luminescence on the intensity of the excitation light allows to determine the number of photons required for the population of the luminescence level.

The power dependences of the UC luminescence usually are shown in double-logarithmic plots, where the power-law dependence transforms into a linear function (**Fig. 3.11**).

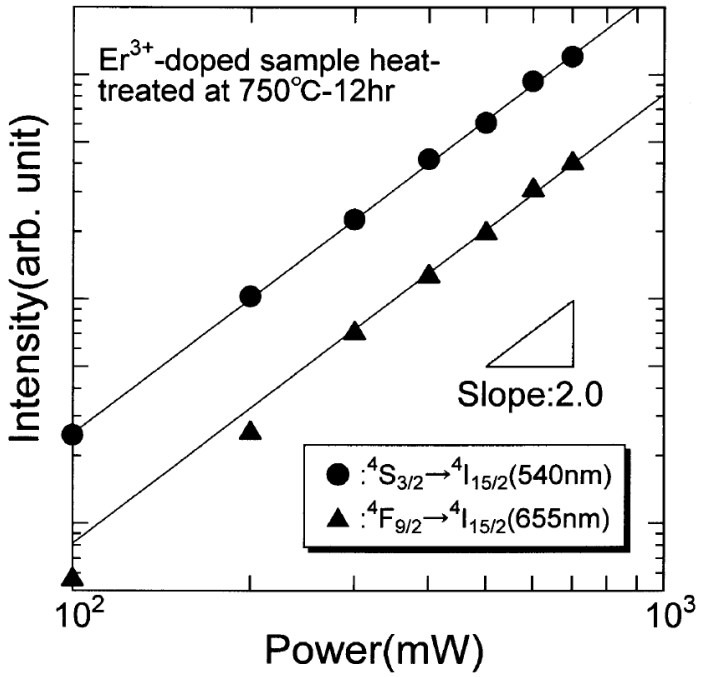

Fig. 3.11: Power dependence of the "green" and "red" UC luminescence bands of Er^{3+} in LaF_3 [54]

Detailed studies [53] revealed that under high excitation densities or for the systems with extremely high rate of the UC, the slopes of the UC luminescence intensities i.e. the number of the photons involved in the excitation of the luminescence, decrease tending from $I_{lum} \propto I_{exc}^{\ n}$ to $I_{lum} \propto I_{exc}^{\ 1}$.

3.4.2. Up-conversion luminescence and phonons

In general, two competing processes in the multiphoton conversion can be disitinguished: radiative emission and non-radiative multiphonon relaxation. The radiative emission occurring from a higher excited state is the desired process, while multi-photon relaxation usually is not. In this section processes that lead to the multi-phonon relaxations will be reviewed.

In solid state physics vibrations of a crystal lattice are treated as quantized vibration modes or, in other words, – phonons. Depending on the lattice structure and the constituting ions, phonons of different energies appear. The phonon energy of the matrix is an important parameter, which defines the non-radiative decay rate. In [52] the probability of non-radiative transition W_{nr} between two levels E_2 and E_1 separated in energy by ΔE (**Fig. 3.12**) is defined by:

$$W_{nr} = C \cdot e^{-\alpha p}, \tag{3.8}$$

where C and α – are positive lattice-dependent constants, $p = \frac{\Delta E}{\hbar\omega}$ defines the number of phonons, required to bridge the ΔE by phonons with the energy $\hbar\omega$.

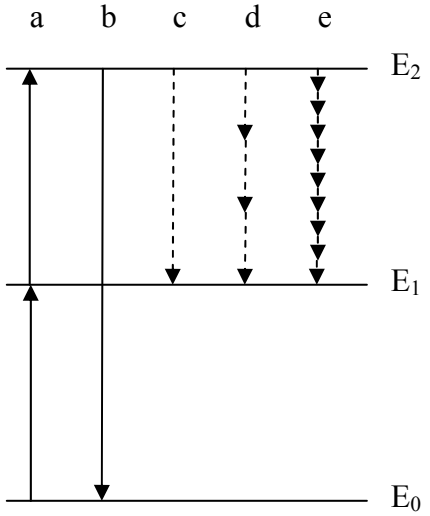

Fig. 3.12: Schematic energy level configuration. (a) – UC excitation, (b) – UC emission, (c) – non-radiative transition with one phonon emission, (d) – non-radiative transition with three phonons emission, (e) – non-radiative transition with nine phonons emission. Full and dashed arrows are radiative and non-radiative transitions, respectively.

From the analysis of (3.8) one can conclude, that the rate of the non-radiative transitions for a given ΔE will be higher in the matrix characterized by higher phonon energy. In other words, the probability of non-radiative transition between two energy levels separated by ΔE is lower if the number of phonons required to bridge the ΔE is smaller. As a rule-of-thumb the multi-phonon relaxation prevails over the radiative emission if less than 5 – 6 phonons are required to bridge the energetic separation between the emission and lower-lying level [52].

In **Fig. 3.13** the non-radiative decay rates for different hosts a function of ΔE are shown [10].

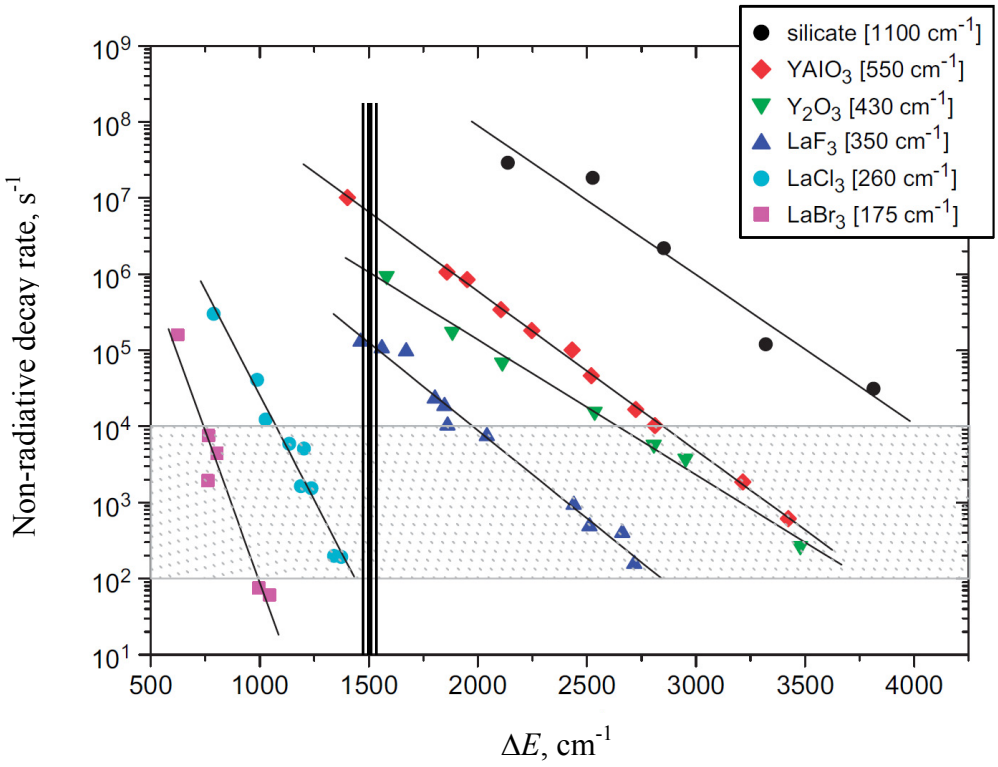

Fig. 3.13: Non-radiative rate vs. energetic separation ΔE in different hosts. Values in the square brackets are the corresponding phonon energies of the respective class of matrix [10]

The typical radiative rates of the luminescence of rare-earth ions (10^2 – 10^4) s^{-1} are indicated by a shaded area. In this region the radiative and non-radiative decay rates are comparable. The region above the shaded area corresponds to the enhanced multiphonon relaxation processes, when the luminescence of an ion in a specific

matrix is efficiently quenched by non-radiative decays via multiphonon relaxation. The region below the shaded area stands for the luminescence, which is almost not influenced by the multiphonon relaxations [10].

One can see that for a specific material the rate of the non-radiative decay grows when ΔE decreases. On the other hand the rate of the non-radiative decays for a specific ΔE for example at 1500 cm^{-1} (vertical line) decreases as the phonon energy of the matrix becomes smaller: silicates > oxides > fluorides > chlorides > bromides.

3.4.3. Dynamics of UC luminescence

The measurements of the UC luminescence excited in CW regime can provide general information about the process, for example, from the spectrum of the UC luminescence one can identify the ions, involved in the creation of the luminescence. However the direct measurements of the UC luminescence in CW regime fail to distinguish between the mechanisms (ESA or ETU) responsible for the luminescence. This information can be gained from time-resolved measurements of the UC luminescence under pulsed excitation. In this section the dynamical aspect of the UC luminescence for the two mechanisms (ESA and ETU) will be revealed [52].

In the case of ESA mechanism both GSA and ESA processes occur within the laser pulse, which is usually 5–10 ns short. As a result the luminescence kinetics will be a simple exponential decay, characterized by a transition probability k_{UC} or a lifetime τ of the respective excited state (**Fig. 3.14a**):

$$I_{UC}^{ESA} = I_0 e^{-k_{UC}t} = I_0 e^{-\frac{t}{\tau}} \tag{3.9}$$

In the case of ETU more complicated considerations have to be made. Let $N_1(t)$ and $N_2(t)$ be the electron populations of the intermediate (first) and the final excited (second) states, respectively. Under excitation three processes have to be taken into account: first de-excitation of the intermediate state to the ground state (rate constant k_{GR}), ETU from the intermediate state to the final excited state (rate constant k_{ETU}) and UC emission from the final excited state to the ground state (rate

constant k_{UC}). In this case the rate equations for the intermediate and the finale excited states can be written as:

$$\frac{\partial N_1(t)}{\partial t} = -k_{GR}N_1(t) - 2k_{ETU}\left[N_1(t)\right]^2 \tag{3.10}$$

$$\frac{\partial N_2(t)}{\partial t} = +k_{ETU}N_1(t) - k_{UC}N_2(t) \tag{3.11}$$

The factor 2 and the squared population of the first state appearing in the equation (3.10) are due to the fact that the both ions (initially in the intermediate state) after the ETU process leave the state to bring one of the ions into the final excited state and the other to the ground state.

Unfortunately, the system of the equations as it is cannot be solved analytically, however, at moderate excitation densities an assumption $2\left[N_1(t)\right]^2 \approx N_1(t)$ can be made and the system can be solved, giving the population of the intermediate excited state:

$$N_1(t) = C_1 e^{-(k_{GR}+k_{ETU})t} \tag{3.12}$$

and final excited state as:

$$N_2^{ETU}(t) = \left(\frac{1 - e^{[(k_{ETU}+k_{UC}-k_{GR})t]} C_2 k_{ETU}}{k_{GR} + k_{ETU} - k_{UC}} + C_3 \right) \cdot e^{(-k_{UC}t)} \tag{3.13}$$

The graphical interpretation of the equation (3.13) is shown in **Fig. 3.14b**. One can see that if the kinetics of the UC luminescence is governed by an ETU process, there is a zero intensity at the time moment $t = 0$. Afterwards a rise in the emission intensity followed by an exponential decay is present.

The clear difference between ESA and ETU seen in the temporal profiles of the UC luminescence allows for easy distinguishing between the two mechanisms. However, in practice real systems often show the combination of both ESA and ETU mechanisms (for example, the "green" UC luminescence of Er^{3+} ions can be observed in both ESA and ETU processes (**Fig. 3.5** and **Fig. 3.6**). The result of such possible combination is shown in **Fig. 3.14c**. At the time moment $t = 0$ there is an intensity offset responsible for the ESA mechanism, which starts within the laser pulse (shown as dashed line). The following growth and subsequent decay of the UC luminescence correspond to the ETU mechanism.

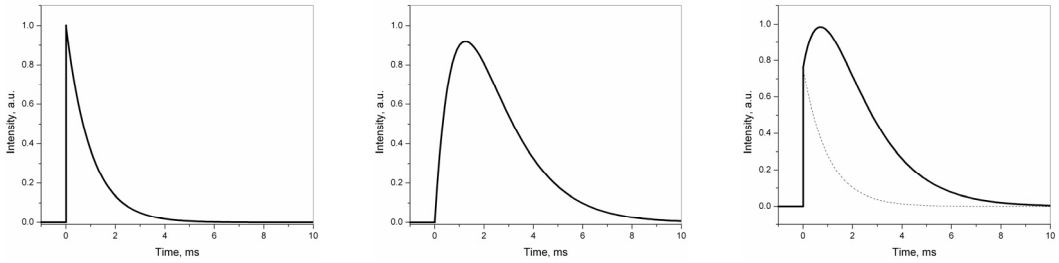

a b c

Fig. 3.14: Graphical interpretation of (a) ESA, (b) ETU and (c) combination of ESA and ETU mechanisms in the temporal profiles of UC luminescence.

3.5. Synthesis and up-conversion luminescence in rare-earth doped $NaLaF_4$

The first report on $NaLaF_4$ doped with Er^{3+} and Yb^{3+} has appeared in 1972 [26], however no further studies on the up-conversion luminescence in rare-earth doped $NaLaF_4$ have followed. Various works related to $NaF\text{-}LaF_3$ phase diagram [55-57] (**Fig. 3.15**), optical phonon modes in Raman polarized spectra of the bulk $NaLaF_4$ [30] and thermostimulated luminescence of different RE ions in polycrystalline $NaLaF_4$ [58] are virtually the only information known about the material.

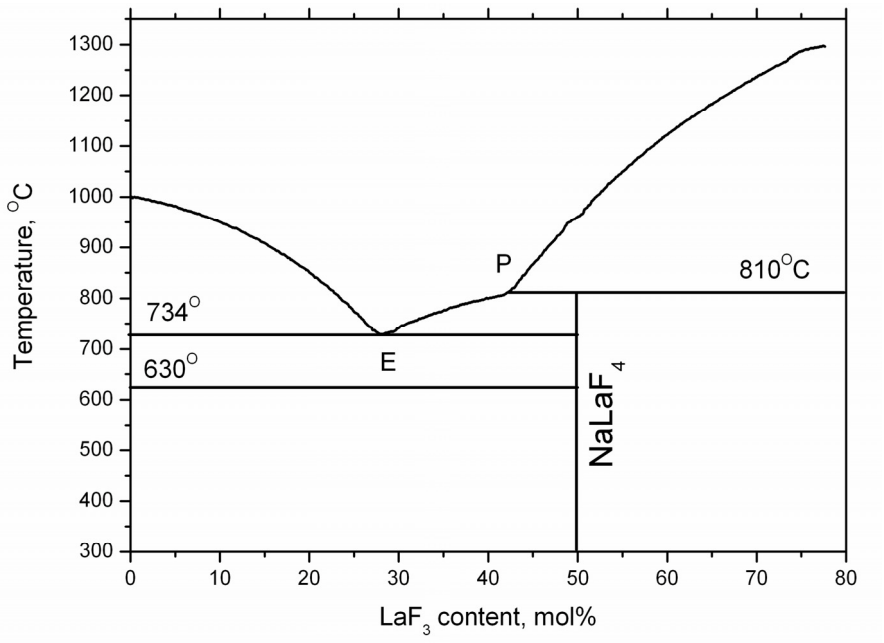

Fig. 3.15: Phase diagram of $NaF\text{-}LaF_3$ (adapted from [57]).

From x-ray diffraction measurements the lattice structure for most of $Na(RE)F_4$ is proposed to be hexagonal [57, 59]. Thoroughly the structure of $NaLaF_4$ was studied by the polarized Raman spectra measurements [30]. In this work it is claimed that the $C_{3h}(P\bar{6})$ *gagarinite* structure is the correct one for $NaLaF_4$ crystal. The authors describe $NaLaF_4$ as $Na_{1.5}La_{1.5}V_{Na}F_6$, where V_{Na} represents vacant Na sites, as presented in **Fig. 3.16**.

In this structure, La^{3+} occupy a 1*a* (Wyckoff) site, while a 1*f* site is shared by La^{3+} and Na^{+}; a 2*h* site is half occupied by Na^{+} (50% of occupancy by vacancies) and two nonequivalent fluorine ions, F1 and F2, occupy 3*j* and 3*k* sites [30].

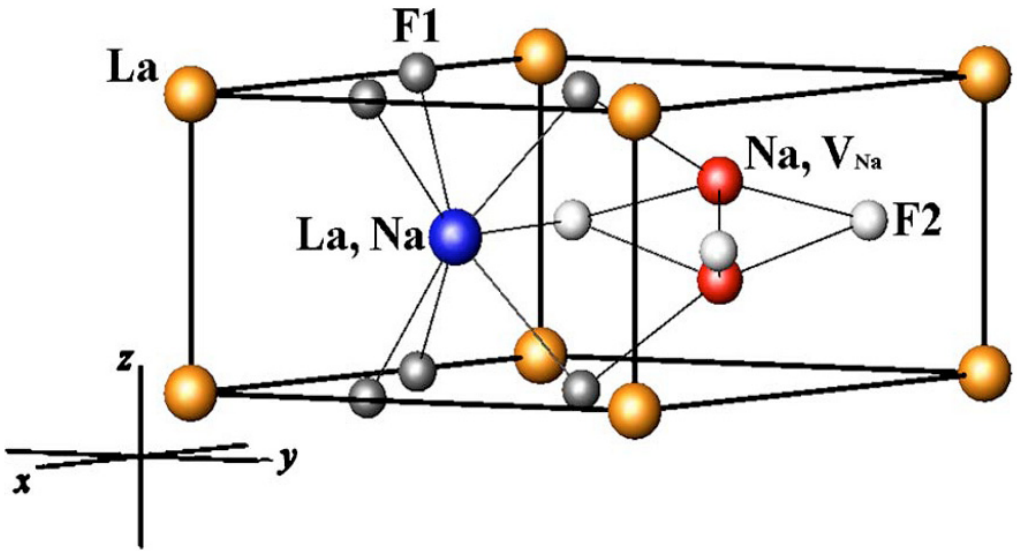

Fig. 3.16: The structure of $NaLaF_4$ represented as $Na_{1.5}La_{1.5}V_{Na}F_6$ crystal in the $P\bar{6}$ group [30].

The studies on RE doped $NaYF_4$, which has the same hexagonal structure as $NaLaF_4$, revealed that RE activators may occupy two or three non-equivalent sites in the crystalline structure, substituting for Y^{3+} and Na^{+}. The isostructure of $NaLaF_4$ to $NaYF_4$ supposes that the RE activators might substitute for La^{3+} and Na^{+}.

The conventional Czochralski technique has been reported for the synthesis of bulk undoped $NaLaF_4$ single crystals. From phase diagram (**Fig. 3.15**) it can be seen that $NaLaF_4$ has an incongruent melt point which means that $NaLaF_4$ can be grown directly only from non-stoichiometric melt, containing excess of NaF [30]. Due to

nonstoichiometric melt, only small single crystals sized as few cm^3 can be grown at very low pulling speeds (0.1 mm/h).

Two other synthesis methods of polycrystalline RE doped $NaLaF_4$ material have been reported [22, 58].

In [26] it was shown that the powder samples can be synthesized by firing the mixture of Na_2SiF_6 and $La_{1-x}RE_xF_3$. The latter was precipitated by hydrofluoric acid HF from an aqueous nitrate or chloride solution of the proper RE composition. During the synthesis at around 600^OC temperature Na_2SiF_6 decomposes to produce NaF and SiF_4 gas. The reaction between NaF and $La_{1-x}RE_xF_3$ yields $NaLa_{1-x}F_4:RE_x$. Up-conversion luminescence in Yb^{3+}, Er^{3+} doped $NaLaF_4$ synthesized by this method is mentioned in the same work [26], however no further studies of the up-conversion properties of RE doped $NaLaF_4$ have followed.

In [58] it was shown that RE doped $NaLaF_4$ can be prepared from La oxide and other RE oxides, considered to be used as dopants in the final material, Na_2CO_3 and aqueous 47% HBr and 40% HF solutions of acids. The mixture of the respective rare-earth oxides is dissolved in HBr and the fluorides REF_3 are precipitated with HF. The liquid is evaporated and HF is added again. The appropriate amount of Na_2CO_3 is dissolved in water and slowly added to the mixture. The product is dried, and the addition of HF and drying are repeated. Then the solid is transferred into a glassy carbon boat and heated to 550 °C in a HF/Ar gas stream for 20 h. In this step, the reaction toward hexagonal $NaLa_{1-x}F_4:RE_x$ takes place. The powder is ground up in mortar and heated to 590 °C in an Ar gas stream for another 20 h. Finally, the product is washed with water and then dried at 100 °C. The final product – $NaLaF_4$ doped with various RE ions – was thoroughly studied by Krumpel et al. [58] to obtain the energetic positions of RE dopant levels in the band gap of $NaLaF_4$ and no additional information on UC properties of the material have followed.

In the both synthesis methods highly hazardous hydrofluoric acid HF is used. The high corrosivity of the acid towards many materials including glass makes the synthesis of the $NaLaF_4$ rather complicated.

Both lack of the detailed information on up-conversion luminescence in RE doped $NaLaF_4$ and its complicated synthesis led to **the studies of the up-conversion processes in Er^{3+} doped $NaLaF_4$ and elaboration of new synthesis technique of Er^{3+} doped $NaLaF_4$ presented in this work.**

3.6. Synthesis and up-conversion luminescence in rare-earth doped oxyfluoride glass ceramics

Transparent low-phonon energy hosts are desirable media for up-conversion applications. Oxyfluoride glass ceramics, having rare-earth doped fluoride nanocrystals embedded in a silicate matrix, provides both the high efficiency of the up-conversion process (the efficient up-conversion luminescence occurs in the fluoride nanocrystals) and excellent chemical, mechanical and durability properties of the silicate glass [12].

Comparison of three main types of RE doped hosts is given in **Table 3.2**.

Table 3.2: Physicochemical properties of different hosts prospective in UC applications.

Crystalline phase *(Heavy fluorides)*	Oxide glass *(SiO_2 or GeO_2 base)*	Oxyfluoride glass ceramics *(SiO_2 with LaF_3)*
Complex synthesis	Easy synthesis	Easy synthesis
Costly	Cheap	Cheap
Hard to obtain large sized materials of good optical grade	Easy to obtain large sized materials of good optical grade	Easy to obtain large sized materials of good optical grade
NOT fusion-spliceable to conventional optical fiber	fusion-spliceable to conventional optical fiber	fusion-spliceable to conventional optical fiber
High efficiency of UC process	Low efficiency of UC process	High efficiency of UC process

After the first synthesis of the oxyfluoride glass ceramics by Wang and Ohwaki in 1993 [42] different oxyfluoride ceramics systems have been synthesized with PbF_2 [32], CaF_2 [36], BaF_2 [39], $BaYF_5$ [60], $NaYF_4$ [61] crystallites doped with various rare-earth dopants. In 1998, Dejneka [12] reported that LaF_3 is one of the most suitable fluoride hosts for rare earth ions in oxyfluoride glass ceramics because it has a great solid solubility for rare earth ions and is characterized by low phonon energy.

Table 3.3: Characteristic phonon energies of different hosts [12].

Type of the material	Highest phonon energy, cm^{-1}
Borate glass	1250
Silicate glass	1100
Heavy metal oxide	800
Fluorozirconate	580
Fluoroindate	520
Oxyfluoride glass ceramics with LaF_3	350

Among other glass families (**Table 3.3**) silicate glasses are the most often used ones. Although the phonon energy of the silicates is quite modest, the supreme physicochemical properties of the silicates are the reason of the enhanced attention towards this group of the materials.

A group of Wang have succeeded in the preparation of SiO_2 based glass ceramics with Er^{3+} doped LaF_3 nanocrystals. Various properties of this system related to the synthesis and up-conversion processes have been thoroughly studied [43-45]. According to their research for the synthesis of the oxyfluoride glass ceramics first of all an oxyfluoride glass with the composition 41.2 SiO_2 – 29.4 Al_2O_3 – 17.6 Na_2CO_3 – 11.8 LaF_3 – 1.0 ErF_3 has to be melted. The melting occurs in a covered Pt crucible at $1350^{O}C$. Afterwards the precursor glass is thermally treated at a glass crystallization temperature (for different RE concentrations the temperature varies from $650^{O}C$ to $690^{O}C$) to yield transparent glass ceramics. The structural composition (XRD and transmission electron microscopy measurements) of the glass ceramics revealed that the thermal treatment of the glass triggers the formation of hexagonal LaF_3 nanocrystallites sized about 15 – 25 nm. It was found that the increase of ErF_3 concentration in the precursor glass leads to the decrease of the crystallization temperature of LaF_3 suggesting that the Er^{3+} ions act as nucleating agents prompting the crystallization of the glass. According to the value of the activation energy of the crystallization it was argued that the appearance of LaF_3 is a diffusion controlled process.

During the thermal treatment Er^{3+} ions initially present in the glass phase partially incorporate into the LaF_3 nanocrystallites greatly improving the efficiency of the up-conversion luminescence. It was argued that considerably lower phonon

energy of LaF_3 crystalline phase (~350 cm^{-1} [12]) compared to the precursor silicate glass (~1100 cm^{-1} [12]) is responsible for the boost of the efficiency of the up-conversion luminescence observed in the glass ceramics.

Considerably less attention has been paid to the studies of the time-resolved UC luminescence in oxyfluoride glass ceramics containing LaF_3:Er^{3+} and no information on the UC luminescence and its temporal characteristics measured at low temperatures for this system could be found. The detailed studies of the up-conversion luminescence at low temperatures might be of great importance to understand the true nature of the up-conversion processes occurring in the material that are otherwise impossible to observe at higher temperatures due to, for example, thermal quenching.

A considerable dearth of the information on UC processes in Er^{3+} doped oxyfluoride glass ceramics at low temperature led to **the studies of the up-conversion processes at low temperatures in Er^{3+} doped oxyfluoride glass ceramics with LaF_3 nanocrystallites presented in this work.**

4. Experimental methods

4.1. Synthesis

For the synthesis of the samples in air atmosphere a temperature controlled high temperature furnace Carbolite HTF 18/8 was used (**Fig. 4.1**). The heating elements of the oven are $MoSi_2$, allowing to achieve temperature as high as $1800^{O}C$.

Fig. 4.1: High temperature furnace Carbolite HTF 18/8.

The annealing of $NaLaF_4$ in fluorine flow was performed in a special apparatus able to withstand fluorine atmosphere at elevated temperature. The scheme of the reactor is shown in **Fig. 4.2**.

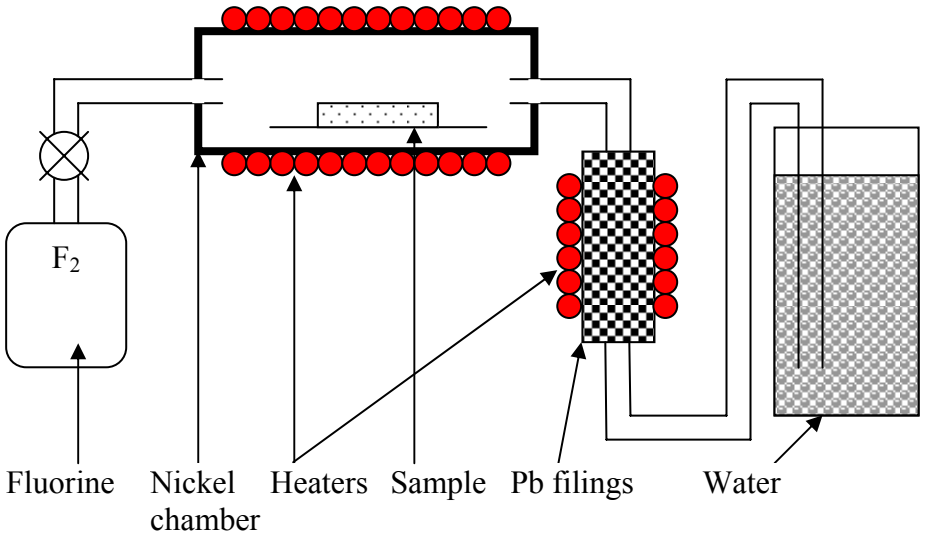

Fig. 4.2: Nickel reactor used for the fluorination of samples.

For the fluorination a mixture of 10% F_2 90% He was used. All the components of the reactor except for the heat exposed part are made from Teflon. The heat exposed part of the reactor is made from nickel – one of the rarest materials which is able to withstand the fluorine atmosphere at temperatures up to 600^{O}C. Unreacted fluorine gas is firstly passed through hot lead filings to form PbF_2, then bubbled through water before to be finally released into atmosphere.

4.2. Differential thermal analysis

DTA involves heating (or cooling) of a test sample and a reference sample under identical conditions and recording the temperature of the both samples. Later the differential temperature (difference between the temperature of the test sample and the reference sample) is plotted against temperature. Changes in the test sample, for example, melting, evaporation, crystallization or others, which lead to the absorption or evolution of heat, can be observed relative to the reference sample, provided that no changes in the reference sample during the heating occur.

Examples of some physicochemical processes are summarized in **Table 4.1**.

Table 4.1: Physicochemical processes involving absorption of the heat (endothermic) or evolution of the heat (exothermic) [62].

Process	Type of reaction
Glass transition	endothermic
Melting	endothermic
Crystallization	exothermic
Evaporation	endothermic
Sublimation	endothermic
Decomposition	exothermic
Oxidation	exothermic
Reduction	endothermic

In the present work the DTA was used to identify the crystallization temperature of the oxyfluoride silicate glass related to the appearance of LaF_3 crystalline phase in the glass matrix. The DTA measurements were performed using Shimadzu DTG-60 apparatus. The overall scheme of the apparatus is shown in **Fig. 4.3**.

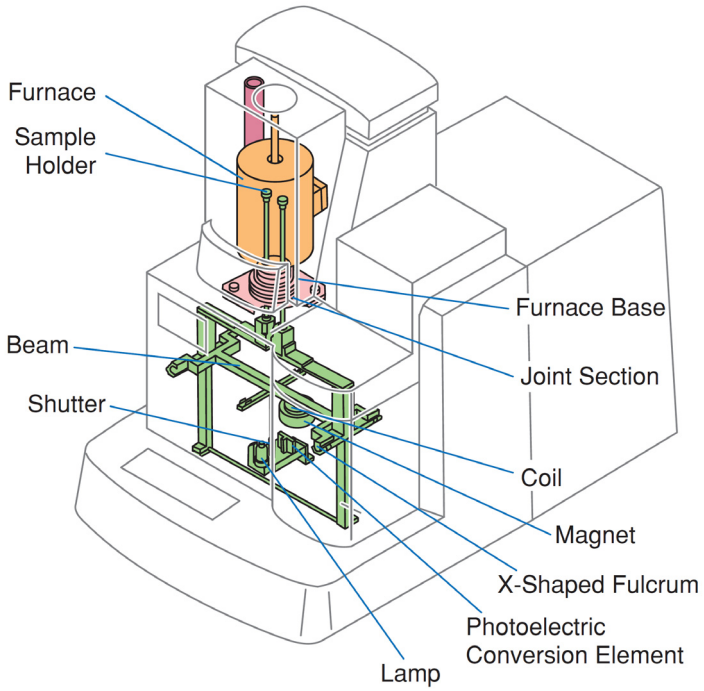

Fig. 4.3: Shimadzu DTG-60 apparatus scheme [63].

4.3. Structure investigations

For the determination of structure of the samples and for the estimation of the size of crystallites XRD method was used. In this method interference of x-ray radiation reflected from a material is measured. The condition of the constructive interference is given by the famous Bragg's relation:

$$2d \sin\theta = n\lambda \,, \tag{5.1}$$

where d is the distance between the atomic layers, θ – angle of incidence of x-rays, λ – wavelength of the x-ray radiation, n – the order of the diffraction (usually 1). This relation predicts that for certain structures series of XRD peaks at certain θ will appear. The XRD data of most of the inorganic materials is tabulated and can be used for the identification of unknown materials.

For the size determination the Sherrer's formula was used [64]:

$$d = \frac{K\lambda}{(\Delta - \Delta_{instr}) \cdot \cos(\theta)}, \tag{5.2}$$

where λ – wavelength of the x-ray radiation, Δ – FWHM of XRD peak appearing at the angle θ. K – the Sherrer constant (varies from 0.9 to 1.0 depending on the type of crystalline latiice), Δ_{instr} instrumental function. From the formula it can be seen that the size of the crystalline phase defines the broadness of the XRD peak: smaller size of the crystallites corresponds to broader XRD peaks.

For the measurements of XRD patterns x-ray diffractometer X'Pert Pro MPD was used. The diffractometer was equipped with an x-ray tube (anode material – Cu, wavelength 0.154056 nm) operating at 40 kV and 30 mA. The size determination was performed using the software provided with the diffractometer.

4.4. Infrared absorption and Raman spectra measurements

IR absorption spectra were measured using FTIR spectrometer Bruker Equinox 55. Resolution better than 0.5 cm^{-1}. Raman measurements were performed using SPEX-RAMALOG Laser Raman Spectrometer system (resolution 0.15 cm^{-1}) equipped with laser MLL-671 nm–300mW from CNI laser.

4.5. Luminescence measurements

UC and traditional luminescence in all the samples was excited either in CW regime by a temperature-power controlled IR laser diode system λ_{em}=975nm (power up to 1W) (Thorlabs: LDC 220C (power controller), TED 200C (temperature controller), TCLDM9 (diode mount), L975P1WY (laser diode)) or in pulsed regime by a wavelength tunable (optical parametric oscillator) pulsed laser NT342/3UV from Ekspla. Laser pulse duration was 5 ns, repetition frequency of the pulses – 10 Hz. The spectra have not been corrected for the spectral sensitivity of the equipment. For low temperature measurements ARSCRYO closed cycle He cryostat was used. Temperature of the sample was controlled by a temperature controller LakeShore 325 with a precision ±1 K.

4.5.1. Luminescence spectra

For the measurements of the luminescence spectra a CCD camera Andor DU-401-BV attached to Andor SR-303i-B monochromator/spectrometer was used. For power dependence measurements of the UC luminescence neutral density filters were used in the excitation channel to attenuate the excitation power while the intensity of the UC luminescence was detected by CCD camera. The excitation power was monitored by Thorlabs PDA55 amplified Si photodetector.

4.5.2. Excitation spectra

For the excitation spectra measurements NT342/3UV tunable laser, Andor SR-303i-B monochromator/spectrometer and Andor DU-401-BV CCD camera were used. The measurement technique involved the measurement of the luminescence spectra at different excitation wavelengths and processing of the measured data by author's developed software (LabVIEW) to yield the excitation spectra measured for a fixed luminescence position. The spectra have not been corrected for the spectral sensitivity of the equipment.

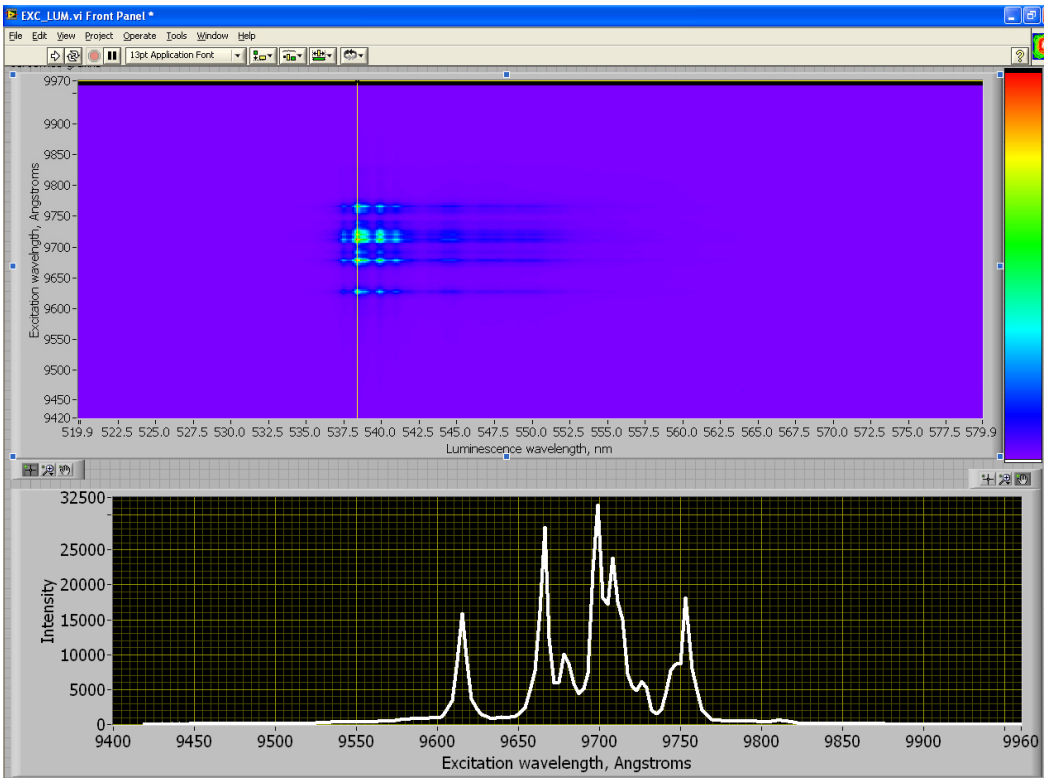

Fig. 4.4: Window of the software developed to analyze excitation spectra. Upper part – UC luminescence spectra measured at different excitation wavelengths, bottom part – excitation spectrum for the luminescence at 539 nm.

4.5.3. Luminescence kinetics

Luminescence kinetics was measured by a photomultiplier tube ФЭУ-115 attached to Andor SR-303i-B monochromator/spectrometer and detected by Tektronix TDS 684A oscilloscope. The overall temporal resolution of the system was less than 10 ns.

5. Results

5.1. Erbium doped $NaLaF_4$

5.1.1. Mixing-firing synthesis of $NaLaF_4:Er^{3+}$

Erbium doped polycrystalline $NaLaF_4$ samples were synthesized from 65NaF – 35LaF_3 – xErF_3 (x = 0.05, 0.1, 0.5, 1, 2, 4, 5, 7 and 10 mol %), 65NaF – 10LaF_3 – 25ErF_3 melt (in mol %). For additional luminescence measurements it was necessary to synthesize $NaErF_4$, for which 50NaF – 50 ErF_3 composition was used. For each batch about 5g of the fluoride components (purity 4N) were fully mixed and melted in a corundum crucible at $900^{O}C$ in air. After 1 hour the furnace was switched off and the batches were slowly cooled there for about 2 hours. The obtained polycrystalline materials were polished to form square coupons (5x5x2 mm) and later their structure and luminescence properties were studied.

5.1.2. Structure and optical properties of $NaLaF_4:Er^{3+}$

XRD pattern typical for the samples of $NaLaF_4$ at low Er^{3+} concentrations is shown in **Fig 5.1**.

The pattern is governed by the peaks related to $NaLaF_4$ crystalline phase (JCPDS No. 50-0155). Some peaks of weaker intensity related to NaF (JCPDS No. 36-1455) are also present in the pattern. Indeed according to the phase diagram [57] (shown in **Fig. 3.15**) if NaF-LaF_3 melt is cooled from $900^{O}C$ down to $734\ ^{O}C$ about 14 mol% of $NaLaF_4$ is crystallized with the respect to the initial melt composition.

Below the temperature of T = $734\ ^{O}C$, which corresponds to the eutectic temperature of the melt, additional amount of 56 mol% of $NaLaF_4$ is formed and about 30 mol% of NaF remains in the melt. So the final composition of the synthesized polycrystalline material is expected to be $NaLaF_4$ (70 mol %) and NaF (30 mol %).

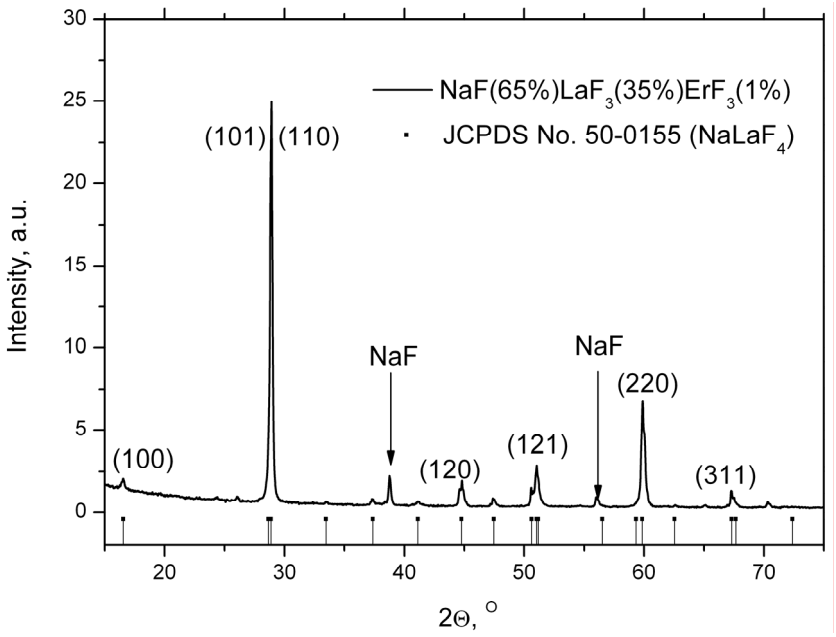

Fig. 5.1: XRD pattern of 1% Er^{3+} doped $NaLaF_4$ polycrystalline material. The most intense peaks of $NaLaF_4$ are indexed.

For better understanding of the possible variations in the phase composition at different ErF_3 content, a relevant part of the XRD pattern was selected and studied in detail (**Fig. 5.2**).

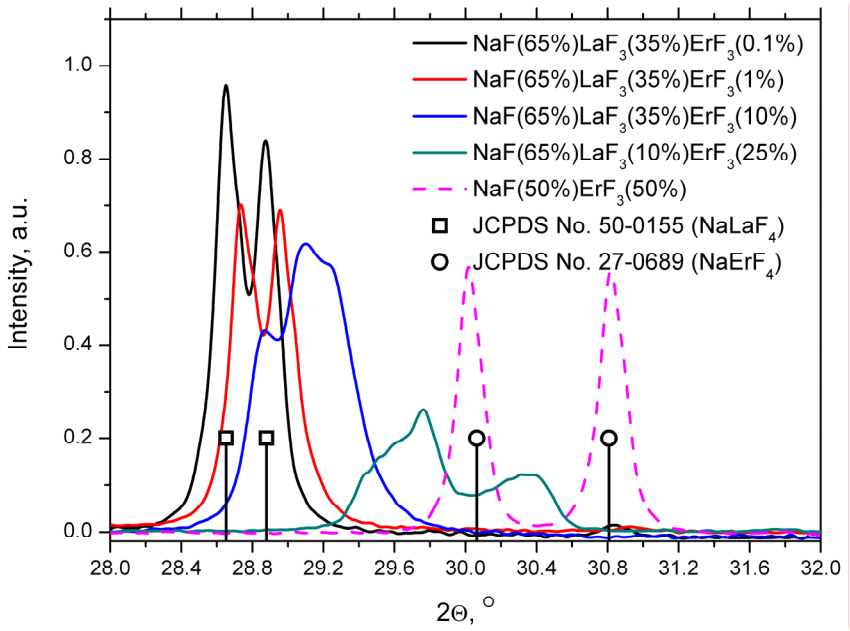

Fig. 5.2: XRD pattern of $NaLaF_4$:Er^{3+} material for samples with different LaF_3 and ErF_3 contents.

The positions of the peaks corresponding to $NaLaF_4$ crystalline phase are slightly shifted to higher degrees, when Er^{3+} content in the initial melt is raised. Further increase of ErF_3 concentration leads not only to the shift of the corresponding peaks to higher degrees but also to the appearance of a shoulder at the right side of the peaks. Moreover at even higher relative concentration of ErF_3 in the melt (NaF(65%) – LaF_3(25%) – ErF_3(10%)) the peaks corresponding to $NaLaF_4$ crystalline phase are broadened and shifted to even higher degrees. As for the samples where LaF_3 is absent (NaF(50%) – ErF_3(50%)) the observed peaks are identified as $NaErF_4$ (JCPDS No. 27-0689). The shift of the peaks observed at low concentrations of ErF_3 could be explained by the fact that the radius of Er^{3+} (1.06 Å) ion is smaller than that of La^{3+} (1.22 Å) ion [65], which means that the incorporation of activator ions in $NaLaF_4$ lattice would lead to the decrease of the lattice parameter of the latter, and the corresponding positions of XRD peaks would shift to higher degrees. This fact signifies that at low concentrations Er^{3+} ions mostly incorporate into $NaLaF_4$ crystalline phase and $NaLaF_4$:Er^{3+} is formed. The further shift and broadening of the peaks observed at higher concentrations of ErF_3 could be explained by the formation of $NaLaF_4$ crystallites with even higher concentration of Er^{3+} adjacent to much distorted $NaErF_4$ crystalline phase. It is possible because the crystalline structures of $NaLaF_4$ and $NaErF_4$ are identical and the lattice parameters are close ($NaLaF_4$ – (6.178 Å, 6.178 Å, 3.828 Å) (JCPDS No. 50-0155), $NaErF_4$ – (5.959 Å, 5.959 Å, 3.514 Å) (JCPDS No. 27-0689)). No changes in the position or shape of the peaks corresponding to NaF crystalline phase were noticed when Er^{3+} content in the melt was varied. This is an important fact because it suggests that NaF remaining in the material after melting is unlikely to be doped and its influence on the luminescent properties of the material is negligible. To sum up the information gained from the XRD analysis of the samples: at low concentrations of ErF_3 in the initial melt mostly $NaLaF_4$:Er^{3+} is formed, some residual NaF is also observed. At higher concentrations of ErF_3 in the initial melt not only the relative concentration of Er^{3+} in $NaLaF_4$ continues to increase but also strongly distorted $Na(LaEr)F_4$ compound tending towards $NaErF_4$ crystalline phase is formed.

The Raman spectrum measured for the undoped $NaLaF_4$ polycrystalline material is shown in **Fig. 5.3**.

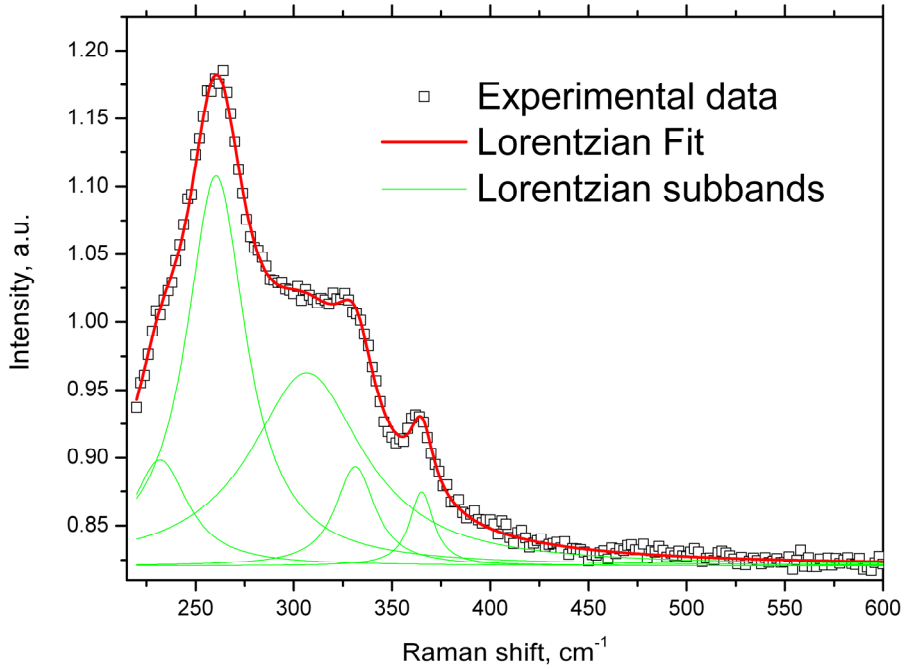

Fig. 5.3: Raman spectrum of undoped $NaLaF_4$ sample.

The Raman measurements for the doped specimens showed presence of the strong luminescence signal even at the lowest doping levels of Er^{3+} making the detection of the Raman signal impossible, therefore the undoped $NaLaF_4$ was chosen for Raman measurements. Lorentzian fit of the spectrum revealed five phonon bands centered at 232 cm^{-1}, 260 cm^{-1}, 306 cm^{-1}, 331 cm^{-1} and 365 cm^{-1}. These bands can be assigned to $NaLaF_4$ crystalline phase since NaF is not active in the Raman spectroscopy and cannot contribute to the spectrum. The positions of the bands are in a good accordance with previously reported polarized Raman spectrum for $NaLaF_4$ single crystal [30]. Taking into account the positions, FWHMs and the intensities of the corresponding Lorentzian sub-bands the effective phonon energy for $NaLaF_4$ could be estimated: $E_{ph} = \frac{\sum_i E_i w_i A_i}{\sum_i w_i A_i} \sim 290\ cm^{-1}$, where E_i, w_i and A_i are the position, FWHM and relative intensity of each Lorentzian sub-band respectively. The obtained value of the effective phonon energy, which to the utmost extent defines the rate of non-radiative transitions in a material, is even lower than that previously reported for $NaYF_4$ (360 cm^{-1}) [11] making $NaLaF_4$ a very promising candidate in the field of UC phosphors.

The UC luminescence spectrum for the sample with Er^{3+} concentration 2 mol% excited at λ=975 nm is shown in **Fig. 5.4**. The luminescence bands corresponding to the characteristic transitions in Er^{3+} ion are present in the UC luminescence spectrum: violet ($^2H_{9/2} \rightarrow {}^4I_{15/2}$), green ($^2H_{11/2} \rightarrow {}^4I_{15/2}$ and $^4S_{3/2} \rightarrow {}^4I_{15/2}$) and red ($^4F_{9/2} \rightarrow {}^4I_{15/2}$).

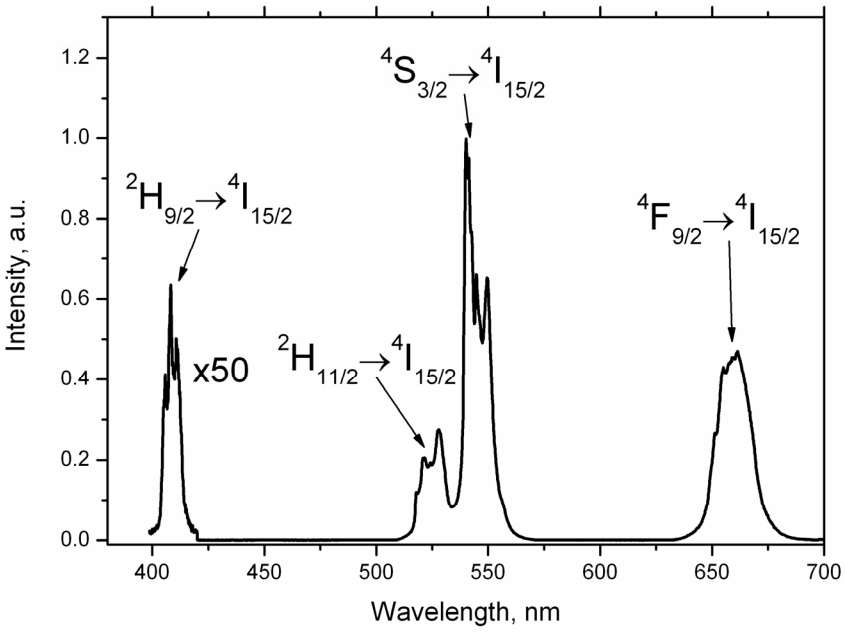

Fig. 5.4: Stationary UC luminescence spectrum of 2% Er^{3+} doped $NaLaF_4$ excited at 975 nm.

It is known that in UC processes the emission intensity I_{UC} has a power law dependence on the excitation power P_{exc}: $I_{UC} \sim (P_{exc})^n$, where n is a number of photons required to excite the emitting state [53]. In **Fig. 5.5** the dependence of the UC luminescence intensities measured for the main radiative transitions of Er^{3+} at 410 nm, 540 nm and 665 nm versus excitation power are shown.

The plots in the double logarithmic chart show linear behaviour of the UC luminescence intensity versus excitation power having parameters of the slopes close to 2 for the 540 nm and 665 nm bands. This is an indication that the $^4S_{3/2}$ and $^4F_{9/2}$ levels are populated by two photon processes, while the slope of 2.98 for the band at 410 nm signifies the involvement of three-photon absorption process in the creation of the violet UC band.

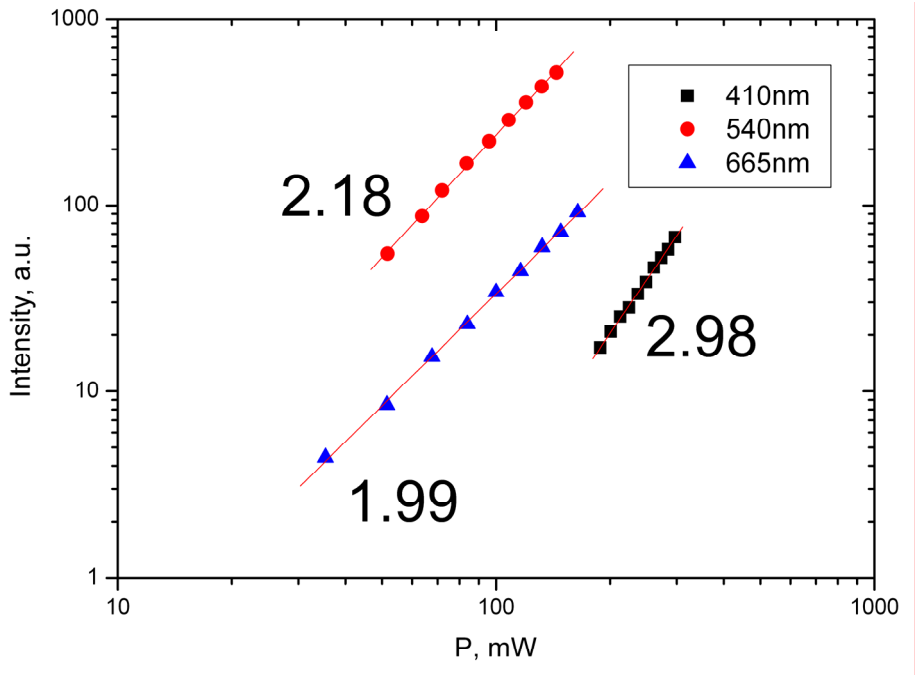

Fig. 5.5: Power dependence of the transitions $^2H_{9/2} \rightarrow {}^4I_{15/2}$ (squares), $^4S_{3/2} \rightarrow {}^4I_{15/2}$ (circles) and $F_{9/2} \rightarrow {}^4I_{15/2}$ (triangles) in $NaLaF_4:Er^{3+}$.

The time-resolved profiles of the UC luminescence for the green, red and violet luminescence bands are shown in **Fig. 5.6**. The rise and the decay components are present in all the kinetics, signifying the involvement of ET mechanism in the creation of all the three UC luminescence bands. The kinetics of the "green" luminescence is of more complicated nature – it has an intensity offset at the moment $t = 0$, while no intensity offset is present for the other transitions (**Fig. 5.6** insets). The possible excitation routes of the UC luminescence for Er^{3+} ion are shown in **Fig. 5.7**.

The appearance of the green luminescence band at 540 nm might be a result of an ESA_1 process i.e. sequential two photon absorption process: $^4I_{15/2} + h\nu \rightarrow {}^4I_{11/2} + h\nu \rightarrow {}^4F_{7/2}$. Afterwards the relaxation to $^2H_{11/2}$ and $^4S_{3/2}$ populates the emitting levels for the green luminescence. Another route to populate the $^4S_{3/2}$ level is by ET process: $(^4I_{11/2}, {}^4I_{11/2}) \rightarrow (^4I_{15/2}, {}^4F_{7/2})$ (ET_1). The involvement of the both ESA and ET processes is evident in the time-resolved luminescence decay plot for the green luminescence band excited at 980 nm (**Fig. 5.6a**). It can be seen that the luminescence decay curve has an intensity offset at $t = 0$, meaning that one of the mechanisms involved in the creation of the UC luminescence is ESA (the luminescence signal appears within the time of the laser pulse), while the rise part of the kinetics signifies the involvement of the ET process

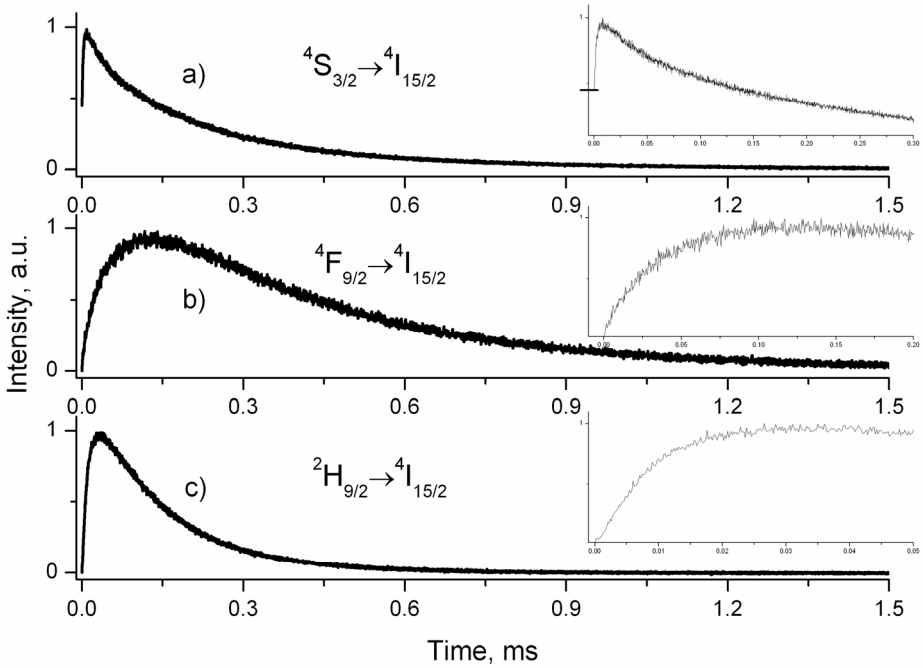

Fig. 5.6: Decay profiles for (a) $^4S_{3/2} \rightarrow {}^4I_{15/2}$, (b) $^4F_{9/2} \rightarrow {}^4I_{15/2}$, (c) $^2H_{9/2} \rightarrow {}^4I_{15/2}$ optical transitions in $NaLaF_4:Er^{3+}$(0.5mol%) excited at 980 nm.

The appearance of the red luminescence at 660 nm might be caused by a CR and subsequent ET process, for example, ($^4S_{3/2}$, $^4I_{15/2}$) → ($^4I_{9/2}$, $^4I_{13/2}$) (CR) and later ($^4I_{13/2}$, $^4I_{11/2}$) → ($^4I_{15/2}$, $^4F_{9/2}$) (ET_2). The clear evidence of a pure ET process is a time-resolved luminescence decay plot for the red band excited at 980 nm (**Fig. 5.6b**) – it can be seen that the luminescence signal does not have any intensity offset at $t = 0$.

The appearance of the violet band could be explained by a CR and subsequent ET process ($^4S_{3/2}$, $^4I_{15/2}$) → ($^4I_{9/2}$, $^4I_{13/2}$) (CR) and later ($^4S_{3/2}$, $^4I_{13/2}$) → ($^2H_{9/2}$, $^4I_{15/2}$) (ET_3). Again the ET process is supported by the luminescence decay kinetics excited at 980 nm (**Fig. 5.6c**) – no intensity offset is present at $t = 0$.

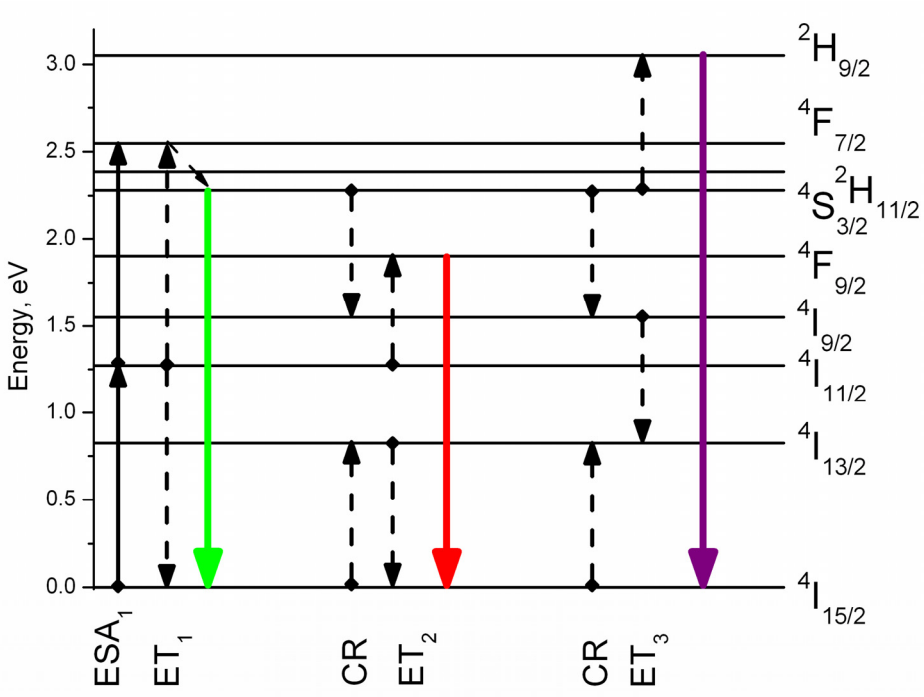

Fig. 5.7: Schematic energy level diagram and the main radiative transitions in Er^{3+} ion. Full and dashed arrows are radiative and non-radiative transitions, respectively.

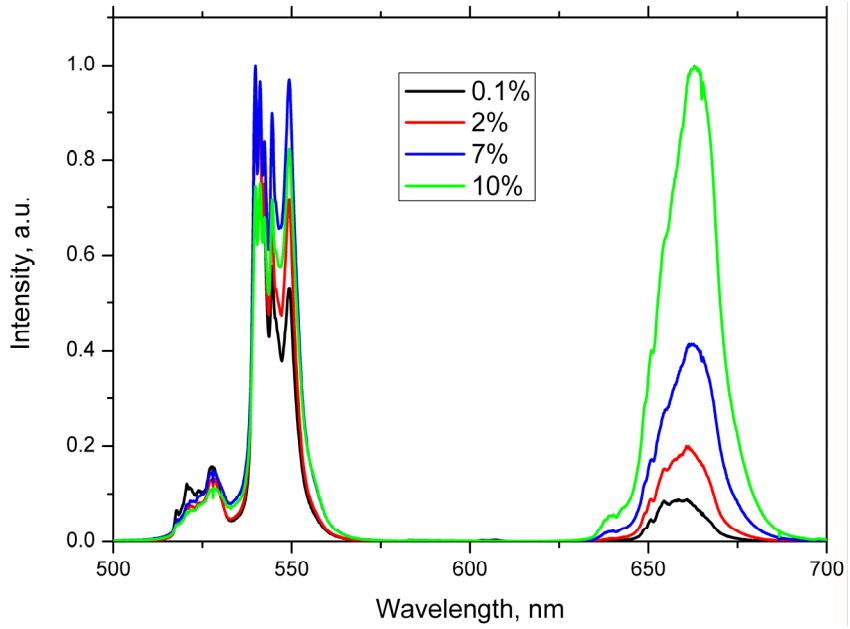

Fig. 5.8: Stationary UC luminescence spectra of Er^{3+} doped $NaLaF_4$ samples at different doping levels excited at 975 nm.

In **Fig. 5.8** the UC luminescence spectra for the samples at different doping levels are shown. It can be seen that the increase of Er^{3+} doping level leads to the decrease of the green-to-red bands intensity ratio. This could be explained by an

interionic cross-relaxation process, which becomes dominant at higher Er^{3+} concentrations, when the average distance between the Er^{3+} ions diminishes. On one hand the cross-relaxation process depopulates $^4S_{3/2}$ level ($^4S_{3/2}$, $^4I_{15/2}$) → ($^4I_{9/2}$, $^4I_{13/2}$) (in **Fig. 5.7** CR) thus decreasing the intensity of the green band. On the other hand it provides an extra route for $^4F_{9/2}$ level population: ($^4I_{13/2}$, $^4I_{11/2}$) → ($^4I_{15/2}$, $^4F_{9/2}$) (ET_2) increasing the population of $^4F_{9/2}$ level and the intensity of the red band.

Another important parameter, which is essential for the characterization of the optical properties of the material, is the decay profile of the luminescence under direct excitation of the emitting level. In this work we have performed time-resolved luminescence measurements for the green ($^4S_{3/2}$ → $^4I_{15/2}$) and red ($^4F_{9/2}$ → $^4I_{15/2}$) luminescence bands at direct excitation not higher than 300 cm^{-1} above the respective emitting level. The luminescence kinetics related to the transitions from the different Er^{3+} energy levels to the ground state are shown in **Fig. 5.9** and **Fig. 5.10**.

It can be seen in the semilogarithmic chart that the luminescence decay curves for the green band (**Fig. 5.9**) contain more than one component. Exponential fit (**Fig. 5.9** inset) shows that the experimental curve can be approximated by two exponents: “fast” and “slow”. At highest doping levels the slow component almost disappears and only the fast one remains. Similar tendency can be observed for the red luminescence band (**Fig. 5.10**), which also seems to be built of two components (**Fig. 5.10** inset), although the concentration impact on the lifetime value of the slow component is less pronounced compared to the green band.

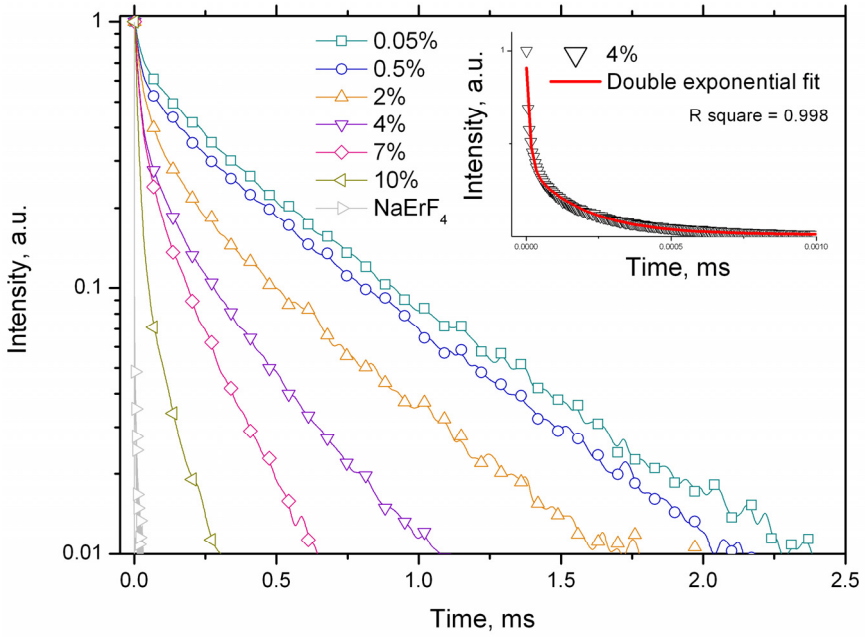

Fig. 5.9: Decay profiles for the $^4S_{3/2} \rightarrow {}^4I_{15/2}$ optical transition in $NaLaF_4$ at different Er^{3+} concentrations: direct excitation at room temperature. Inset – double exponential fit of the decay for the sample with 4 mol% Er^{3+}.

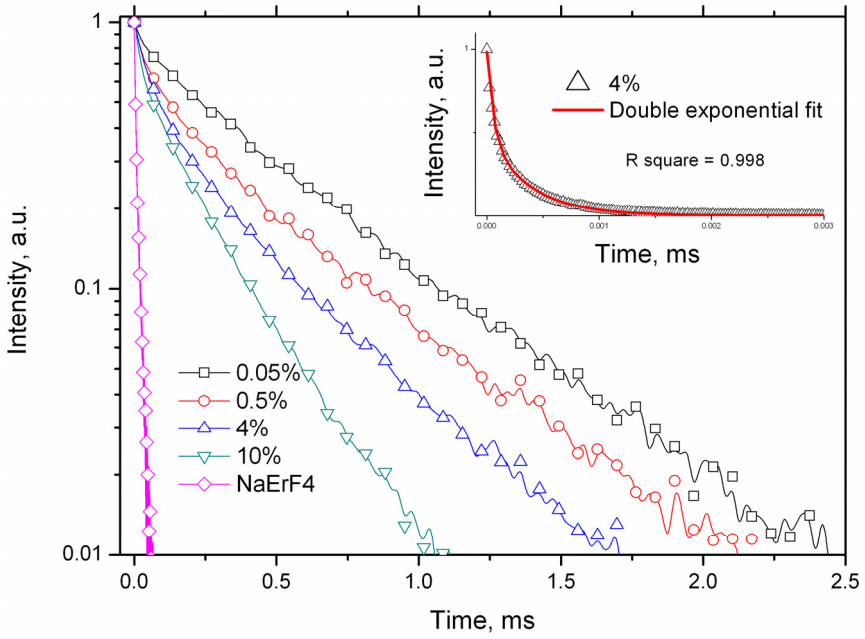

Fig. 5.10: Decay profiles for the $^4F_{9/2} \rightarrow {}^4I_{15/2}$ optical transition in $NaLaF_4$ at different Er^{3+} concentrations: direct excitation at room temperature. Inset – double exponential fit of the decay for the sample with 4 mol% Er^{3+}.

The values of the lifetimes for the both luminescence bands at different doping levels are summarized in **Table 5.1**.

Table 5.1: Lifetimes (in μs) of the main optical transitions in Er^{3+} doped $NaLaF_4$ samples at different doping levels and $NaErF_4$, measured under direct excitation at room temperature. The lifetimes of $NaYF_4:Er^{3+}$ 2 mol% is given for the comparison [11].

		0.05 %	0.1 %	0.5 %	1 %	2 %	4 %	10 %	$NaErF_4$	$NaYF_4$ 2% [11]
$^4S_{3/2}$ ↓ $^4I_{15/2}$	fast	50	40	35	30	25	20	7	0.275	360
	slow	510	490	470	410	350	240	80		
$^4F_{9/2}$ ↓	fast	110	100	90	85	70	60	30	5	430
	slow	530	520	510	480	450	390	230		

The presence of the fast and slow components in the luminescence decay plots at direct excitation could be explained by the formation of several crystalline phases in the polycrystalline material as it was seen in the XRD patterns (**Fig. 5.1** and **Fig. 5.2**). Since the decay profiles of the green luminescence at low Er^{3+} concentrations are mostly governed by a single slow exponent and XRD analysis reveals mainly the presence of $NaLaF_4:Er^{3+}$ in the samples, this slow exponential component could be attributed to $NaLaF_4:Er^{3+}$. It is also supported by the fact that the obtained lifetime value of the slow exponent is comparable to that of $NaYF_4$ (**Table 5.1**), which has similar structure and close effective phonon energy as $NaLaF_4$ does. At higher doping levels the value of the slow component for the green luminescence band in the exponential fit decreases. This might be due to the cross-relaxation processes between Er^{3+} ions in $NaLaF_4$, in which the emitting $^4S_{3/2}$ level is non-radiatively depopulated (cross-relaxation $(^4S_{3/2}, {}^4I_{15/2}) \rightarrow (^4I_{9/2}, {}^4I_{13/2})$).

The appearance of the fast component in the exponential decay of the green luminescence band and the growth of its relative intensity along with the increase of Er^{3+} concentration in $NaLaF_4$ correlates with the XRD observations (**Fig. 5.2**) where the increase of ErF_3 amount in the initial melt led to the shift of the corresponding XRD peaks towards those attributable to $NaErF_4$ crystalline phase. This fact suggests that the fast exponential component in the decay curve of the green luminescence band could be attributed to the distorted $NaErF_4$ crystalline phase.

5.1.3. Summary

1) Erbium doped polycrystalline $NaLaF_4$ material was synthesized.
2) The XRD patterns measured for $NaLaF_4$ material at different doping levels of ErF_3 showed considerable lattice distortion of $NaLaF_4$ when Er^{3+} content was increased.
3) The effective phonon energy of $NaLaF_4$ derived from Raman measurements for the undoped material was estimated $E_{ph} \sim 290\ cm^{-1}$.
4) The UC luminescence spectra measured for the samples at different doping levels of Er^{3+} revealed the characteristic luminescence bands in the violet ($^2H_{9/2} \rightarrow {}^4I_{15/2}$), green ($^2H_{11/2} \rightarrow {}^4I_{15/2}$ and $^4S_{3/2} \rightarrow {}^4I_{15/2}$) and red ($^4F_{9/2} \rightarrow {}^4I_{15/2}$) spectral regions.
5) The luminescence decay curves originating from $^4S_{3/2}$ and $^4F_{9/2}$ levels of Er^{3+} ions in $NaLaF_4$ crystalline structure were measured and the lifetimes of the corresponding levels were determined.
6) Pure ET mechanisms are responsible for the "red" and "violet" UC luminescence, while a combination of ESA and ET mechanisms is involved in the creation of the "green" UC luminescence.

The results are published in A. Sarakovskis, J. Grube, A. Mishnev, M. Springis, *Up-conversion processes in $NaLaF_4:Er^{3+}$*, Optical Materials **31**, 10 (2009), p. 1517 – 1524. {SCI, Impact factor 1.714}

In the previous section it was shown that RE doped $NaLaF_4$ is a prospective material in the field of UC luminophors due to the low phonon energy of the host matrix. However, the described synthesis procedure is costly (rare-earth fluorides are roughly 3 times more expensive then the respective oxides) and the synthesized material contains an unwanted $Na(LaEr)F_4$ crystalline phase even at lowest doping levels of Er^{3+}.

In some other synthesis techniques (described, for example, in [26, 58]) RE fluorides are prepared during the synthesis of $NaLaF_4$ by the reaction of RE oxides with hydrofluoric acid. In this case the synthesis procedure becomes complicated because of the high corrosivity and hazardous nature of the acid.

The next task was to develop a novel synthesis technique of $NaLaF_4:Er^{3+}$ improving the drawbacks of the previously mentioned and to study the structure and UC luminescence properties of the material at different stages of the synthesis.

5.1.4. Novel synthesis method

$NaLaF_4:Er^{3+}$ (Er^{3+} concentration 0.5 mol%) was prepared from La_2O_3, Er_2O_3 (purity 4N), NaF (purity 4N) and hydrochloric acid (37%). For the synthesis of the material the rare-earth oxides were dissolved in hydrochloric acid yielding $LaCl_3$ and $ErCl_3$:

$La_2O_3 + 6HCl \rightarrow 2LaCl_3 + 3H_2O$

$Er_2O_3 + 6HCl \rightarrow 2ErCl_3 + 3H_2O$

After evaporation of the liquid the chlorides were dissolved in deionized water while in separate beaker a water solution of sodium fluoride was prepared. The addition of the NaF solution to the dissolved chlorides led to the precipitation of LaF_3 and ErF_3:

$LaCl_3 + 3NaF \rightarrow LaF_3 + 3NaCl$

$ErCl_3 + 3NaF \rightarrow ErF_3 + 3NaCl$

The precipitate was washed several times with deionized water to remove NaCl species. Later, additional amount of NaF was added to the precipitate and the solution was evaporated to dryness.

5.1.5. Structure and optical properties of $NaLaF_4:Er^{3+}$

The XRD pattern of the resultant powder is shown in **Fig. 5.11**. One can see the peaks related to NaF and considerably broader bands identified as LaF_3 crystalline phase. According to the broadness of the peaks related to LaF_3 the average size of the crystallites was estimated by equation (5.2) as 10 nm.

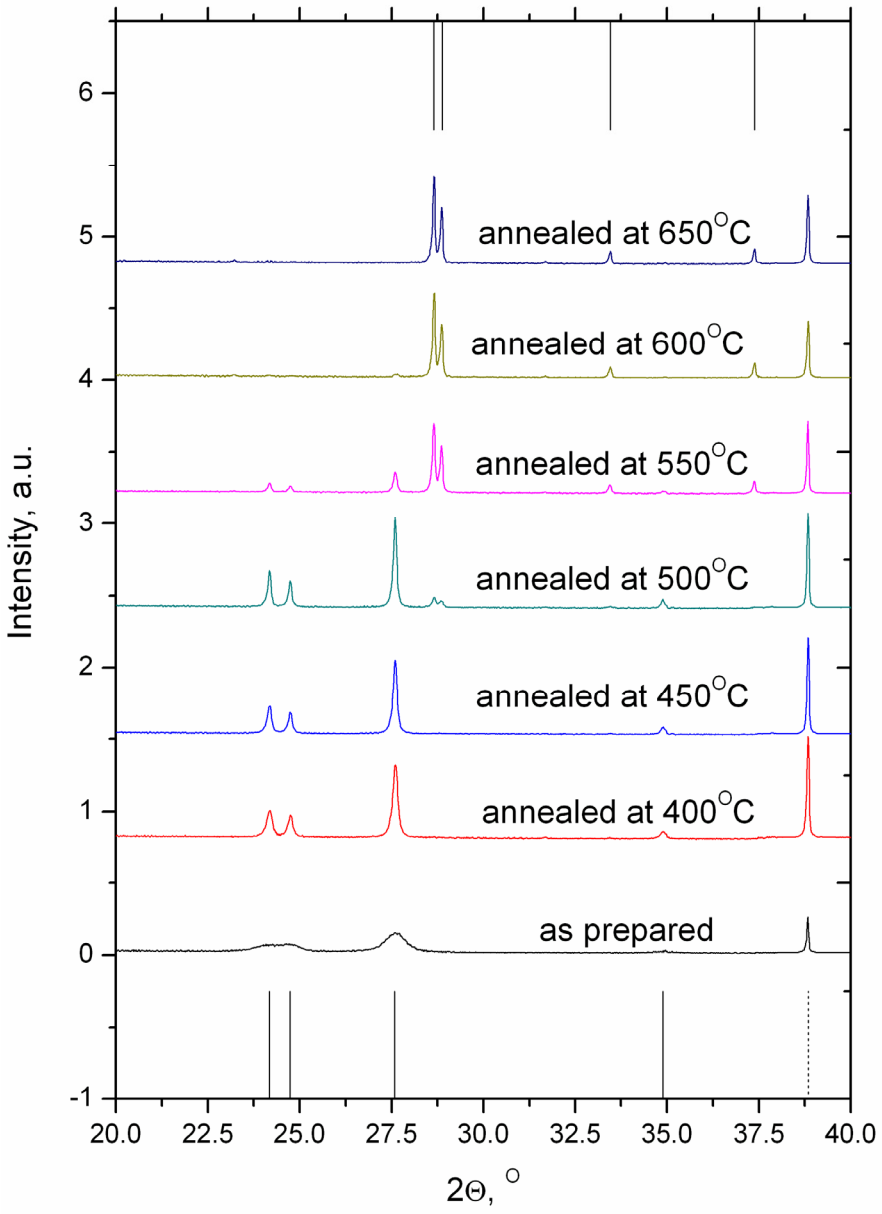

Fig. 5.11: XRD pattern of $NaLaF_4$ powder at different synthesis stages. Vertical lines – recognized XRD peaks of LaF_3 (solid lines at the bottom), $NaLaF_4$ (solid lines in the upper part) and NaF (dotted line at the bottom).

The following synthesis procedure involved heat treatment of the synthesized powders at different temperatures from 400^{O}C to 650^{O}C for 15h in air. Afterwards the powders were used for XRD measurements, while for optical measurements approximately 300 mg of each powder were pressed in tablets (Ø 13mm).

The XRD patterns of the synthesized samples are shown in **Fig. 5.11**. It can be seen that for the samples annealed at 400^{O}C and 450^{O}C the XRD peaks of LaF_3 get narrow indicating the increase of the size of LaF_3 crystallites. At higher synthesis temperatures the XRD peaks related to $NaLaF_4$ appear in the pattern while the intensity of the LaF_3 peaks decreases. For the samples heat treated at 650^{O}C the XRD pattern shows presence of $NaLaF_4$ and NaF but no LaF_3 can be observed (the evolution of LaF_3 and $NaLaF_4$ content in the materials annealed at different temperatures is shown in **Fig. 5.12**).

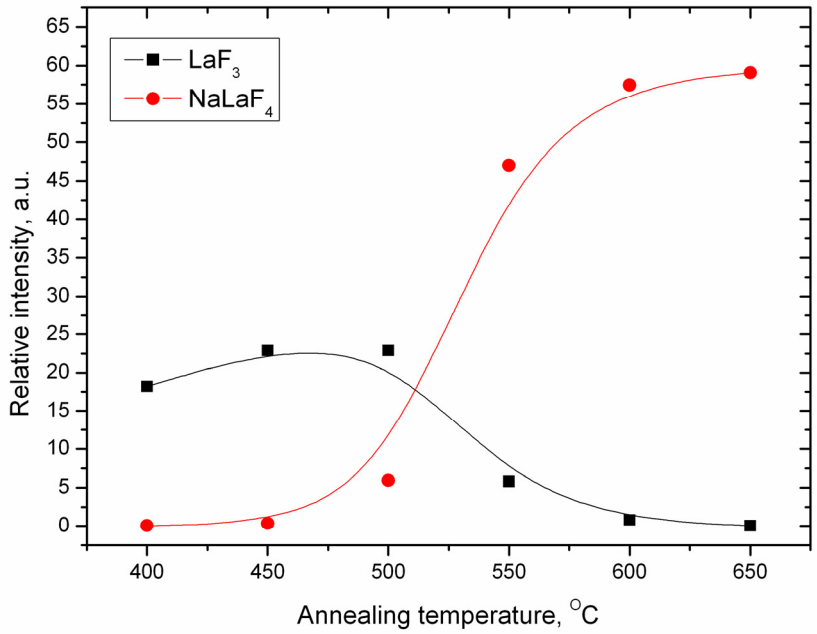

Fig. 5.12: Evolution of the intensity of XRD peaks related to LaF_3 (squares) and $NaLaF_4$ (circles) crystalline phases.

The spectrum of the UC luminescence under excitation at 975 nm measured for the sample synthesized at 650^{O}C is shown in **Fig. 5.13**. One can see the traditional luminescence bands of Er^{3+} in the green and red spectral region responsible for ($^2H_{11/2}$, $^4S_{3/2}$) → $^4I_{15/2}$ (green) and $F_{9/2}$ → $^4I_{15/2}$ (red) transitions. As it was shown in the previous section (**Fig. 5.7**) the excitation of Er^{3+} at 975 nm populates the $^4I_{11/2}$ level of

the ion. Afterwards the $^4F_{7/2}$ level becomes populated either by ESA ($^4I_{15/2}$ + hν → $^4I_{11/2}$ +hν → $^4F_{7/2}$) or by ET_1 (($^4I_{11/2}$, $^4I_{11/2}$) → ($^4I_{15/2}$, $^4F_{7/2}$)) mechanisms. The relaxation to $^2H_{11/2}$, $^4S_{3/2}$ populates the levels of the "green" luminescence while a combination of ($^4S_{3/2}$, $^4I_{15/2}$) → ($^4I_{9/2}$, $^4I_{13/2}$) (CR) and later ($^4I_{13/2}$, $^4I_{11/2}$) → ($^4I_{15/2}$, $^4F_{9/2}$) (ET_2) mechanisms might be responsible for the "red" luminescence.

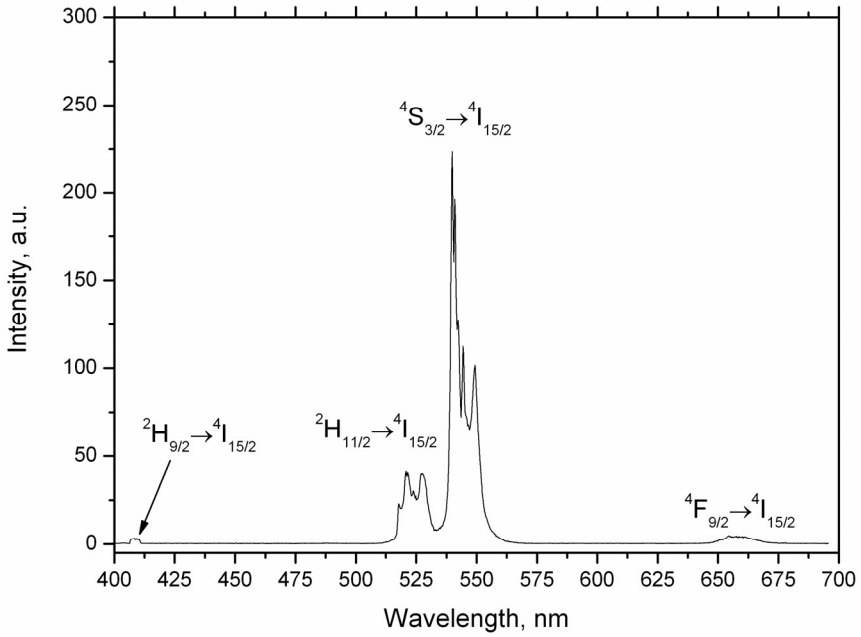

Fig. 5.13: UC luminescence excited at 975 nm measured for the sample annealed at 650^{O}C.

In further discussion the main attention will be focused on the "green" UC luminescence because the intensity of the corresponding ($^2H_{11/2}$, $^4S_{3/2}$) → $^4I_{15/2}$ transition is considerably higher than for the other transitions.

The "green" part of the UC luminescence spectrum was measured for the samples annealed at different temperatures (**Fig. 5.14**). Special care was taken when the sample tablets were placed in the sample holder to achieve equal measurement conditions for all the samples. It is essential if one wants to compare the relative intensities of the UC luminescence spectra for the samples annealed at different temperatures.

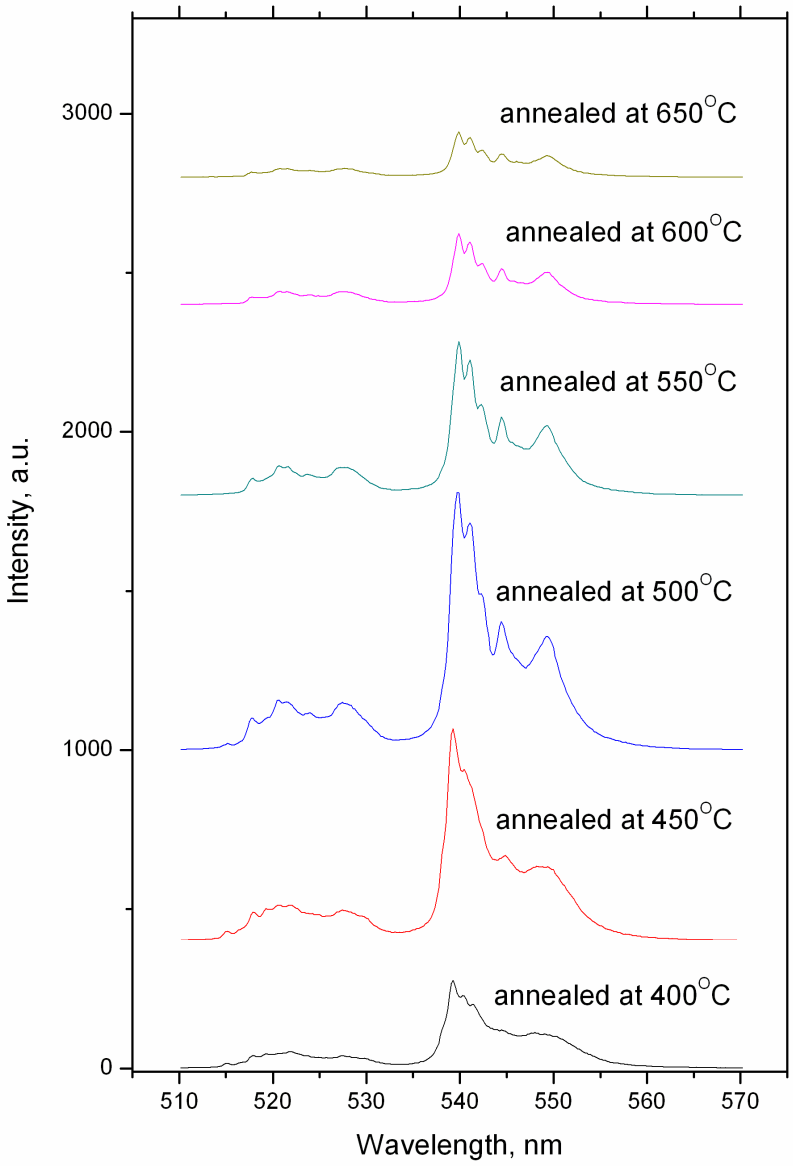

Fig. 5.14: "Green" UC luminescence excited at 975 nm measured for the samples annealed at different temperatures.

In **Fig. 5.14** one can see that both the intensity and the shape of the "green" luminescence band are different for the samples annealed at different temperatures. For example, the UC luminescence spectrum of the sample annealed at 400°C is similar to the one previously reported as $LaF_3:Er^{3+}$ [43]. The increase of the annealing temperature leads to the monotonous transformation of the shape of the "green" UC luminescence band tending towards $NaLaF_4:Er^{3+}$, seen in the previous section. The changes observed in the UC luminescence spectra agree well with the XRD measurements, where the increase of the annealing temperature led to the decrease of the amount of LaF_3 while the amount of $NaLaF_4$ increased.

The evolution of the intensity of the "green" UC luminescence band as the function of the annealing temperature is shown in **Fig. 5.15**.

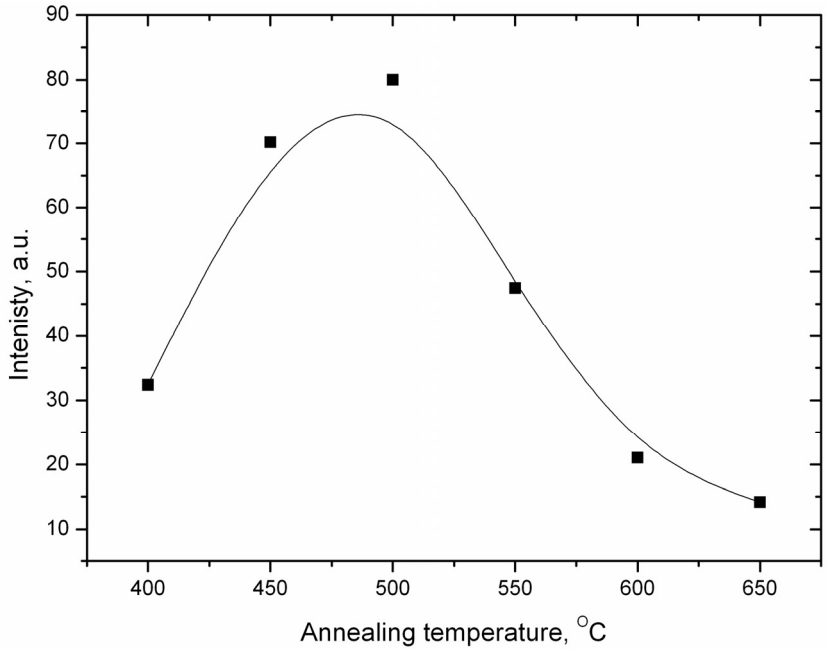

Fig. 5.15: Evolution of the intensity of the "green" UC luminescence band as the function of the annealing temperature.

From **Fig. 5.15** it can be seen that the intensity of the "green" UC luminescence has complicated dependence on the annealing temperature: up to 500^{O}C the intensity of the "green" luminescence rises when the annealing temperature is increased while at higher temperatures the intensity decreases again. Decay kinetics of the UC luminescence under pulsed excitation at 980 nm were measured to study the origin of the intensity dependence on the annealing temperature (**Fig. 5.16**).

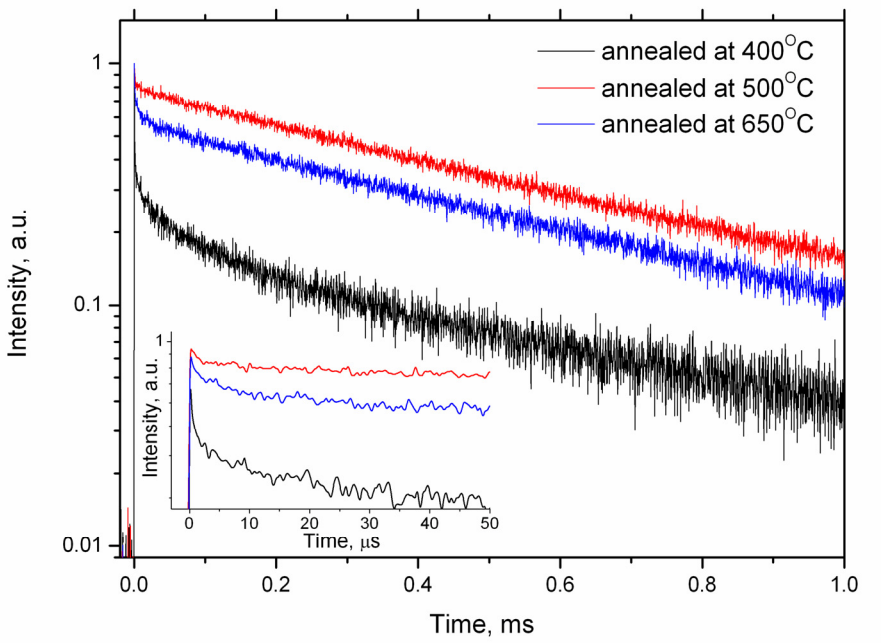

Fig. 5.16: Normalized decay kinetics of the UC luminescence excited at 980 nm. Luminescence position set to 542 nm. Inset: initial part of the decay kinetics magnified.

The measured decay kinetics show no intensity offset at the time t = 0. This indicates that the "green" UC luminescence is caused by the ESA process ($^4I_{15/2}$ + hν → $^4I_{11/2}$ +hν → $^4F_{7/2}$) (**Fig. 5.7**) and no ET is involved in the creation of the luminescence.

At the annealing temperatures up to 550°C the decay kinetics of the UC luminescence consists of three components. The third order exponential fit of the experimental data $I = A_1 e^{-\frac{t}{\tau_1}} + A_2 e^{-\frac{t}{\tau_2}} + A_3 e^{-\frac{t}{\tau_3}}$ reveals the values of the components: τ_1 = 630 μs, τ_2 = 70 μs and τ_3 = 100 ns. At the higher annealing temperatures the second decay component disappears and only the fast and slow components are present.

The relative intensities of the components (A_1, A_2 and A_3) vary as the annealing temperature changes and the evolution of the intensities of the three components as the function of the annealing temperature is shown in **Fig. 5.17**.

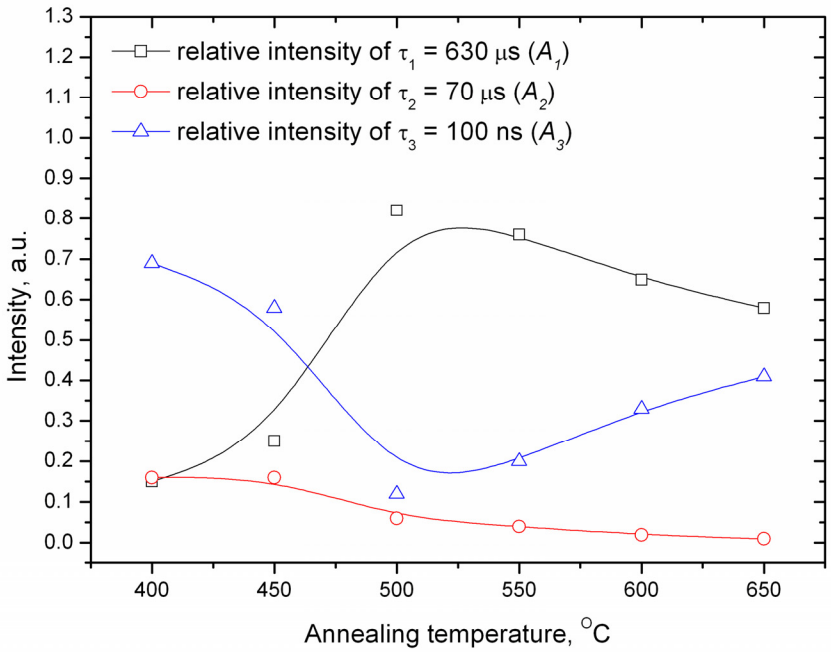

Fig. 5.17: Evolution of the relative intensities of the decay components as the function of the annealing temperature.

The analysis of the XRD patterns (**Fig. 5.11**, **Fig. 5.12**), UC luminescence spectra (**Fig. 5.14**) and the evolution of the decay components (**Fig. 5.17**) allows concluding that the slowest decay component (τ_1 = 630 μs) is attributable to the luminescence of $NaLaF_4:Er^{3+}$, because it has low relative intensity for the samples annealed up to 500°C (low content of $NaLaF_4$ crystalline phase), while at elevated annealing temperatures the slow decay component is prevailing.

The second decay component (τ_2 = 70 μs) can be attributed to the luminescence of $LaF_3:Er^{3+}$, because its dependence of the intensity on the annealing temperature is similar to the evolution of the XRD peaks related to the LaF_3 crystalline phase (**Fig. 5.12**) – as the annealing temperature grows both the content of LaF_3 and the intensity of the second decay component in the temporal profile of the UC luminescence gradually decrease.

The third decay component (τ_3 = 100 ns) can be explained by the quenching of the UC luminescence in $NaLaF_4:Er^{3+}$. In previous investigations performed on similar materials, for example, $NaGdF_4:Eu^{3+}$ [66] it was shown that oxygen as well as hydroxyl groups (OH^-) are efficient quenchers of the luminescence in fluorides. Since the initial stage of the synthesis of the samples occurs in water it is possible that hydroxyl groups appear in $NaLaF_4:Er^{3+}$ and influence its optical properties.

Absorption spectra in the IR region were measured for the samples annealed at different temperatures to clarify possible impact of OH^- on the optical properties of $NaLaF_4:Er^{3+}$ (**Fig. 5.18**).

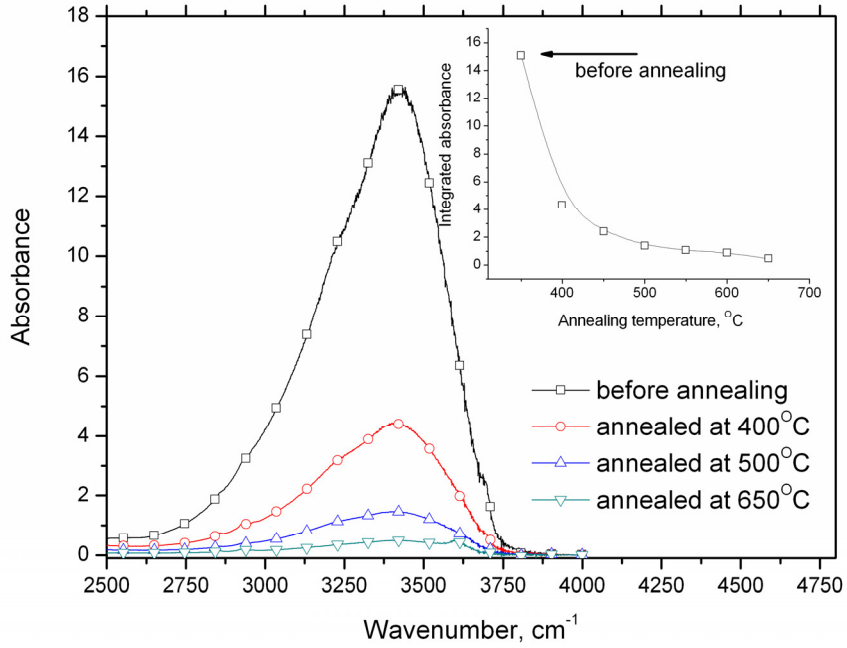

Fig. 5.18: Absorption spectra measured for the samples annealed at different temperatures. Inset: integrated absorbance for the samples annealed at different temperatures.

The absorption spectra reveal a band peaked at 3400 cm^{-1} which is ascribed to the stretching vibrations of $O\text{-}H^-$ [66]. The evolution of the intensity of the band is shown in the inset of **Fig. 5.18**. It can be seen that the intensity of the band at 3400 cm^{-1} decreases as the heating temperature rises, which indicates that the annealing helps to remove the OH^- species from the samples. The elimination of OH^- groups from the samples diminishes the quenching effect of the luminescence and the relative intensity of the fast component in the decay profiles decreases. The relative intensity of the slowest component "symmetrically" increases (**Fig. 5.17**) and the overall intensity of the UC luminescence grows. However, at higher annealing temperatures the OH^- content continues to decrease while the intensity of the fast component increases. This could be explained by the formation of complex oxygen related defects in $NaLaF_4$. It is possible because the annealing of the samples was performed in air and oxygen species present in the atmosphere can migrate inside $NaLaF_4:Er^{3+}$ and incorporate in the $NaLaF_4$ lattice [66], substituting, for example, for F^- [67]. In

this case Er^{3+}-oxygen conglomerates might form, considerably decreasing the efficiency of the luminescence due to increased multi-phonon relaxation rates [22, 66, 68] between the metastable states of Er^{3+} in $NaLaF_4$.

To clarify whether oxygen related defects are responsible for the quenching of the luminescence in the samples annealed at temperatures above 500^{O}C additional annealing in fluorine atmosphere (10% F_2, 90% He) was performed. The fluorination of the material at elevated temperatures is expected to eradicate oxygen impurities from the sample thus decreasing the quenching effect of the UC luminescence [22, 26, 69].

Decay kinetics of the UC luminescence measured for the samples annealed at 650^{O}C for 15 h in air atmosphere and later heat treated in fluorine atmosphere at 500^{O}C for 3h are shown in **Fig. 5.19**. It can be seen that the additional annealing of the sample in the fluorine atmosphere completely removes the fast component from the decay profile and only the slow component remains.

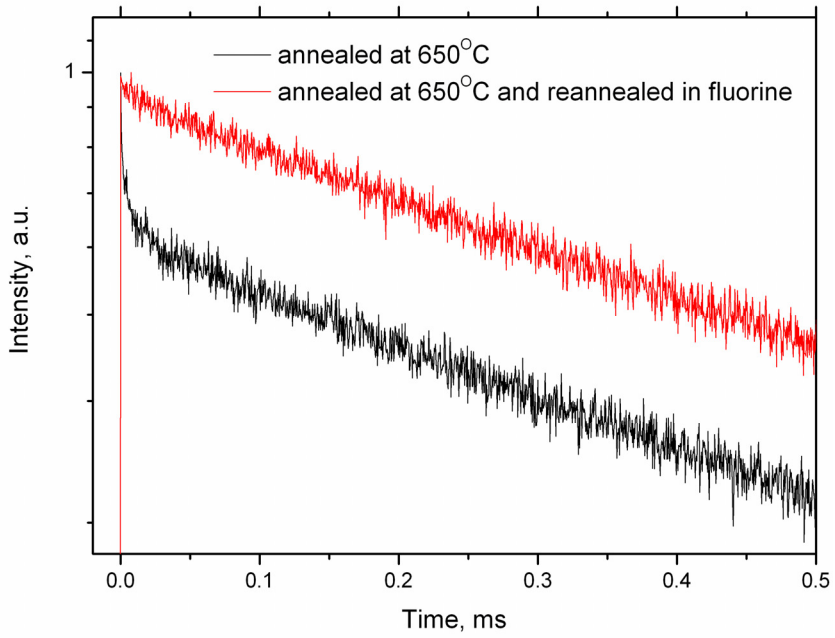

Fig. 5.19: Normalized decay kinetics of the UC luminescence excited at 980 nm measured for the samples reannealed in fluorine atmosphere. Luminescence position set to 542 nm.

The UC luminescence spectrum measured for the sample reannealed in the fluorine atmosphere (**Fig. 5.20**) shows approximately 8 fold increase in the intensity

compared to the sample before the fluorination and the highest intensity among other annealing temperatures.

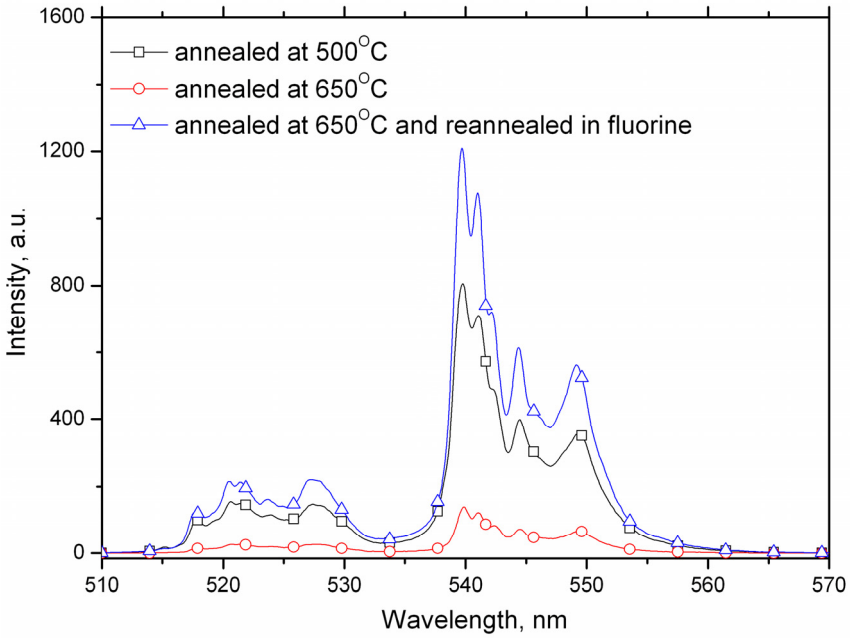

Fig. 5.20: "Green" UC luminescence excited at 975 nm measured for the sample annealed at different temperatures.

The observed differences in the temporal profiles measured for the samples before and after heat treatment in the fluorine atmosphere (the disappearance of the fast component from the decay kinetics of the UC luminescence) indicate that the fast decay component is related to the luminescence of Er^{3+}-oxygen defects which are formed during the first annealing in air.

The increased intensity of the UC luminescence after the reannealing in the fluorine atmosphere signifies that the quenching of the UC luminescence observed for the samples annealed above 550°C is due to Er^{3+}-oxygen related defects formed in $NaLaF_4:Er^{3+}$.

5.1.6. Summary

1) The novel synthesis procedure of $NaLaF_4:Er^{3+}$ without using hydrofluoric acid has been developed.
2) The XRD patterns measured for the material at rising annealing temperatures showed gradual content increase of $NaLaF_4$ and the decrease of LaF_3.
3) The optimal synthesis temperature of $NaLaF_4:Er^{3+}$ is $650^{O}C$.
4) The UC luminescence spectra measured for $NaLaF_4:Er^{3+}$ revealed the characteristic luminescence bands in the violet ($^2H_{9/2} \rightarrow {}^4I_{15/2}$), green ($^2H_{11/2} \rightarrow {}^4I_{15/2}$ and $^4S_{3/2} \rightarrow {}^4I_{15/2}$) and red ($^4F_{9/2} \rightarrow {}^4I_{15/2}$) spectral regions.
5) The kinetics of the "green" UC luminescence showed no rise component in the profile signifying that ESA mechanism is responsible for the appearance of the "green" UC luminescence band.
6) For the samples synthesized at the temperatures up to $500^{O}C$ the UC luminescence is quenched mostly by OH^- groups.
7) The concentration of OH^- groups present in the material at the first stage of the synthesis is decreasing as the annealing temperature grows.
8) The increase of the synthesis temperature above $500^{O}C$ promotes the creation of other oxygen related defects in the material, responsible for the quenching of the UC luminescence.
9) The post-treatment of $NaLaF_4:Er^{3+}$ in fluorine atmosphere at $500^{O}C$ helps to remove the oxygen impurities from the material thus increasing the efficiency of the UC luminescence.

5.2. Erbium doped oxyfluoride glass ceramics

5.2.1. Synthesis and structure of glass and glass ceramics

The attempts to synthesize the oxyfluoride glass and glass ceramics following precisely the method described by Wang (for example, [43]) have failed: neither DTA nor XRD showed appearance of any fluoride crystalline phase in the material up on heat treatment of the glass at the temperature corresponding to its crystallization.

Sequential iterative modifications of the chemical composition and synthesis method of the oxyfluoride glass yielded the following composition:

$40SiO_2–25Al_2O_3–19Na_2CO_3–3NaF–9LaF_3–0.5ErF_3$, which is somewhat different from those, reported in other works for similar oxyfluoride glass systems [13, 44, 53].

The glass was prepared from the high purity raw materials (purity 4N). The batch of the raw materials (~10g) was melted in a covered corundum crucible for 1 h at 1450 ^oC in air atmosphere followed by the casting of the liquid between two preheated stainless steel plates. Afterwards the glass was cut in approximately 2 mm thick plates.

DTA was performed on ground glass sample (approx ~ 50 mg) at 10 K/s heating rate. According to the DTA data the glass samples were annealed at 660^OC for 2 h yielding transparent glass ceramics. The structure of the glass (G) and glass ceramics (GC) samples was checked by XRD. All the spectral measurements were performed either at RT or at 50 K using closed cycle helium cryostat. Unfortunately, it was impossible to cool the samples to temperatures lower than 50 K due to the heat produced by the radiation of the excitation laser.

The DTA curve measured for the G sample is presented in **Fig. 5.21**. The endothermic region of the curve at 540^OC corresponds to the glass transition temperature while a pronounced exothermic peak observable at 660^OC is related to the crystallization of the glass. The XRD analysis confirmed the formation of LaF_3 crystalline phase after the heat treatment of the G sample at 660^OC, i.e. transparent GC is formed. The typical XRD patterns of the G and GC samples are presented in **Fig. 5.22**.

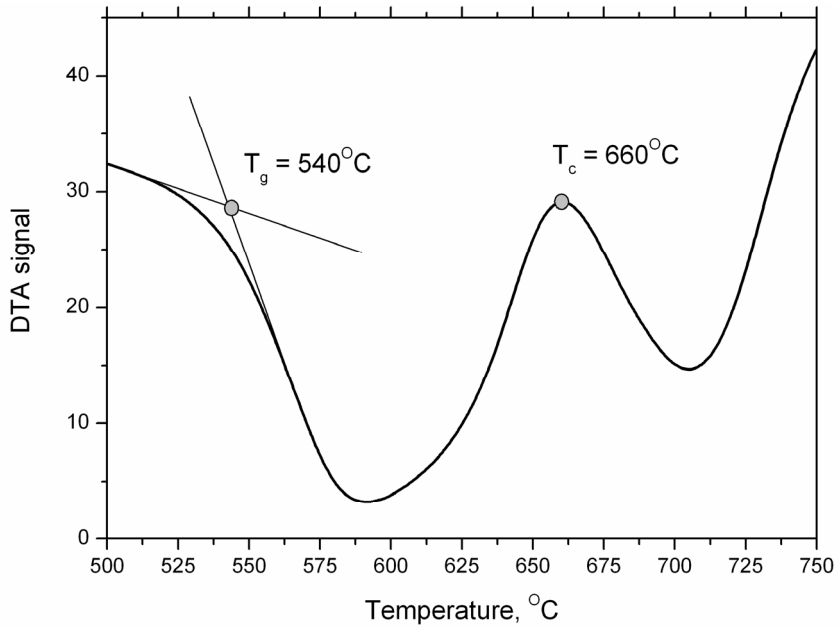

Fig. 5.21: DTA curve of the precursor glass. T_g – glass transition temperature, T_c – crystallization temperature.

The XRD pattern of the precursor glass sample does not show any sharp diffraction peaks having just two broad bands, indicating the amorphous structure of the G sample. The sharp diffraction peaks appearing in the XRD pattern of the GC sample are attributable to hexagonal LaF_3 phase (JCPDS 32-0483). Based on the widths of the XRD peaks and using equation (5.2) the mean crystallite size of LaF_3 was estimated to be around 20 nm.

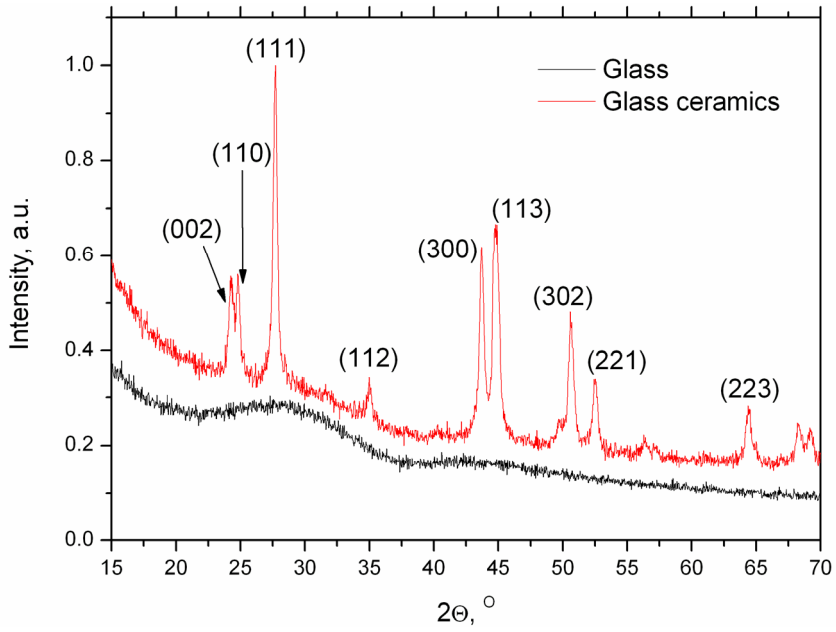

Fig. 5.22: XRD pattern of the G (black line) and GC (red line) samples. The most intense LaF_3 diffraction peaks are denoted.

5.2.2. Optical properties of glass and glass ceramics

The luminescence spectrum of the G and GC under pulsed excitation at 970 nm reveals traditional luminescence bands corresponding to Er^{3+} ion transitions in the green ($^2H_{11/2} \rightarrow {}^4I_{15/2}$, $^4S_{3/2} \rightarrow {}^4I_{15/2}$) and red ($^4F_{9/2} \rightarrow {}^4I_{15/2}$) spectral regions. In further discussion the attention will be focused on the "green" UC luminescence bands of Er^{3+} ($^2H_{11/2} \rightarrow {}^4I_{15/2}$ and $^4S_{3/2} \rightarrow {}^4I_{15/2}$). In previous discussion the main excitation mechanisms of the green UC luminescence of Er^{3+} ions have been determined. They involve the $^4I_{15/2} \rightarrow {}^4I_{11/2}$ transition followed by the $^4I_{11/2} \rightarrow {}^4F_{7/2}$ transition via ESA, ETU or the combination of the both.

The normalized UC luminescence spectra of the G and GC in the green spectral region measured at RT are shown in **Fig. 5.23a**. One can see that the spectrum of the G sample is built of two broad shapeless bands of different intensities corresponding to the different electronic transitions within Er^{3+}. The complicated composition of the bands is probably due to different non-equivalent positions of Er^{3+} in the glass network. The UC luminescence spectrum of the GC has some sharp overlapping peaks in its structure, suggesting the incorporation of Er^{3+} in the crystalline phase of LaF_3. The sharp peaks become even more pronounced when the UC luminescence of the GC is measured at 50 K (**Fig. 5.23b**) and the spectrum is slightly shifted to the "blue" compared to the one measured at RT. In the both spectra of the G and GC samples measured at low temperature the signal corresponding to the transition $^2H_{11/2} \rightarrow {}^4I_{15/2}$ is absent while that corresponding to the transition $^4S_{3/2} \rightarrow {}^4I_{15/2}$ increases in intensity several times. This can be explained by the fact that at RT the levels $^2H_{11/2}$ and $^4S_{3/2}$ of Er^{3+} are thermally coupled allowing the level $^2H_{11/2}$ to be thermally populated from $^4S_{3/2}$. At 50 K the thermal energy is not sufficient to realize the thermal excitation of the higher-lying $^2H_{11/2}$ level so only energetically the lowest of the two ($^4S_{3/2}$) remains populated [6].

Upon the ceraming, the overall intensity of the UC luminescence has increased about 10 times, which is due to the differences in the phonon energies of the two hosts: oxide glass and crystalline LaF_3. In previous sections it was shown that the efficiency of the UC luminescence observed in RE ions strongly depends on the phonon energy of the host, in which the active ion is situated. The small phonon

energy of the fluoride host compared to that of the silicate glass defines lower rate of non-radiative transitions within RE ion situated in LaF_3 thus increasing the efficiency of the UC luminescence.

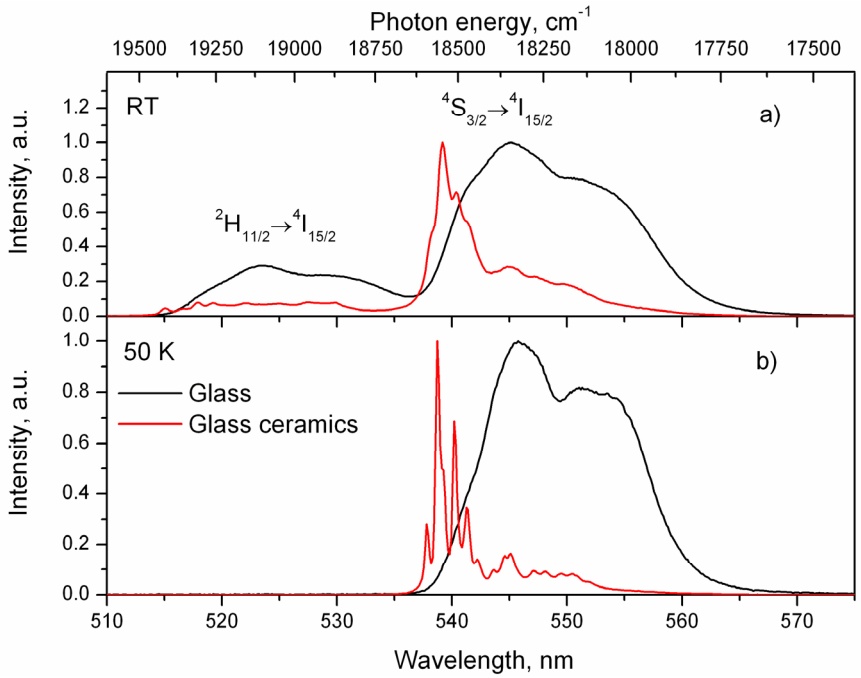

Fig. 5.23: UC luminescence spectra of the G (black line) and GC (red line) samples measured at a) RT and b) 50 K under 970 nm excitation.

The excitation spectra of the UC luminescence at 539 nm have been measured for the GC sample in the IR spectral region at RT and 50 K (**Fig. 5.24**).

Similarly to the luminescence spectra, the excitation spectra are changed when the temperature is lowered from RT to 50 K: the rather broad bands present at RT become sharper and shift to the "blue" when the temperature is lowered. Taking precise data of the Stark sublevels gained from the absorption spectra of $LaF_3:Er^{3+}$ [49] measured at 4.2 K, the electronic transitions from different Stark sublevels of the ground state $^4I_{15/2}$ (numerical values of the first five Stark sublevels of the ground state are given in the legend of **Fig. 5.24**) to different Stark sublevels of the $^4I_{11/2}$ state could be deduced from the excitation spectra (vertical bars under the plots in **Fig. 5.24**).

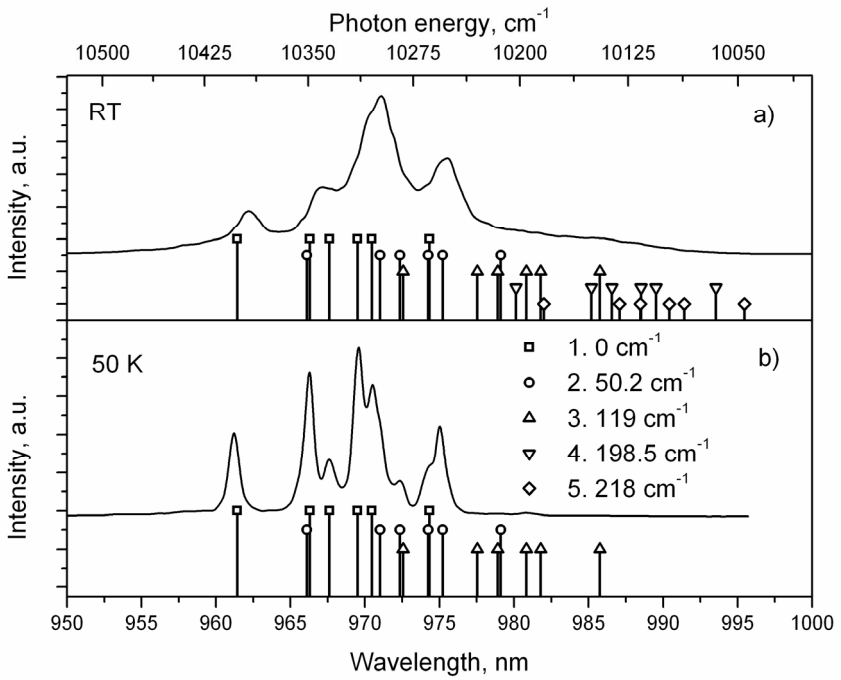

Fig. 5.24: Excitation spectra of the UC luminescence at 539 nm measured for the GC sample at a) RT and b) 50 K. Vertical bars under the plots correspond to the transitions from different Stark sublevels of the ground state $^4I_{15/2}$ (energetic positions of the sublevels are given in the legend) to the Stark sublevels of the $^4I_{11/2}$.

At RT the electronic transitions from at least first five Stark sublevels of the ground state to $^4I_{11/2}$ level could be excited under appropriate IR illumination while at 50 K the transitions from only the first three Stark sublevels of the ground state to different sublevels of the $^4I_{11/2}$ are active (**Fig. 5.28**). Indeed according to Boltzmann distribution the population of the third Stark sublevel of the ground state due to the thermal excitation at 50 K could reach few percents allowing the electronic transitions arising from this sublevel to $^4I_{11/2}$ while at RT first five Stark sublevels of the ground state are thermalized. According to Boltzmann distribution all the Stark sublevels of the $^4I_{11/2}$ level are thermalized meaning that at both 50 K and RT the electronic transitions arising from any of the Stark sublevels of the $^4I_{11/2}$ level can occur.

The excitation spectra of the "green" luminescence have been measured also at the direct excitation of the $^4F_{7/2}$ level (**Fig. 5.25**) in the spectral region 470 nm – 500 nm at 50 K and RT. The excitation spectrum measured at 50 K is built of sharp lines corresponding to the transitions from the different Stark sublevels of the $^4I_{15/2}$ to the different Stark sublevels of the $^4F_{7/2}$ level. The spectrum measured at RT appears

broadened: it contains less resolved spectral lines, which superimpose a broad excitation band.

The differences between the excitation spectra measured at different temperatures for the both UC luminescence and conventional luminescence provide the information which is important if one wants to consider the realization of either ESA or ET mechanisms of the UC process and they will be discussed later.

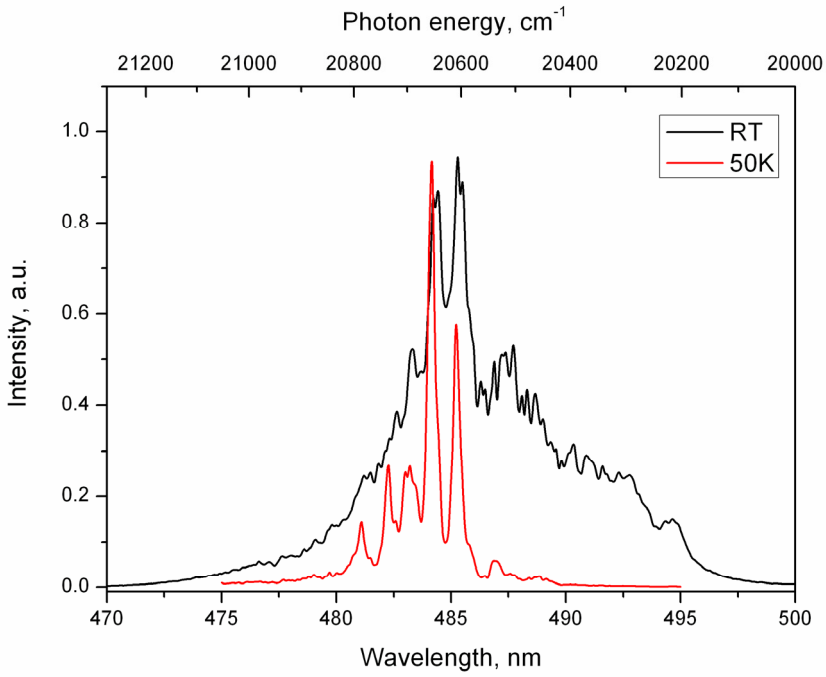

Fig. 5.25: Excitation spectra of the luminescence at 539 nm measured for the GC sample at RT (black line) and 50 K (red line).

The decay curves of the green UC luminescence at 539 nm have been measured for the GC sample under different excitation wavelengths in the IR at RT and at 50 K. The temporal profiles of the luminescence excited at different wavelength in the region 950 nm – 1000 nm measured at RT appear to be very similar, having two distinct decay components: fast and slow (as an example one of the decay kinetics excited at 970 nm is shown in **Fig. 5.26**). The slow component (~500 μs) is related to the luminescence originating from the crystalline phase, because this component is absent in the decay profiles of the G sample (shown in **Fig. 5.26** for the comparison). The fast component (~2 μs) coinciding with the one measured for the G sample is attributable to the UC luminescence of Er^{3+} occurring in the glassy phase of the GC.

For the both decay components no notable growth of the luminescence signal after the laser pulse in the spectral region of the excitation (950 nm – 1000 nm) was noticed suggesting that mostly ESA mechanism of the UC luminescence is dominant in the GC.

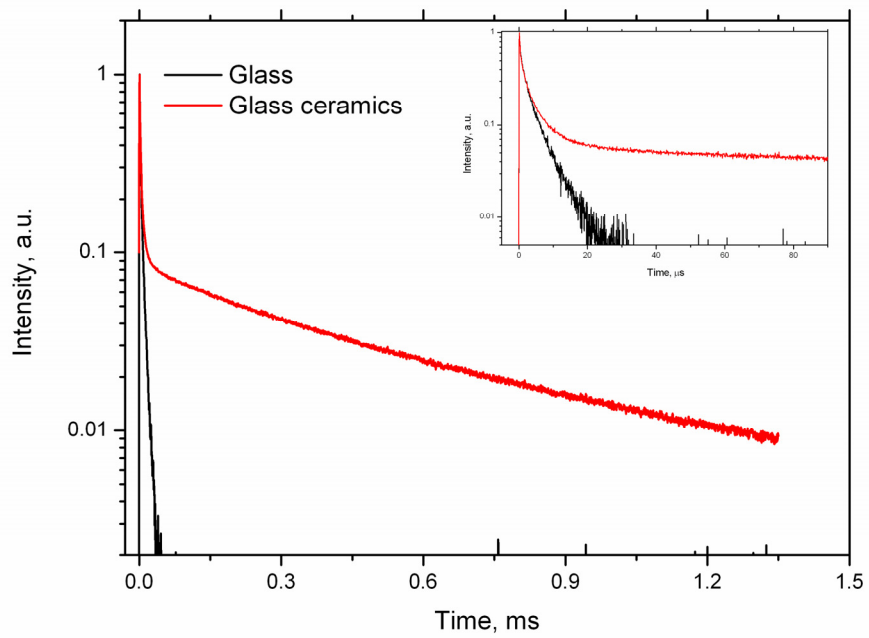

Fig. 5.26. Decay kinetics of the UC luminescence for the G (black line) and GC (red line) samples under 970 nm excitation measured at RT. Inset: magnified initial part of the decay kinetics. Luminescence position set to 539 nm.

The fast and the slow components are also present in the decay profiles of the UC luminescence when measured for the GC at 50 K although the characteristic lifetime values of the components increase, reaching ~3 μs and ~1.5 ms for the fast and slow components respectively (**Fig. 5.27**). The shape of the slow component varies when the excitation wavelength is changed: only at a few excitation wavelengths the decay kinetics reaches its maximum of intensity within the time of the laser pulse while at most cases the kinetics possesses an explicit rising part of the slow component. The appearance of the rising part suggests an ET mechanism of the UC luminescence to be dominant at low temperatures in the crystalline phase.

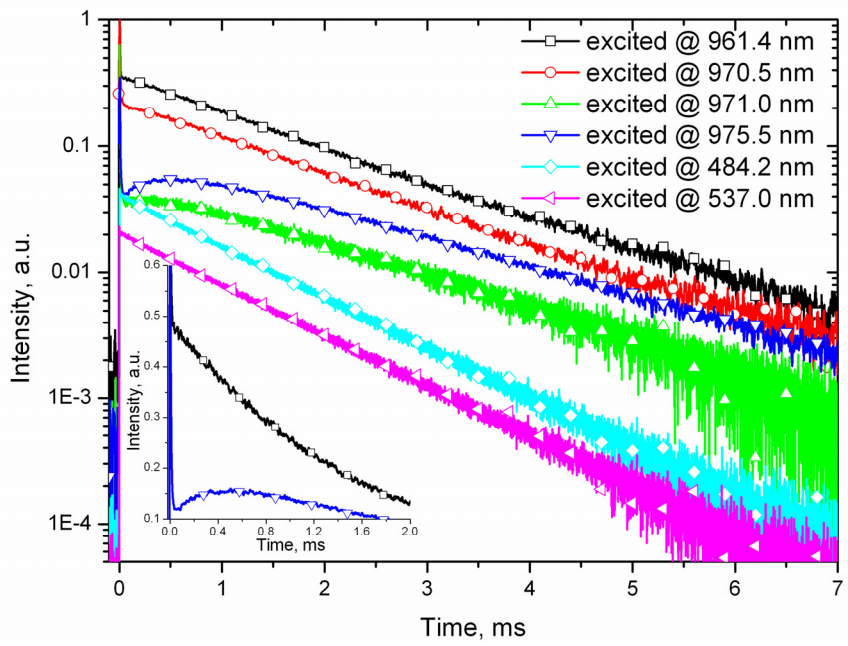

Fig. 5.27: Decay kinetics of the UC and traditional luminescence for the GC sample under various excitation wavelengths measured at 50 K. Inset: magnified initial part of the decay kinetics. Luminescence position set to 539 nm.

To study the origin of the ESA and ET mechanisms in the crystalline phase of the GC at low temperature the energy level scheme adapted from [49] with the Stark sublevels of the ground and the excited states has been constructed (**Fig. 5.28**).

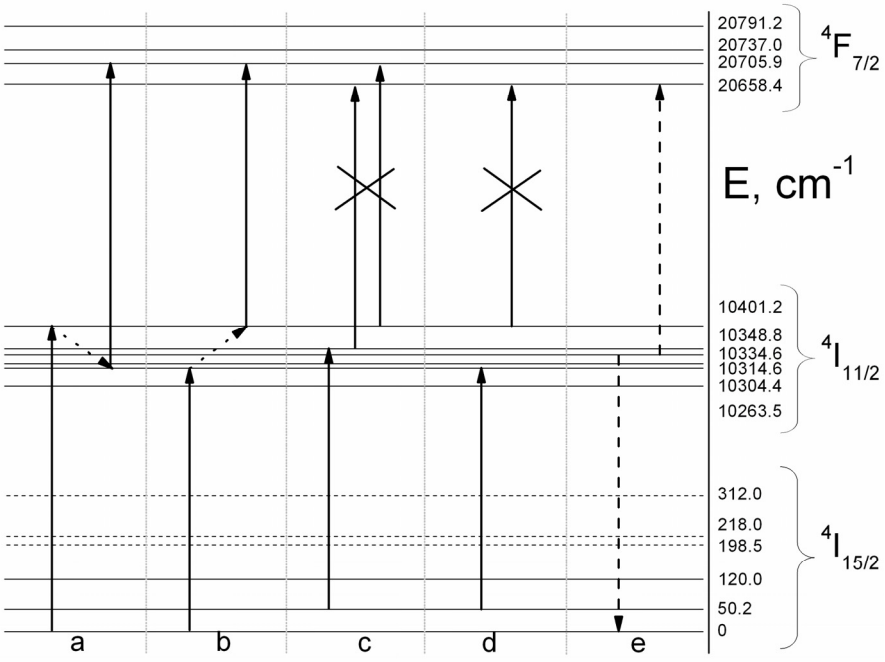

Fig. 5.28: Energy level scheme of Er^{3+} ion in LaF_3 [49] and possible mechanisms of the UC luminescence in the crystalline phase of the GC sample at 50 K.

Excitation at 10401.2 cm^{-1} (961.4 nm) (**Fig. 5.28a**) corresponds to the energy difference between the first Stark sublevel of the ground state ($^4I_{15/2}$) and the sixth Stark sublevel of the excited state ($^4I_{11/2}$) and is effectively absorbed in $LaF_3:Er^{3+}$ crystallites. The subsequent thermalization of the $^4I_{11/2}$ level, taking place in ps time scale, populates the second Stark sublevel of the $^4I_{11/2}$ (10304.4 cm^{-1}), from which the system can be excited with the same excitation energy of the laser to the second Stark sublevel of the $^4F_{7/2}$ (10304.4 + 10401.2 = 20705.6 cm^{-1}). The resulting energy is just by 0.3 cm^{-1} off-resonance from the actual Stark sublevel position of the $^4F_{7/2}$ and therefore is effectively absorbed. As the result the decay kinetics of the UC luminescence under excitation at 10401.2 cm^{-1} has ESA nature.

Similarly, when the system is excited at 10304.4 cm^{-1} (970.5 nm) (**Fig. 5.28b**), corresponding to the energy difference between the first Stark sublevel of the ground state and the second Stark sublevel of the $^4I_{11/2}$, the excitation radiation is absorbed. After the fast thermalization, the sixth Stark sublevel of the $^4I_{11/2}$ is populated, from which the system can be excited with the same excitation energy of the laser to the second Stark sublevel of the $^4F_{7/2}$ (10401.2 + 10304.4 = 20705.6 cm^{-1}), suggesting the ESA mechanism of the UC luminescence to be dominant.

It should be mentioned though that the decay kinetics of the "green" UC luminescence, exciting at 10401.2 cm^{-1} and 10304.4 cm^{-1} do not coincide with the decay kinetics of the "green" luminescence at direct excitation of the $^4F_{7/2}$ level (at 484.2 nm) or direct excitation of the emitting $^4S_{3/2}$ level (at 537.0 nm) **Fig. 5.27**). This is probably due to a slight involvement of the ET mechanism of the UC luminescence which will be discussed later.

Excitation at 10298.6 cm^{-1} (971.0 nm) (**Fig. 5.28c**) corresponds to the energy difference between the second Stark sublevel of the ground state ($^4I_{15/2}$) and the fifth Stark sublevel of the excited state ($^4I_{11/2}$) and is effectively absorbed in $LaF_3:Er^{3+}$ crystallites. It is obvious that any possible excitation with the same laser radiation from the $^4I_{11/2}$ to $^4F_{7/2}$ must start from either fifth or sixth Stark sublevel of the $^4I_{11/2}$. In the case of the fifth Stark sublevel the resulting energy would be 10348.8 + 10298.6 = 20647.4 cm^{-1} which is by -11.0 cm^{-1} off-resonance from the required energy to reach the first Stark sublevel of the $^4F_{7/2}$ (20658.4 cm^{-1}).

Similar calculations yield -6.1 cm^{-1} for the case of the sixth Stark sublevel of the $^4I_{11/2}$ and the second Stark sublevel of the $^4F_{7/2}$.

The excitation at 10251.0 cm^{-1} (975.5 nm) (**Fig. 5.28d**) corresponds to the energy difference between the second Stark sublevel of the ground state ($^4I_{15/2}$) and the second Stark sublevel of the excited state ($^4I_{11/2}$) and despite slight off-resonance (-3.2 cm^{-1}) is effectively absorbed by the system, showing a peak in the excitation spectrum of the GC (**Fig. 5.24**). Further efficient excitation from the $^4I_{11/2}$ to the $^4F_{7/2}$ by the same laser radiation is possible only from the sixth Stark sublevel of the $^4I_{11/2}$: 10401.2 + 10251.0 = 20652.2 cm^{-1} which is by -6.2 cm^{-1} off-resonance from the required energy to reach the first Stark sublevel of the $^4F_{7/2}$ (20658.4 cm^{-1}). For the both excitation energies, shown in **Fig. 5.28c** and **Fig. 5.28d** (10298 cm^{-1} and 10251 cm^{-1}), the UC luminescence decay kinetics have explicit rise part of the intensity (**Fig. 5.27**), indicating the dominance of the ET mechanism in the creation of the luminescence. Since one of the preconditions of the ESA process to be dominant in a system is almost perfect conjunction of the photon energies required for the ground state absorption (GSA) and ESA, a certain off-resonance between the two absorption types can decrease the efficiency of the ESA mechanism of the UC. Indeed from the analysis of **Fig. 5.28** it can be seen that the off-resonance between the GSA and ESA higher than 6 cm^{-1} significantly decreases the probability of the ESA process in the crystalline phase of the GC at 50 K. On the other hand the measurements at RT indicated the dominance of the ESA mechanism of the UC luminescence (**Fig. 5.26**). The prevalence of the ESA mechanism at RT could be explained by considerably broader excitation bands of the UC luminescence measured at RT (**Fig. 5.24**). The broad excitation bands related to the electronic transitions between different Stark sublevels of the ground state ($^4I_{15/2}$) and the excited states ($^4I_{11/2}$, $^4F_{7/2}$) (**Fig. 5.24** and **Fig. 5.25**) allow for better overlap of the GSA and ESA thus greatly enhancing the efficiency of the ESA mechanism of the UC luminescence at RT.

One of the possible ET mechanisms in $LaF_3:Er^{3+}$ crystallites is shown in **Fig. 5.28e**. The downward arrow represents the energy released by one of Er^{3+} ions (sensitizer) and upward arrow stands for the energy absorbed by another Er^{3+} ion (activator). The energetic misfit between the two energies is 9.2 cm^{-1} but since the ET mechanism usually is a multiphonon-assisted process there is no requirement for the perfect coincidence between the two energies. From the ET mechanism shown in **Fig. 5.28e** it is clear that the population rate of the $^4S_{3/2}$ level is defined by the lifetime of the $^4I_{11/2}$ level. Since the lifetime of the $^4I_{11/2}$ level of Er^{3+} in fluorides usually is longer than that of $^4S_{3/2}$ [11, 70, 71], the decay kinetics of the UC luminescence produced by

ET mechanism should be longer. Indeed the decay kinetics related to ET mechanism have effective lifetime value 2.32 ms, while the ones related to the ESA mechanism – 1.52 ms.

In the case of the pure ESA mechanism, the decay kinetics of the UC luminescence should coincide with the decay kinetics obtained at direct excitation. However, one can notice slight deviation between the decay kinetics of the UC luminescence excited at 961.4 nm (τ_{UC} ~ 1.52 ms) and that obtained at direct excitation at 537.0 nm (τ_{direct} ~ 1.1 ms). Slightly longer decay kinetics obtained in the ESA process compared to the one at direct excitation is probably due to a minor involvement of the ET mechanism in the creation of the UC luminescence although the ESA mechanism still prevails.

5.2.3. Summary

1) Oxyfluoride silicate glass and transparent glass ceramics containing LaF_3 crystallites was synthesized.
2) During the synthesis the activator ions partially incorporate in the crystalline phase, and $LaF_3:Er^{3+}$ is formed.
3) The UC luminescence spectra, the excitation spectra and the decay kinetics of the "green" luminescence band of Er^{3+} were measured for the GC sample at 50 K and RT.
4) At RT the dominant mechanism of the UC luminescence in the GC sample is ESA, while at 50 K – the ET mechanism prevails.
5) The ESA mechanism of the UC luminescence is still active at 50 K for the excitation energies, at which the energetic off-resonance between the GSA and ESA is less than 6 cm^{-1}.

The results are published in A. Sarakovskis, J. Grube, G. Doke, M. Springis, *Excited state absorption and energy-transfer mechanisms of up-conversion luminescence in Er^{3+}-doped oxyfluoride glass ceramics at different temperatures*, Journal of Luminescence, **130**, 5 (2010), p. 805 - 811. {SCI, Impact factor 1.628}

5.3. Thesis

- Novel synthesis method of $NaLaF_4:Er^{3+}$ has been developed allowing to synthesize the material without using a hydrofluoric acid.
- Luminescence properties of $NaLaF_4:Er^{3+}$ depend on the synthesis conditions:
  - The increase of Er^{3+} concentration in $NaLaF_4:Er^{3+}$ causes the formation of $Na(LaEr)F_4$ complex compound responsible for the shortening of the lifetime of Er^{3+} luminescence.
  - The quenching of the up-conversion luminescence in $NaLaF_4:Er^{3+}$ depends on the annealing temperature: below $500^{O}C$ the up-conversion luminescence is quenched by OH^- related defects, but above $500^{O}C$ – the quenching is due to other oxygen related defects.
  - The post-treatment of $NaLaF_4:Er^{3+}$ in fluorine atmosphere at $500^{O}C$ reduces the content of oxygen impurities in the material and significantly diminishes the quenching effect of the up-conversion luminescence.

- The dominance of either excited-state-absorption or energy-transfer mechanisms of the up-conversion luminescence in oxyfluoride glass ceramics containing $LaF_3:Er^{3+}$ nanocrystals is temperature dependent.
- A criterion, which entails the dominance of energy-transfer over excited-state-absorption mechanism of the up-conversion luminescence in the crystalline phase of the glass ceramics at 50 K, is the energy mismatch of more than 6 cm^{-1} between ground-state-absorption and excited-state-absorption.

6. Outlook

In this work two prospective materials for the UC purposes, namely, $NaLaF_4:Er^{3+}$ and oxyfluoride glass ceramics containing $LaF_3:Er^{3+}$ were investigated.

It was concluded that the increase of Er^{3+} concentration in $NaLaF_4:Er^{3+}$ causes the formation of $Na(LaEr)F_4$ complex compound responsible for the shortening of the lifetime of Er^{3+} luminescence, while the quenching of the UC luminescence in $NaLaF_4:Er^{3+}$ synthesized at different temperatures is explained by Er^{3+}-oxygen related defects.

From the application point of view the existence of oxygen defects in fluorides is undesirable, because they act as "killers" of the UC luminescence due to their involvement in the enhanced non-radiative de-excitation of RE ions leading to the decrease of the UC efficiency. From scientific point of view the existence of such defects in $NaLaF_4:RE^{3+}$ raises a series of challenging questions to be answered: what is the structure of these defects? What is the mechanism of their formation? What is the mechanism of the energy transfer from RE^{3+} to the oxygen defect? Once these questions are answered, possible applications like, for example, fluorine sensors may follow.

Another material investigated in this work is the transparent oxyfluoride silicate glass ceramics containing $LaF_3:Er^{3+}$. It was synthesized by thermal treatment of the precursor glass and up-conversion properties of the material were studied at room temperature and 50 K. It was shown that the dominance of either ESA or ET mechanisms of the UC luminescence in oxyfluoride glass ceramics containing $LaF_3:Er^{3+}$ nanocrystals is temperature dependent. A dominance criterion of either of the two mechanisms of the UC luminescence in the crystalline phase of the glass ceramics was provided, however, some general unanswered questions related to the glass ceramics still remain.

Although the glass ceramics provides an interesting model, where two different RE doped phases (glass and crystalline) coexist, the studies of the UC luminescence in such systems reported in the literature are strictly targeted on either of the two phases: the glass or the crystallites. But is there any energy transfer between the two phases and if it can be observed, what are the mechanisms of such energy transfer?

On the other hand, it was shown that the efficiency of the UC luminescence in oxyfluoride glass ceramics is defined by the efficiency of the UC process in the fluoride component of the ceramics. At the present, the most efficient fluoride host for the UC purposes is considered to be $NaYF_4$ mainly due to its low phonon energy. Soon after the excellent UC properties of crystalline RE^{3+} doped $NaYF_4$ were reported a number of works, in which oxyfluoride glass ceramics with $NaYF_4$ nanocrystallites, have appeared.

In the present work the Raman spectrum measured for $NaLaF_4$ showed that the phonon energy of the latter is lower than that reported for $NaYF_4$, raising another challenging task – to obtain oxyfluoride glass ceramics with $NaLaF_4$:RE^{3+} nanocrystals.

The raised questions are the subject of further investigations that will be continued after the defending of the present thesis.

References

[1] F. Auzel, *Compteur quantique par transfert d'énergie entre deux ions de terres rares*, Comptes Rendus l'Académie Des Sci. (Paris) **262**, 1016 (1966).

[2] Y. Wang, J. Ohwaki, *High efficiency infrared to visible upconversion of Er^{3+} in $BaCl_2$*, Journal of Applied Physics **74**, 2 (1993), p. 1272 – 1278.

[3] J. M. Breteau, J. L. Ayral, F. Micheron, F. Auzel, *Medical x-ray imaging in infrared to visible upconverting materials*, Journal of Applied Physics **67**, 2 (1990), p. 1102 – 110.

[4] E. Downing, L. Hesselink, J. Ralston, R. Macfarlane, *A Three-Color, Solid-State, Three-Dimensional Display*, Science **273**, 5279 (1996), p. 1185 – 1189.

[5] J. E. C. Silva, G. F. de Sa, P. A. Santa-Cruz, *White light simulation by up-conversion in fluoride glass host*, Journal of Alloys and Compounds **344**, 1–2, (2002), p. 260 – 263.

[6] C. Li, B. Dong, S. Li, C. Song, *Er^{3+}–Yb^{3+} co-doped silicate glass for optical temperature sensor*, Chemical Physics Letters **443**, 426 (2007), p. 426 – 429.

[7] L. F. Johnson, H. J. Guggenheim, *Infrared-Pumped Visible Laser*, Applied Physics Letters **19**, 2, (1971**)**, p. 44 – 47.

[8] H. J. M. A. A. Zijlmans, J. Bonnet, J. Burton, K. Kardos, T. Vail, R. S. S. Niedbala, H.J. Tanke, *Detection of Cell and Tissue Surface Antigens Using Up-Converting Phosphors: A New Reporter Technology*, Analytical Biochemistry **267**, 1 (1999) p. 30 – 36.

[9] B.N. Samson, P.A. Tick, N.F. Borrelli, *Efficient neodymium-doped glass-ceramic fiber laser and amplifier*, Optics Letters **26**, 3 (2001), p. 145 – 147.

[10] A. Shalav, B.S. Richards, M.A. Green, *Luminescent layers for enhanced silicon solar cell performance: Up-conversion*, Solar Energy Materials and Solar Cells **91**, 9 (2007), p. 829 – 842.

[11] J.F. Suyver, J. Grimm, M.K. van Veen, D. Biner, K.W. Krämer, H.U. Güdel, *Upconversion spectroscopy and properties of $NaYF_4$ doped with Er^{3+}, Tm^{3+} and/or Yb^{3+}*, Journal of Luminescence **117**, 1 (2006), p. 1 – 12.

[12] M. Dejneka, *Transparent oxyfluoride glass ceramics*, MRS Bulletin 23, 11 (1998), p. 56 – 62.

[13] Jisen Zhang, W. Qin, D. Zhaoa, Degejihu, J. Zhang, Y. Wang, C. Cao, *Spectral variations and energy transfer processes on both Er^{3+} ion concentration and excitation densities in Yb^{3+}–Er^{3+} codoped LaF_3 materials*, Journal of Luminescence **122-123** (2007), p. 506 – 508.

[14] Rayko Simura, A. Jouini, K. Kamada, A. Yoshikawa, K. Aoki, Y. Guyot, G. Boulon, T. Fukuda, *Growth and characterization of Pr^{3+}-doped $Gd_{1-x}Yb_xF_3$ fluoride single crystal for visible up-conversion luminescence applications*, Journal of Crystal Growth **291**, 1 (2006), p. 309 – 313.

[15] C. Cao, W. Qin, J. Zhang, Y. Wang, P. Zhu, G. Wang, G. Wei, L. Wang, L. Jin, *Enhanced ultraviolet up-conversion emissions of Tm^{3+}/Yb^{3+} codoped YF_3 nanocrystals*, Journal of Fluorine Chemistry 129, 3 (2008), p. 204 – 209.

[16] M. Bouffard, J. P. Jouart, M.-F. Joubert, *Red-to-blue up-conversion spectroscopy of Tm^{3+} in SrF_2, CaF_2, BaF_2 and CdF_2*, Optical Materials **14**, 1 (2000), p. 73 – 79.

[17] C. Cao, W. Qin, J. Zhang, Y. Wang, G. Wang, G. Wei, P. Zhu, L. Wang, L. Jin, *Up-conversion white light of $Tm^{3+}/Er^{3+}/Yb^{3+}$ tri-doped CaF_2 phosphors*, Optics Communications **281**, 6 (2008), p. 1716 – 1719.

[18] X.P. Chen, Q.Y. Zhang, C.H. Yang, D.D. Chen, C. Zhao, *Comparative investigation on structure and luminescence properties of fluoride phosphors codoped with Er^{3+}/Yb^{3+}*, Spectrochimica Acta Part A: Molecular and Biomolecular Spectroscopy **74**, 2 (2009), p. 441 – 445.

[19] S. A. Pollack, D. B. Chang, *Ion-pair upconversion pumped laser emission in Er^{3+} ions in YAG, YLF, SrF_2, and CaF_2 crystals*, Journal of Applied Physics **64**, 6 (1988), p. 2885 – 2893.

[20] J. Zhang, Z. Duan, D. He, S. Dai, L. Zhang, L. Hu, *Intense blue up-conversion luminescence in Tm^{3+}/Yb^{3+} codoped oxyfluoride glass–ceramics containing β-PbF_2 nanocrystals*, Spectrochimica Acta Part A: Molecular and Biomolecular Spectroscopy **62**, 4-5 (2005), p. 831 – 834.

[21] J.F. Suyver, A. Aebischer, D. Biner, P. Gerner, J. Grimm, S. Heer, K.W. Krämer, C. Reinhard, H.U. Güdel, *Novel materials doped with trivalent lanthanides and transition metal ions showing near-infrared to visible photon upconversion*, Optical Materials **27**, 6 (2005), p. 1111 – 1130.

[22] K.W. Kramer, D. Biner, G. Frei, H. U. Gudel, M. P. Hehlen, S. R. Luthi, *Hexagonal Sodium Yttrium Fluoride Based Green and Blue Emitting Upconversion Phosphors*, Chemistry of Materials **16**, 7 (2004), p. 1244 – 1251.

[23] J. Shan, Y. Ju, *Controlled synthesis of lanthanide-doped $NaYF_4$ upconversion nanocrystals via ligand induced crystal phase transition and silica coating*, Applied Physics Letters **91**, 12 (2007), p. 123103 – 123105.

[24] G. Wang, W. Qin, L. Wang, G. Wei, P. Zhu, R. Kim, *Intense ultraviolet upconversion luminescence from hexagonal $NaYF_4:Yb^{3+}/Tm^{3+}$ microcrystals*, Optics Express **16**, 16 (2008), p. 11907 – 11914.

[25] S. Heer, K, Kompe, H. U. Gudel, M. Haase, *Highly efficient multicolour upconversion emission in transparent colloids of lanthanide doped $NaYF_4$ nanocrystals*, Advanced Materials **16**, 23-24 (2004), p. 2102 – 2105.

[26] T. Kano, H. Yamamato, Y. Otomo, *$NaLnF_4:Yb^{3+}$, Er^{3+} (Ln:Y, Gd, La): efficient green-emitting infrared-excited phosphors*, Journal of Electrochemical Society: Solid State Science and Technology **119**, 11 (1972), p. 1561 – 1564.

[27] Z. Wang, F. Tao, L. Yao, W. Cai, X. Li, *Selected synthesis of cubic and hexagonal $NaYF_4$ crystals via a complex-assisted hydrothermal route*, Journal of Crystal Growth **290**, 1 (2006), p. 296 – 300.

[28] N. Martin, P. Boutinaud, M. Malinowski, R. Mahiou, J. C. Cousseins, *Optical spectra and analysis of Pr^{3+} in β-$NaYF_4$*, Journal of Alloys and Compounds **275-277** (1998), p. 304 – 306.

[29] A. Grzechnik, P. Bouvier, M. Mezouar, M. D. Mathews, A. K. Tyagi, J. Kohler, Hexagonal $Na_{1.5}Y_{1.5}F_6$ at High Pressures, Journal of Solid State Chemistry 165 (2002), p. 159 – 164.

[30] M. M. Lage, F. M. Matinaga, J.-Y. Gesland, R. L. Moreira, *Optical phonon modes and crystal structure of $NaLaF_4$ single crystals*, Journal of applied Physics 99 (2006), p. 053510 – 053517.

[31] G. S. Yi, G. M. Chow, *Synthesis of hexagonal-phase $NaYF_4$:Yb,Er and $NaYF_4$:Yb,Tm nanocrystals with efficient up-conversion fluorescence*, Advanced Functional Materials **16** (2006), p. 2324 – 2329.

[32] S.F. León-Luis, J. Abreu-Afonso, J. Pena-Martinez, J. Mendez-Ramos, A.C. Yanes, J. del-Castillo, V.D. Rodriguez, *Up-conversion and colour tuneability*

in Yb^{3+}–Er^{3+}–Tm^{3+} co-doped transparent nano-glass-ceramics, Journal of Alloys and Compounds **479**, 1-2 (2009), p. 557 – 560.

[33] F. C. Guinhos, P. C. Nobrega, P. A. Santa-Cruz, *Compositional dependence of up-conversion process in Tm^{3+}–Yb^{3+} codoped oxyfluoride glasses and glass-ceramics*, Journal of Alloys and Compounds **323-324** (2001), p. 358 – 361.

[34] J. Mendez-Ramos, V.K. Tikhomirov, b, V.D. Rodriguez, D. Furniss, *Infrared tuneable up-conversion phosphor based on Er^{3+}-doped nano-glass–ceramics*, Journal of Alloys and Compounds **440**, 1-2 (2007), p. 328 – 332.

[35] D. Chen, Y. Wang, E. Ma, Y. Yu, F. Liu, *Partition, luminescence and energy transfer of Er^{3+}/Yb^{3+} ions in oxyfluoride glass ceramic containing CaF_2 nano-crystals*, Optical Materials **27**, 12 (2007), p. 1693 – 1699.

[36] D. Chen, Y. Wang, Y. Yu, E. Ma, F. Bao, Z. Hu, Y. Cheng, *Influences of Er^{3+} content on structure and upconversion emission of oxyfluoride glass ceramics containing CaF_2 nanocrystals*, Materials Chemistry and Physics **95** (2006), p. 264–269.

[37] Y. Kishi, S. Tanabe, *Infrared-to-visible upconversion of rare-earth doped glass ceramics containing CaF_2 crystals*, Journal of Alloys and Compounds **408-412** (2006), p. 842 – 844.

[38] Z. Hu, Y. Wang, E. Ma, D. Chen, F. Bao, *Microstructures and upconversion luminescence of Er^{3+} doped and Er^{3+}/Yb^{3+} co-doped oxyfluoride glass ceramics*, Materials Chemistry and Physics **101** (2007), p. 234 – 237.

[39] X. Qiao, X. Fan, M. Wang, X. Zhang, *Spectroscopic properties of Er^{3+}–Yb^{3+} co-doped glass ceramics containing BaF_2 nanocrystals*, Journal of Non-Crystalline Solids **354** (2008), p. 3273 – 3277.

[40] D. Chen, Y. Wang, Y. Yu, E. Ma, L. Zhou, Microstructure and luminescence of transparent glass ceramic containing Er^{3+}:BaF_2 nano-crystals, Journal of Solid State Chemistry **179** (2006), p. 532 – 537.

[41] Y. Yu, D. Chen, Y. Wang, F. Liu, E. Ma, *A new transparent oxyfluoride glass ceramic with improved luminescence*, Journal of Non-Crystalline Solids **353** (2007), p. 405 – 409.

[42] Y. Wang, J. Ohwaki, *New transparent vitroceramics codoped with Er^{3+} and Yb^{3+} for efficient frequency upconversion*, Applied Physics Letters **63**, 24 (1993), p. 3268 – 3270.

[43] E. Ma, Z. Hu, Y. Wang, F. Bao, *Influence of structural evolution on fluorescence properties of transparent glass ceramics containing LaF_3 nanocrystals*, Journal of Luminescence **118** (2006), p. 131 – 138.

[44] Z. Hu, E. Ma, Y. Wang, D. Chen, *Fluorescence property investigations on Er^{3+}-doped oxyfluoride glass ceramics containing LaF_3 nanocrystals*, Materials Chemistry and Physics **100** (2006), p. 308 – 312.

[45] Z. Hu, Y. Wang, F. Bao, W. Luo, *Crystallization behavior and microstructure investigations on LaF_3 containing oxyfluoride glass ceramics*, Journal of Non-Crystalline Solids **351** (2005), p. 722 – 728.

[46] M. H. V. Werts, *Making sense of lanthanide luminescence*, Science Progress 88, 2 (2005), p. 101-131.

[47] T. Kano, *Principal phosphor materials and their optical properties*, Phosphor Handbook, 2nd edition, edited by W. M. Yen, S. Shionoya, H. Yamamoto, Boca Raton, FL: CRC Press, Taylor & Francis Group, 2007

[48] M. H. V. Werts, R. T. F. Jukes, J. W. Verhoeven, *The emission spectrum and the radiative lifetime of Eu^{3+} in luminescent lanthanide complexes*, Physical Chemistry Chemical Physics 4 (2002), p. 1542 – 1548.

[49] W. F. Krupke, and J. B. Gruber, *Absorption and fluorescence spectra of Er^{3+} ($4f^{11}$) in LaF_3*, Journal of Chemical Physics **39**, 4 (1963), p. 1024 – 1030.

[50] Mrinmay Pal, M.C. Paul, A. Dhar, A. Pal, R. Sen, K. Dasgupta, S.K. Bhadra, *Investigation of the optical gain and noise figure for multi-channel amplification in EDFA under optimized pump condition*, Optics Communications **273**, 2 (2007), p. 407 – 412.

[51] F. Auzel, *Upconversion and Anti-Stokes Processes with f and d Ions in Solids*, Chemical Review **104**, 1 (2004), p. 139 – 173.

[52] J. F. Suyver, *Upconversion Phosphors*, Luminescence from theory to applications, edited by Cees Ronda, Weinheim: WILEY-VCH Verlag GmbH & Co. KGaA, 2008.

[53] M. Pollnau, D. R. Gamelin, S. R. Luthi, H. U. Gudel, *Power dependence of upconversion luminescence in lanthanide and transition-metal-ion systems*, Physical Review B 61, 5 (2000), p. 3337 – 3346.

[54] S. Tanabe, H. Hayashi, T. Hanada, N. Onodera, *Fluorescence properties of Er^{3+} ions in glass ceramics containing LaF_3 nanocrystals*, Optical Materials **19**, 3 (2002), p. 343 – 349.

[55] F. Abdoun, M. Gaune-Escard, G. Hatem, Calorimetric and thermal analysis investigations of the MF-LaF_3 Mixtures (M = Alkali Metal), Journal of Phase Equilibria 18, 1 (1997), p. 6 – 20.

[56] R.E. Thoma, H. Insley, and G.M. Hebert, The sodium fluoride-lanthanide trifluoride systems, Inorganic Chemistry **5**, 7 (1966), p. 1222 – 1229.

[57] P. Fedorov, I. I. Buchinskaya, O. S. Bondareva, A. A. Bystrova, L. L. Vistin, D. A. Ershov, S. P. Ivanov, V. A. Stasyuk, and B. P. Sobolev, *Phase Diagrams of the NaF-RF_3 (R = La, Ce, Pr, Nd, Sm) Systems*, Russian Journal of Inorganic Chemistry **45**, 6 (2000), p. 949 – 953.

[58] A. H. Krumpel, E. van der Kolk, D. Zeelenberg, A. J. J. Bos, K. W. Krämer, P. Dorenbos, *Lanthanide 4f-level location in lanthanide doped and cerium-lanthanide codoped $NaLaF_4$ by photo- and thermoluminescence*, Journal of Applied Physics 104 (2008), p. 073505 – 073515.

[59] J. H. Burns, Crystal structure of hexagonal sodium neodymium fluoride and related compounds, Inorganic Chemistry 4, 6 (1965), p. 881 – 886.

[60] F. Liu, Y. Wang, D. Chen, Y. Yu, E. Ma, L. Zhou, P. Huang, *Upconversion emission of a novel glass ceramic containing Er^{3+}: $BaYF_5$ nano-crystals*, Materials Letters **61**, 28 (2007), p. 5022 – 5025.

[61] F. Liua, E. Ma, D. Chen, Y. Wang, Y. Yua, P. Huang, *Infrared luminescence of transparent glass ceramic containing Er^{3+}:$NaYF_4$ nanocrystals*, Journal of Alloys and Compounds 467, 1-2 (2009), p. 317 – 321.

[62] T. Hatakeyama, F. X. Quinn, *Thermogravimetry*, Thermal analysis Fundamentals and applications to polymer science, 2nd edition, Chichester: John Wiley and Sons, 1999.

[63] http://www.ssi.shimadzu.com/products/literature/Thermal/Thermal60_Series.pdf.

[64] P. Scherrer, *Bestimmung der Grosse und der inneren Struktur von Kolloidteilchen mittels Röntgenstrahlen*, Nachrichten von der Gesellschaft der Wissenschaften **2** (1918), p. 98–100.

[65] R.D. Shannon, *Revised effective ionic radii and systematic studies of interatomic distances in halides and chalcogenides*, Acta Crystallographica A **32**, 5 (1976), p. 751 – 767.

[66] A. Mech, M. Karbowiak, L. Kepinski, A. Bednarkiewicz, W. Strek, *Structural and luminescent properties of nano-sized NaGdF4:Eu^{3+} synthesised by wet-chemistry route*, Journal of Alloys and Compounds **380** (2004), p. 315 – 320.

[67] T. J. Bastow, S. N. Stuart, W. G. McDugle, R.S. Eachus, J. M. Spaeth, *Oxygen impurities in x-ray storage phosphors BaFBr and BaFCl investigated by ^{17}O NMR*, Journal of Physics: Condensed Matter **6** (1994), p. 8633 – 8644.

[68] M. Karbowiak, A. Mech, L. Kepinski, W. Mielcarek, S. Hubert, *Effect of crystallite size on structural and luminescent properties of nanostructured Eu^{3+}:$KGdF_4$ synthesised by co-precipitation method*, Journal of Alloys and Compounds **400** (2005), p. 67 – 75.

[69] A. Bednarkiewicz, A. Mech, M. Karbowiak, W. Strek, *Spectral properties of Eu^{3+} doped $NaGdF_4$ nanocrystals*, Journal of Luminescence **114** (2005), p. 247 – 254.

[70] M. J. Weber, *Selective excitation and decay of Er^{3+} fluorescence in LaF_3*, Physical Review **156**, 2 (1967), p. 231 – 241.

[71] C. Sassoye, G. Patriarche, M. Mortier, *High yield syntheses of reactive fluoride* $K_{1-x}(Y,Ln)_xF_{1+2x}$ *nanoparticles*, Optical Materials **31**, 8 (2009), p. 1177 – 1183.

7. List of publications

1. A. Sarakovskis, L. Dimitrocenko, A. Misnevs, U. Rogulis, M. Springis, *Up-conversion process in erbium doped lithium fluoride bulk crystal, lithium borate glass and glass ceramics*, Journal of Physics: Conference Series **93** (2007) p. 012041 – 012047.

2. J. Grube, A. Sarakovskis, L. Dimitrocenko, M. Springis, Temperature Effects in *Up-Conversion Processes of Erbium - Ytterbium Doped Oxyfluoride Silicate Glass*, Latvian Journal of Physics and Technical Sciences 45, 6 (2008), p. 47 – 54.

3. A. Sarakovskis, J. Grube, G. Doke, M. Springis, *Excited state absorption and energy-transfer mechanisms of up-conversion luminescence in Er^{3+}-doped oxyfluoride glass ceramics at different temperatures*, Journal of Luminescence, **130**, 5 (2010), p. 805 - 811. ***{SCI}***

4. A. Sarakovskis, J. Grube, A. Mishnev, M. Springis, *Up-conversion processes in $NaLaF_4:Er^{3+}$*, Optical Materials **31**, 10 (2009), p. 1517 – 1524. ***{SCI}***

5. A. Sarakovskis, J. Grube, G. Doke, and M. Springis, *Selective excitation of up-conversion luminescence by Yb^{3+}-Er^{3+} energy transfer in glass and crystalline phase of oxyfluoride glass ceramics*, Optical Materials, submitted to journal. ***{SCI}***

8. List of conference abstracts

1. A. Sarakovskis, L. Dimitrocenko, A. Petruhins, J. Grube, I. Tale, U. Rogulis, M. Springis, *Up-conversion luminescence of Er^{3+} in LiF crystals*, 23rd Scientific Conference in Institute of Solid State Physics, Riga, Latvia, February 13 – 15, 2007.

2. Sarakovskis, L. Dimitrocenko, A. Misnevs, U. Rogulis, M. Springis, *Up-conversion process in erbium doped lithium fluoride bulk crystal, lithium borate oxyfluoride glass and glass ceramics*, International Baltic Sea Region conference Functional Materials and Nanotechnologies, Riga, Latvia, April 2 – 4, 2007.

3. A. Sarakovskis, L. Dimitrocenko, A. Petruhins, J. Grube, A. Misnevs, U. Rogulis, M. Springis, *Multiphoton processes in rare-earth doped oxyfluoride glasses*, Developments in Optics and Communications, Riga, Latvia, April 27 – 29, 2007.

4. A. Sarakovskis, L. Dimitrocenko, J. Grube, M. Springis, *Spectral and time-resolved studies of up-conversion luminescence in glass ceramics containing $NaYF_4$:Er nanocrystals*, 24th Scientific Conference in Institute of Solid State Physics, Riga, Latvia, February 20 – 22, 2008.

5. Anatolijs Sarakovskis, Jurgis Grube, Lauris Dimitrocenko, Maris Springis, *Time-resolved spectroscopy of up-conversion processes in Er doped $NaYF_4$ silicate glass ceramics*, International Baltic Sea Region conference Functional Materials and Nanotechnologies, Riga, Latvia, April 1 – 4, 2008.

6. A. Sarakovskis, J. Grube, L. Dimitrocenko, S. Fomins, M. Springis, *Up-conversion luminescence studies on Er^{3+}, Yb^{3+} and Tm^{3+} doped oxyfluoride glass and glass ceramics*, The 6th International Conference on Advanced Optical Materials and Devices, Riga, Latvia, August 24 – 27, 2008.

7. A.Sarakovskis, J.Grube, A.Misnovs, G.Doke, M.Springis, *Energy transfer in Er^{3+} and Yb^{3+} doped silicate glass and glass ceramics*, 25th Scientific Conference in Institute of Solid State Physics, Riga, Latvia, February 11 – 13, 2009.

8. A. Sarakovskis, J. Grube, M. Springis, *Synthesis and up-conversion luminescence properties of $NaLaF_4:Er^{3+}$*, International conference Functional Materials and Nanotechnologies, Riga, Latvia, March 31 – April 4, 2009.

9. A. Sarakovskis, J. Grube, G. Doke, M. Springis, *Synthesis and up-conversion luminescence properties of $NaLaF_4:Er^{3+}$*, Developments in Optics and Communications, Riga, Latvia, April 24 - 26, 2009.

9. Acknowledgements

Author acknowledges EU European Social Fund, Latvian National Research program in Materials Science and Structural Funds for financial support.

Special thanks to my scientific supervisors **Maris Springis** for his patience, continuous support, encouragement and friendship during all my years of studies and research and **Ivars Tale** for the freedom to follow my own ideas, critical comments and valuable discussions.

Thanks to my closest colleagues and friends at the Institute of Solid State Physics: Jurgis Grube, Guna Doke, Krisjanis Smits, Jelena Butikova, Uldis Rogulis, Aris Veispals, Lauris Dimitrocenko for the great times spent at the ISSP and not only. Special thanks to Liga Grinberga for her care and support.